Eidgenössische Technische Hochschule Zürich
Swiss Federal Institute of Technology Zurich

Master Thesis

Correlation Function Measurements of a Microwave Frequency Single Photon Source

Autor:	Deniz Bozyigit
Student number:	04-923-579
Master program:	Electrical Engineering and Information Technology
Supervisor:	Prof. Dr. Andreas Wallraff, Laboratory of Solid State Physics, ETH Zürich
Professor D-ITET:	Prof. Dr. Helmut Bölcskei Communication Technology Laboratory

Zurich, 12. April 2010

Abstract

The *circuit quantum electrodynamics* (QED) setup [1] was shown [2] to be an excellent system for cavity quantum electrodynamics experiments in which the coherent interaction between an atom and the light field in an optical cavity is investigated. This thesis summarizes our efforts to adapt the *measurement of electric field correlations* to the circuit QED setup.

Correlation measurements are one of the most established methods in quantum optics to investigate light and its interaction with other systems. While very well understood theoretically and experimentally in the context of optics, the application in the microwave domain is less investigated and the subject of ongoing research [3, 4, 5]. This is mainly a result of the fundamentally different available detectors which are photon counters in the optical and linear amplifiers in the microwave regime.

We discuss and present a system which allows to perform first and second-order correlation measurements of microwave radiation. To demonstrate the working of this system we implement a source emitting a family of microwave *single photon states* similar as in Refs. [6, 7, 8]. We characterize the non-classical microwave radiation successfully by measuring different properties, such as the field quadratures, the photon number and the time-resolved first- and second-order correlation functions.

In particular, we observe antibunching of the microwave photons in the second-order correlation function which is an unambiguous sign for the quantum mechanical nature of our single photon source. To our knowledge, this is the first documented observation of antibunching of microwave photons.

Contents

1. Introduction

With the advent of quantum mechanics about 100 years ago our physical understanding of the world changed dramatically. The basic idea that energy in physical systems is quantized [9, 10] resolved some of the most important inconsistencies in classical physics and evolved to the most successful physical theory of today - quantum mechanics in its canonical formulation. A huge variety of microscopic and macroscopic observations are explained on the basis of quantum mechanical considerations with no accepted contradictions to theory until now.

For the first time energy quantization was observed in the photoelectric effect a result of the interaction of light and matter. Today, the field of research in which the light-matter interaction is studied is known as *quantum optics* (QO) and is one of the most advanced fields in quantum sciences. There are excellent theoretical and experimental tools available which are very well understood and allow for the most detailed investigations [11]. Using these tools important results were achieved which helped to develop a better understanding of quantum mechanics in general.

As another topic in quantum science the *processing of information in quantum systems* recently became of interest. The main motivation behind this idea was given by Feynman in 1982: Realizing that a large quantum system can only be simulated using exponential amounts of resources, he concluded [12] that quantum systems must have vast inherent information processing capacities. This was confirmed by Shor in 1995 by his quantum algorithm [13] to factorize large numbers, which is an intractable problem on classical computers. Ever since there is an ongoing effort to implement the basic building blocks of a quantum system being able to perform this kind of algorithms - a *quantum computer*.

Since QO systems are experimentally and theoretically well understood many attempts to realize a quantum computer are fully or partly based on QO methods. Besides systems like ion traps and linear optics, one of the most promising candidates is the *circuit quantum electrodynamics* (circuit QED) setup, which is subject of investigation in our laboratory. In circuit QED superconducting circuit elements are used to build microwave resonators and non-linear quantum systems, which behave similar to atoms. It was shown that this is equivalent to the cavity QED system [1] from QO where atoms inside an optical cavity are used to study light-matter interaction. This equivalence is surprising since the physical realization differs completely from optical systems, including the experimental setup which consists of cryostats, microwave gear and superconducting circuits rather than lasers, optics and atoms in free space.

Indeed the circuit QED system was able to demonstrate significant advantages over the common implementations of cavity QED systems. In particular the very strong coupling [2] between atom and light which can be achieved in these systems together with reasonable coherence times [14] and excellent control [7] of the system allowed to observe many important effects known from QO. The same virtues and the possibility to use fabrication methods from microelectronics to engineer and scale up these systems qualifies it as an excellent candidate for the implementation of a quantum computer. This was demonstrated recently by first implementations of simple quantum algorithms [15] in a circuit QED system.

In this work we focused on the circuit QED system as a testbed for QO experiments instead of its potential use for a quantum computer. This is interesting because the physical properties can be engineered and one can enter parameter regimes which are not experimentally accessible in other systems.

To investigate light fields and the interaction with matter one of most established tools are measurements of the correlation functions of the electric field. In the measurement of correlation functions one observes the ability of light to interfere with itself. This ability to interfere is quantified in its degree of *temporal coherence* and is one of the key properties of light. Beyond the characterization of light itself, its coherence properties can be used to study the light emitting system. In many cases the temporal coherence properties are a finger print of the internal dynamics of the emitter and reveal many details about the internal physical processes.

While most of the physics in a circuit QED system is comparable to traditional QO systems [1] they differ significantly in the detection methods. In experiments at optical frequencies the best available detectors are *photon counters* and intensity detectors. Combined with beam splitters they can be used to measure a variety of properties of light, such as the intensity, the field-amplitude and different correlation functions of these quantities. In the microwave regime of circuit QED however most experiments rely on a *homodyne detection* scheme using microwave equipment such as linear amplifiers, mixers and oscilloscopes. In particular no efficient microwave photon counters are available today which would allow to use the same detection methods as in the optical domain.

Although the conventional measurement methods for correlation functions relied heavily on the use of photon detectors it was shown recently [16] that they are also accessible in homodyne detection schemes. In this thesis we work on the question how the such detection methods can be adapted to the circuit QED system, without relying on photon counters but rather on the existing homodyne detection method. In particular we focus on the measurement of the first- and second-correlation functions of the electric field of a single photon source.

2. Review Quantum Electrodynamics

In this chapter we will review the cavity quantum electrodynamics (cavity QED) setup and discuss how this type of system can be implemented equivalently using superconducting microwave electronics known as circuit QED.

2.1. Cavity QED

The cavity QED setup consists of an optical cavity containing an atom and is frequently used in quantum optics to investigate the interaction between light and matter. The cavity is made by two highly reflective mirrors defining a quantized mode of the electric field. Due to the high reflectivity of the mirrors, photons stay inside the cavity for a long time and can interact with the atom several times. After a time $1/\kappa$ characterized by the *cavity decay rate* κ the photons leave the cavity through the mirrors and can be detected on either end of the cavity. The relevant characteristics of the cavity are given by its resonance frequency $\omega_\mathrm{r}/2\pi$ and its decay rate κ or equivalently its *quality factor* $Q = \omega_\mathrm{r}/\kappa$.

The atom inside the cavity interacts with the electromagnetic field of the cavity mode via dipole interaction, which couples its electronic excitations to the cavity field. Although an atom generally has arbitrarily many electronic levels, it is valid in many cases to describe the atom as an effective two level system only considering a ground state $|g\rangle$ and one excited state $|e\rangle$ with an energy difference of $\hbar\omega_\mathrm{a}$. This approximation is good as long as the atom has an *anharmonic* energy spectrum, i.e. the higher-level transitions have frequencies different from the first.

In the case where the cavity and atom are in resonance, they can efficiently exchange energy quanta which happens at a rate g called the *coupling constant*. Normally the atom is coupled by similar mechanisms to other uncontrolled degrees of freedom which results in an energy loss at rate γ.

The Hamiltonian which describes this type of system is known as the *Jaynes-Cummings* Hamiltonian and is given by

$$H_\mathrm{JC} = \hbar\omega_\mathrm{r}(a^\dagger a + \frac{1}{2}) + \frac{\hbar\omega_\mathrm{a}}{2}\sigma_\mathrm{z} + \hbar g(a^\dagger\sigma^- + \sigma^+ a). \tag{2.1}$$

In the first term we have introduced the annihilation (creation) operator a ($a^\dagger$) of the cavity mode to describe the energy in the electric field. The second term represents the energy stored in the atom where the Pauli z-operator is $\sigma_\mathrm{z} = |g\rangle\langle g| - |e\rangle\langle e|$. The atom-cavity interaction

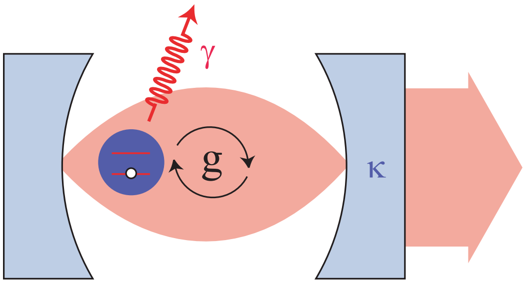

Figure 2.1.: Schematic of the cavity QED setup. Two mirrors define a quantized electric field mode. An atom positioned inside the cavity interacts with the electric field via a dipole interaction and can decay into other modes than the cavity mode indicated by the spontaneous decay rate γ.

is introduced by the third term where $\sigma^- = |g\rangle\langle e|$ and $\sigma^+ = |e\rangle\langle g|$ are the lowering and raising operators of the atomic transition. The rate of the interaction is given by the coupling constant g.

The behavior of this system gets particularly interesting when the interaction between the atom and the light field is strong such that g is larger than κ and γ, known as the *strong coupling* regime. In this regime the dynamics described by the Jaynes-Cummings Hamiltonian depend strongly on the detuning $\Delta = \omega_\mathrm{r} - \omega_\mathrm{a}$ between the atom and the cavity. To understand the behavior of the system it is instructive to discuss the two limits of small and large detuning.

Dispersive limit

When the detuning is large so that $|\Delta| \gg g$, no direct energy exchange between the electric field and the atom takes place but only a dispersive interaction remains. Since the value of g/Δ is small the Jaynes-Cummings Hamiltonian Eq. (2.1) can be simplified using a second order time dependent perturbation theory [17] by expansion in powers of g/Δ, leading to

$$H_\mathrm{disp} = \hbar \left(\omega_\mathrm{r} + \frac{g^2}{\Delta} \sigma_\mathrm{z} \right) \left(a^\dagger a + \frac{1}{2} \right) + \frac{\hbar \omega_\mathrm{a}}{2} \sigma_\mathrm{z}. \tag{2.2}$$

The first term describes the cavity as a harmonic oscillator with an effective resonance frequency of $\omega_\mathrm{r}' = \omega_\mathrm{r} \pm g^2/\Delta$, depending on the state of the atom. This dispersive shift of $2g^2/\Delta$ can be used to infer the atom state by measuring the cavity frequency [18]. Since the Hamiltonian has no terms which would allow an exchange of energy this measurement is a *quantum non-demolition measurement* (QND) of the atom state.

Rewriting the dispersive Hamiltonian

$$H_\mathrm{disp} = \hbar \omega_\mathrm{r} \left(a^\dagger a + \frac{1}{2} \right) + \frac{\hbar}{2} \left(\omega_\mathrm{a} + \frac{2g^2}{\Delta} a^\dagger a + \frac{g^2}{\Delta} \right) \sigma_\mathrm{z}. \tag{2.3}$$

one can see that the dispersive interaction acts equally on the atom state. The second term shows that the effective transition frequency of the atom is shifted by the photon number of the cavity, known as the *ac-Stark shift*. We will see in the experiment chapter 5 that this allows to perform a QND measurement of the photon number in the cavity. The constant term g^2/Δ in the effective transition frequency is known as the Lamb shift and was measured successfully amongst others in Ref. [19].

Vacuum Rabi Splitting

When the detuning between cavity and atom goes to zero for a system in the strong coupling regime, cavity and atom cannot be regarded as individual systems anymore. Formally this means that the atom and photon states are no longer eigenstates of the Hamiltonian. Instead, the symmetric and and anti-symmetric superposition states

$$|n, \pm\rangle = (|g\rangle|n+1\rangle \pm |e\rangle|n\rangle)/\sqrt{2} \tag{2.4}$$

are the new eigenstates of the system. For a given n, the energies of these states would be degenerate in the uncoupled system and split up by $2\sqrt{n}\hbar g$ due to the coupling which is known as the *vacuum Rabi mode splitting*. In this situation the atom and the cavity constantly exchange excitations back and forth, which will be presented as time-resolved vacuum Rabi oscillations in the experimental part of this thesis. A cavity QED system in this limit behaves strongly non-linear due to the strong interaction leading to a wealth of interesting physical effects as, e.g.t̃he vacuum Rabi super-splitting [20] or the photon blockade [21].

2.2. Circuit QED

The circuit QED setup as proposed in Ref. [1] and demonstrated in Ref.[2] is a way to implement a cavity QED system using superconducting electronic circuits. A schematic of the setup used in our laboratory is found in Fig. (2.2). The cavity in this system is realized by a finite length superconducting coplanar wave guide which is capacitively coupled to microwave transmission lines. In this configuration the gaps in the center conductor act as mirrors and define a single electromagnetic mode, typically in the lower GHz range. The coupling to the transmission lines can be tuned by the design of these capacitances, where a smaller capacitance leads to a smaller coupling or equivalently to a higher reflectivity of the mirrors. By using high quality dielectrics and superconducting metals the internal loss in these type of cavities can be minimized and quality factors of up to $Q > 10.000$ [22, 23] are achievable.

The atom in the cavity QED setup is replaced by an electronic device with anharmonic quantized energy spectrum. Different devices were successfully implemented based on the insulating tunnel barrier between two superconducting electrodes known as the *Josephson tunnel junction*, depicted in Fig. (2.2c). One possible implementation is the *split Cooper pair box* (CPB) where two Josephson junctions are connected in a ring as in Fig. (2.2b). In the two superconducting regions the electric charge carriers (Cooper pairs) have a macroscopic wavefunction which overlap in the insulator allowing them to tunnel coherently between the lower superconducting region (reservoir) and the upper superconducting part (island). This device

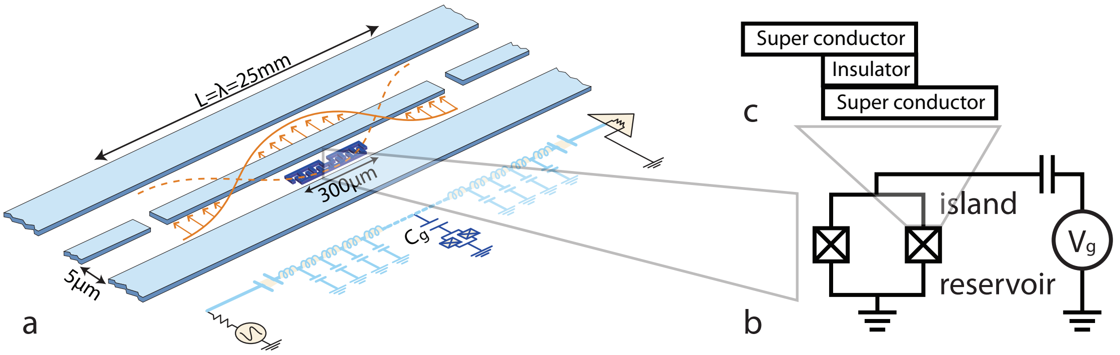

Figure 2.2.: **a)** Schematics of the circuit QED setup. The coplanar waveguide from a superconducting metal (light blue) defines a microwave cavity by the two gap capacitors. The transmon qubit (dark blue) is placed at an anti-node of the electric field. **b)** Circuit diagram of the split Cooper pair box. **c)** Schematic of the Josephson Junction

can effectively be described as a single quantum system with the number of excess Cooper pairs N on the island as a good quantum number. The corresponding eigenstates $|N\rangle$ form a complete basis for the states of the box and allow us to write down the Hamiltonian for the system [24] as

$$H_{\mathrm{CPB}} = 4E_{\mathrm{c}} \sum_N (N - N_{\mathrm{g}})^2 |N\rangle\langle N| - \frac{E_{\mathrm{J}}}{2} \sum_N (|N+1\rangle\langle N| + |N\rangle\langle N+1|). \tag{2.5}$$

The first term describes the electrostatic energy of the excess Cooper pairs on the island. The *charging energy* for one additional charge carrier on the island is $E_{\mathrm{c}} = e^2/2C_\Sigma$, where the capacity C_Σ is the overall capacity between island and reservoir. The gate charge $N_{\mathrm{g}} = C_{\mathrm{g}}V_{\mathrm{g}}/2e$ in this term is determined by the potential difference between island and reservoir V_{g} and allows to tune the average number of excess carriers on the island. The second term describes the coherent tunneling of the Cooper pairs at a rate $E_{\mathrm{J}}/\hbar$ determined by the *Josephson coupling energy* E_{J}. This coupling energy is related to the critical current I_{c} through the junctions by $E_{\mathrm{J}}(\Phi) = I_{\mathrm{c}}(\Phi)\Phi_0/2\pi$ and depends on the flux Φ through the loop of the CPB. By adjusting an external magnetic field the Josephson energy can be tuned as $E_{\mathrm{J}} = E_{\mathrm{J,max}}|\cos(\pi\Phi/\Phi_0)|$.

In the limit where $E_{\mathrm{c}} \gg E_{\mathrm{J}}$ the CPB is referred to as a charge qubit because the charging energy term dominates the Hamiltonian. Although CPBs in this regime were successfully used as qubits they show a strong sensitivity to noise in the gate charge N_{g}. In our experiments we use a modified version of the CPB with a large additional capacitance between island and reservoir, which was proposed as the *transmon qubit* in Ref. [25]. This transmon is a charge qubit in the limit $E_{\mathrm{c}} \ll E_{\mathrm{J}}$ which makes it insensitive to charge noise, because the contribution of the electrostatic term in the Hamiltonian is less dominant. Although this also leads to a strong reduction of the anharmonicity it was shown that it still remains sufficiently large.

The transmon qubit can be coupled via a dipole interaction to a microwave resonator by placing it at an anti-node of the electric field mode. The Hamiltonian of the joint system can be written in terms of the eigenstates of the uncoupled transmon $|i\rangle$

$$H = \hbar \sum_i \omega_i |i\rangle\langle i| + \hbar\omega_\mathrm{r} \left(a^\dagger a + \frac{1}{2} \right) + \sum \hbar g_{i,j} |i\rangle\langle j| (a^\dagger + a). \tag{2.6}$$

and is known as a generalized Jaynes-Cummings Hamiltonian [25]. This Hamiltonian can be simplified by applying the rotating wave approximation and the reduction of the transmon to an effective two level system [25]. The result is equivalent to the Jaynes-Cummings Hamiltonian in Eq. (2.1) which shows that the circuit QED system is an implementation of the cavity QED setup.

Dispersive read-out of the qubit state

To read out the state of the qubit we can use the dispersive approximation of the Jaynes-Cummings Hamiltonian presented in Eq. (2.2) in the case where the qubit is strongly detuned from the resonator $|\Delta| = |\omega_\mathrm{ge} - \omega_\mathrm{r}| \gg g$. Although for the transmon qubit higher level transitions cannot be neglected, one can find an effective dispersive Hamiltonian [25]

$$H_\mathrm{disp,eff} = \frac{1}{2} \hbar\omega'_\mathrm{a} \sigma_\mathrm{z} + (\hbar\omega'_\mathrm{r} + \hbar\chi\sigma_\mathrm{z}) a^\dagger a \tag{2.7}$$

similar to Eq. (2.2). Here the qubit frequency $\omega'_\mathrm{a} = \omega_\mathrm{ge} + g_\mathrm{ge}^2/\Delta$ and resonator frequency $\omega'_\mathrm{r} = \omega_\mathrm{r} - g_\mathrm{ef}^2/2\Delta$ are renormalized due to higher level transitions and the dispersive shift of the resonator frequency is approximately given by

$$\chi = -g^2 \frac{E_\mathrm{c}/\hbar}{\Delta(\Delta - E_\mathrm{c}/\hbar)}. \tag{2.8}$$

This shift is detected [18] by applying a continuous coherent microwave signal at a frequency ω_meas to the resonator starting at the time $t = 0$. Including the measurement drive the Hamiltonian in the frame rotating at the measurement frequency is

$$H_\mathrm{meas} = \frac{1}{2} \hbar\omega'_\mathrm{a} \sigma_\mathrm{z} + (\hbar\omega'_\mathrm{r} - \hbar\omega_\mathrm{meas} + \hbar\chi\sigma_\mathrm{z}) a^\dagger a + \hbar\epsilon(t)(a^\dagger + a), \tag{2.9}$$

where $\epsilon(t)$ is the time dependent amplitude of the measurement tone. Measuring the radiation coming from the cavity by homodyne detection we can infer a complex valued signal

$$S(t) = \sqrt{Z\hbar\omega_\mathrm{meas}\kappa}\, \langle a(t) \rangle\,, \tag{2.10}$$

which gives us the time evolution of the expectation value of the annihilation operator, where Z is the characteristic impedance of the system. This signal is different for the qubit in the $|g\rangle$ or in the $|e\rangle$ state due to the dispersive shift of the resonator and can be predicted theoretical by solving the *cavity Bloch equations* [26]. By comparing the measurement with the theoretical prediction the population of the excited state

$$P_\mathrm{e} = (\langle \sigma_\mathrm{z} \rangle + 1)/2 \tag{2.11}$$

can be extracted. The frequency of the measurement drive is chosen typically close or identical to the resonator frequency, because the effect of the dispersive shift is most strong in this frequency range. Although we only considered average values here, this type of measurement also allows for single shot readout [27] and can even be extended to read out the populations of higher transmon levels [28].

Qubit state control

Using coherent microwave signals one can not only read out but also coherently control the qubit state. This can be achieved by applying a microwave tone close to the qubit transition frequency ω'_a when the qubit is strongly detuned from the resonator. Although most of the radiation is reflected by the resonator, a sufficient part will enter and interact with the qubit. The coherent driving field is considered a classical field with an amplitude $\epsilon_\mathrm{d}(t)$ and a frequency ω_d and can be included into the following effective Hamiltonian [17]

$$H_\mathrm{drive} = (\hbar\omega'_\mathrm{r} - \hbar\omega_\mathrm{d})a^\dagger a + \frac{1}{2}(\hbar\omega'_\mathrm{a} - \hbar\omega_\mathrm{d} + 2\hbar\chi(a^\dagger a + \frac{1}{2}))\sigma_\mathrm{z} + \frac{\hbar\Omega(t)}{2}\sigma_\mathrm{x}, \tag{2.12}$$

where we introduced the *Rabi frequency* $\Omega(t) = \frac{2\epsilon_\mathrm{d}(t)}{\omega'_\mathrm{r} - \omega_\mathrm{d}}$. This control parameter allows to rotate the qubit state vector on the Bloch sphere around the x-axis, or, by adjusting the phase of the drive signal also around the y-axis. The rate at which the state vector rotates around the x-axis is given by the Rabi frequency and is controlled via the amplitude of the driving signal. Neglecting rotations around the z-axes, the overall rotation around the x-axis is characterized by the *Rabi angle* $\theta_\mathrm{r} = \int \Omega(t)dt$. By creating a pulse where the amplitude and length are chosen such that for example $\theta_\mathrm{r} = \pi$ the qubit can be excited from the ground to the excited state. For arbitrary Rabi angles the final qubit state reads

$$|\psi_\mathrm{q}\rangle = \cos(\theta_\mathrm{r}/2)|g\rangle + \sin(\theta_\mathrm{r}/2)|e\rangle. \tag{2.13}$$

3. Measurement Setup

In this chapter we will describe the sample and the experimental setup used in the Quantum Device Laboratory at ETH Zurich to perform the experiments presented in this thesis.

3.1. Sample

Our experiments were performed in the circuit QED device depicted in Fig. (3.1a) implemented on a 500 μm thick sapphire (Al_2O_3) substrate. The largest feature in Fig. (3.1a) is the microwave cavity, fabricated as a coplanar waveguide in a photo-lithographic process using niobium which is superconducting below $T_{\mathrm{c,Nb}} = 9.2\,\mathrm{K}$. The internal loss of such a cavity can be minimized which reflects in internal quality factors reaching [29] $Q_{\mathrm{int}} \gg 10.000$. In this sample the loss of the of cavity is dominated by the external loss to the two output ports, which can be engineered by adjusting the coupling capacitors at both ends of the cavity, see Fig. (3.1b). In our sample the external quality factor is $Q_{\mathrm{ext}} = 2060$ which corresponds to a decay rate of $\kappa/2\pi = 3.12\,\mathrm{MHz}$. The resonance frequency $\nu_{\mathrm{r}} = 6.433\,\mathrm{GHz}$ is determined by the length of the resonator which is in our sample about 10 mm. To reduce the overall sample size the cavity can be fabricated in a meandering form without changing its basic properties.

On the right hand side of the cavity on an anti-node of the cavity field, a transmon qubit was placed, see Fig. (3.1c), using shadow evaporation as described in Ref. [30]. In this process the Josephson junctions are created by depositing a first layer of aluminum which is oxidized to amorphous Al_2O_3 on the surface, followed by a second layer of aluminum constituting the second electrode of the junctions. The coupling constant g and the charging energy E_{c} can be designed by the capacitances of the island and the reservoir to the ground plane and the center conductor and were measured to be $g = 54\,\mathrm{MHz}$ and $E_{\mathrm{c}}/h = 475\,\mathrm{MHz}$. To make the Josephson energy tunable the transmon was implemented using a split CPB with a loop area of $3 \times 4\,\mu\mathrm{m}^2$ with a maximal energy of $E_{\mathrm{J,max}}/h = 16.2\,\mathrm{GHz}$ in our sample. This allows a static tuning of the qubit frequency using a miniature coil positioned below the sample. Additionally, a local flux control line as investigated by L. Steffen [31] was placed in the vicinity of the CPB loop. The transmission line is shorted right before the qubit, such that short current pulses allow to change the flux through the CPB on short time scales and thereby change its transition frequency. This can be used to control the effective qubit-resonator interaction by tuning them in and out of resonance.

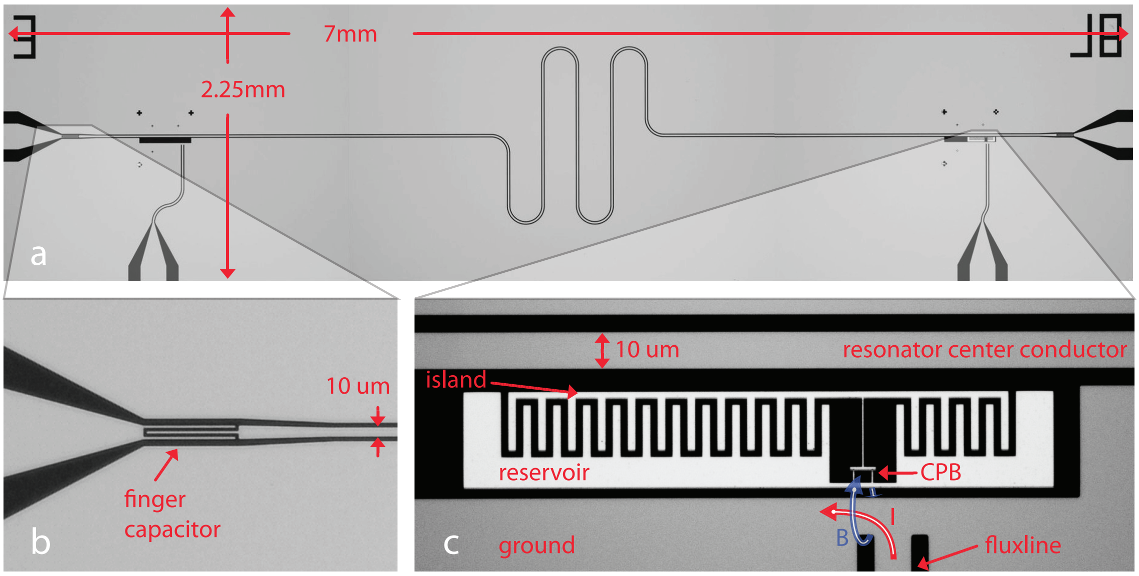

Figure 3.1.: **a)** Circuit QED device with meandering microwave resonator coupled to two output ports (left and right). **b)** Coupling capacitor at the left port. **c)** A transmon qubit is coupled capacitively to the resonator. The magnetic flux through the CPB is controlled by a static field and dynamically by a current I induced through the flux line (lower port).

3.2. Cryogenics and filtering

To be able to observe quantum effects in the microwave regime it has to be ensured that the thermal occupation of all relevant degrees of freedom is well below one quantum of energy. In our system this energy is given by a single microwave photon with an energy of about $h\nu_r = 4 \times 10^{-24}$ J. This limits the temperature as

$$k_B T \ll h\nu_r. \tag{3.1}$$

This condition can be satisfied by using a *dilution refrigerator* [32] which can reach temperatures of around 20 mK corresponding in thermal equilibrium to a thermal occupation below 10^{-6} energy quanta. The dilution refrigerator used in our experiments employs a *pulse tube cooler* [33] with a helium working medium to precool the first two stages to 70 K and 4 K. From there the cooling to 20 mK on the lowest stage is achieved by extracting heat through the evaporation of ^{3}He in a ^{3}He^{4}He mixture. While the absolute temperatures are very low the cooling power on the lowest stage is only on the order of several μW. This is why one of the critical design goals in the setup is to minimize the heat load to the lowest temperature stage.

The most part of the heat load stems from thermal conductivity of the cables and can be reduced by using stainless steel cables with a significantly lower conductivity ($\sim 0.1\,\mathrm{W/(m\cdot K)}$) than regular copper cables ($\sim 20\,\mathrm{W/(m\cdot K)}$). Additionally all microwave input lines are equipped with attenuators at different temperature stages to thermalize the outer and inner conductor to the respective temperatures (Fig. (3.2)). At the same time the attenuators reduce thermal radiation emitted by the room temperature equipment, so that not only the physical temperature (lattice vibrations) but also the electromagnetic field temperature (photon excitations) in the sample stays cold.

These techniques are not applicable for the flux line, which has to be able to supply a significant current for the flux tuning of the qubit. Placing attenuators in this line would lead to electrical dissipation beyond the cooling power of the cryostat. Therefore the only attenuation is placed on the 4 K stage followed by two non-dissipative 400 MHz low pass filters. These filters protect the qubit from high frequency flux noise while retaining enough bandwidth for fast tuning of the qubit frequency. This configuration proved to be a successful compromise between heating of the lowest temperature stage and noise injected to the qubit.

As a final measure to reduce the thermal radiation entering the sample two circulators were installed between the sample and two amplifiers on the output lines. These circulators act as a one way valve for the microwave radiation, which can only travel in one direction indicated by the arrows in Fig. (3.2). In this way the noise emitted by the amplifiers towards the sample is filtered out and is deposited in the $50\,\Omega$ termination on the third port of the circulator. Additionally we use one of the lower circulators to connect a microwave input line, such that one port of the resonator can be used as an input and both ports as measurement outputs.

3.3. Signal generation

To carry out the experiments, a variety of electrical high and low frequency signals need to be send to our sample. These signals are produced by room temperature equipment and can be divided into the following groups:

- Synchronization and trigger signals
- Continuous microwave signals for sample characterization, qubit read-out and qubit spectroscopy
- Pulsed coherent microwave signals for qubit state preparation
- Pulsed low frequency/d.c. signals for qubit frequency tuning through the flux line

Synchronization and triggering

To perform high precision preparation and measurement of the qubit state all devices need to be commonly synchronized, as depicted in Fig. (3.3.) This is achieved by phase locking each device to a common 10 MHz reference provided by a Rubidium clock (SRS FS745). This clock is stabilized against drifts in the clock frequency and provides a reference signal with ultra-low phase noise.

The sequence of steps are performed during one realization of an experiment is defined by the Tektronix 5014 *arbitrary waveform generator* (AWG). For each experiment the AWG plays back a set of signals which switch the microwave sources on and off and trigger the beginning

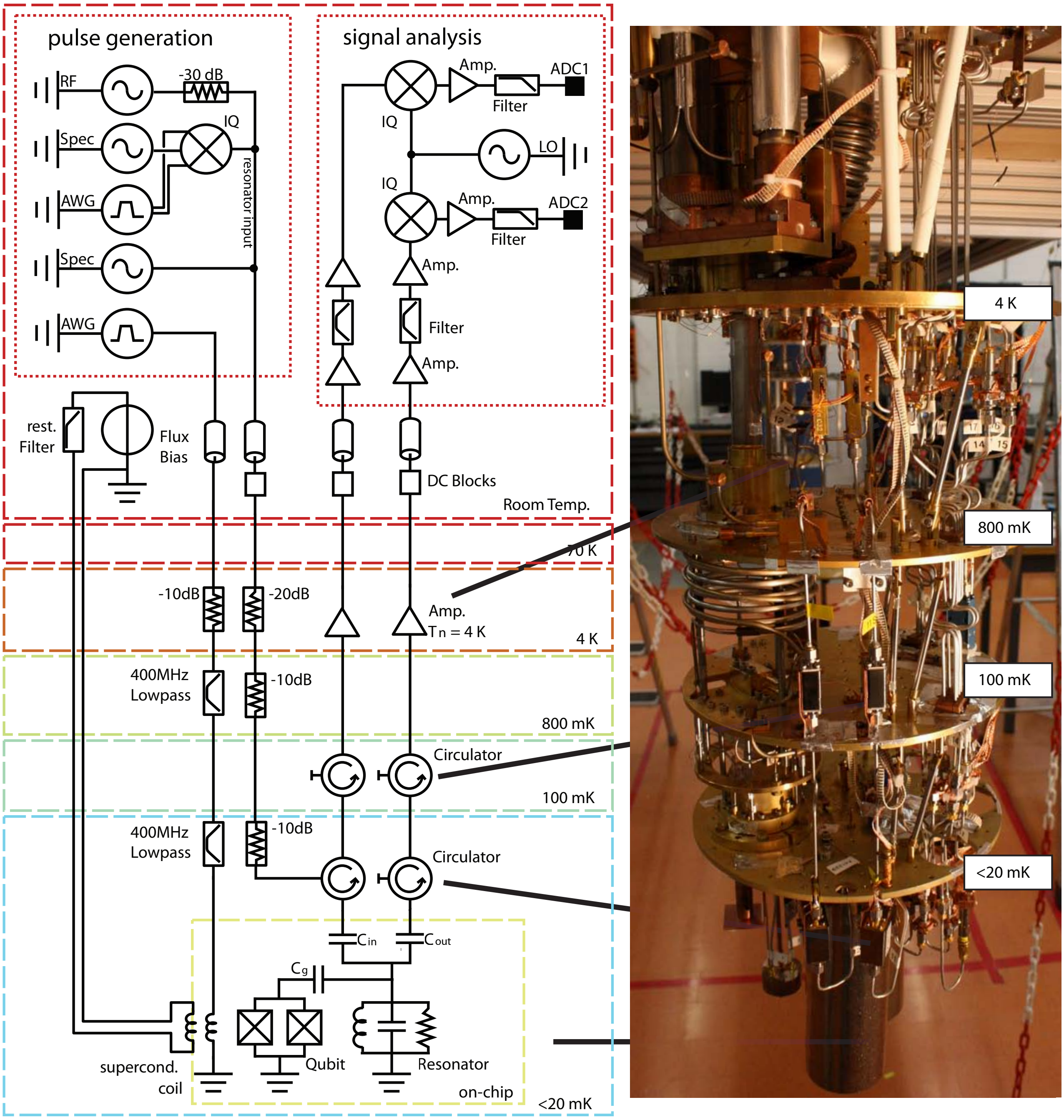

Figure 3.2.: Left: Schematics of the experimental setup. At room temperature (top) signal generation and signal acquisition systems are depicted. Inside of the cryostat five temperature stages are equipped with different components to achieve lowest temperature and lowest noise levels at the sample. Right: Photo of the open cryostat with indications of the relevant devices and temperature stages.

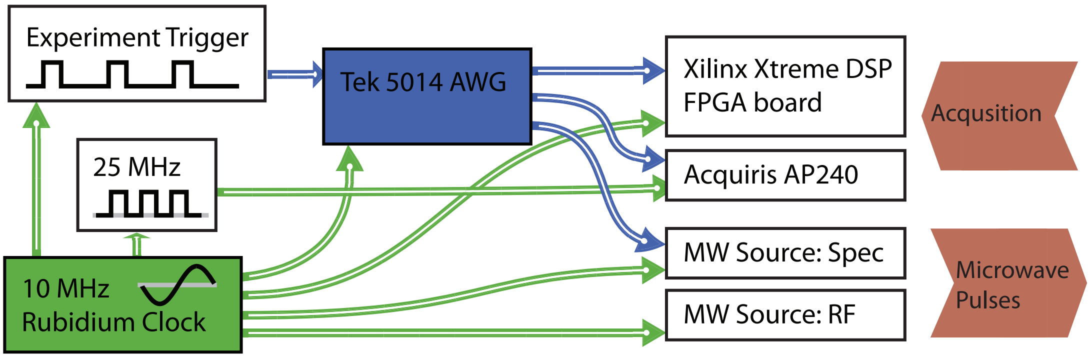

Figure 3.3.: Synchronization of the measurement setup. Green: 10 MHz phase lock signal, Blue: trigger signals.

of the measurement for the two data acquisition cards. Typically many repetitions of an experiment are performed to acquire enough information. These repetitions are controlled by a free running external trigger starting a new experiment every 20-100 μs.

Continuous microwave signals

For sample characterization we use continuous microwave signals generated by Agilent E825X microwave sources, see Fig. (3.2). One source (RF) is used to measure the transmission through the microwave resonator on the sample and can be switched on and off by the AWG for qubit state measurements. The other source (Spec) is used to excite the qubit in spectroscopic measurements.

Pulsed microwave signals

For the controlled preparation of qubit states we use microwave pulses generated by modulating a continuous microwave signal with an IQ-mixer, see Fig. (3.4a). The IQ-mixer is driven by a high power continuous microwave signal with frequency ω_{LO} through its *local oscillator* (LO) port. This LO signal get modulated by the I and the Q signal provided by the AWG which we will write as a combined complex modulation signal $s_{\mathrm{mod}}(t) = I(t) + iQ(t)$. Then, the signal emitted from the RF port of the mixer can be written as

$$E_{\mathrm{RF}}^{(+)}(t) = s_{\mathrm{mod}}(t)e^{-i\omega_{\mathrm{LO}}t} = (I(t) + iQ(t))e^{-i\omega_{\mathrm{LO}}t}. \tag{3.2}$$

On each channel I and Q the AWG can provide signals with a bandwidth of 500 MHz, limited by its sampling rate of 1 GHz. Since these two channels represent the real and imaginary part of the modulation signal s_{mod} we can distinguish positive and negative frequencies in this signal and thus can generate pulses within a band of up to 1 GHz centered at the LO frequency (Fig. (3.4c)). One of the limiting imperfections of the mixer is the leakage of radiation from the LO port to the RF port which can have significant influence on the experiment. To

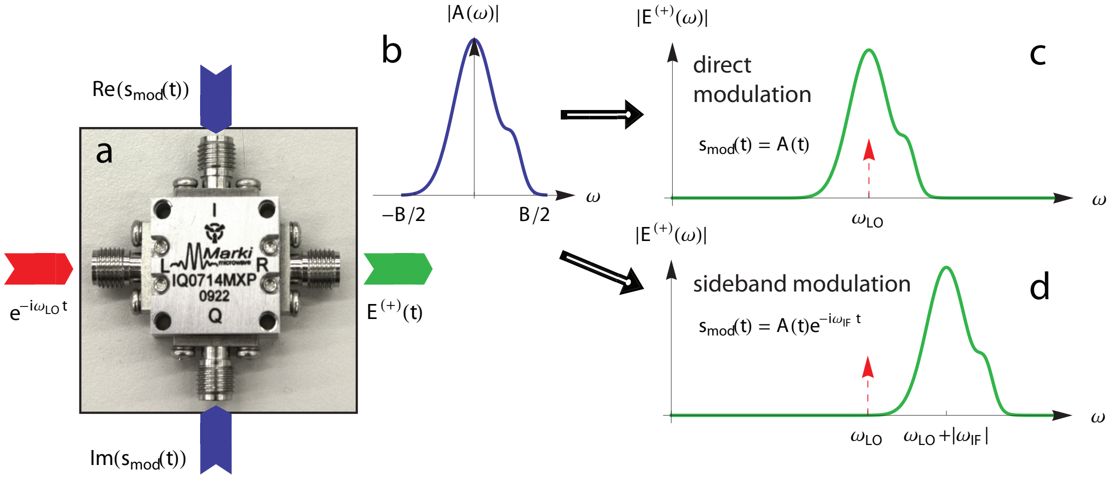

Figure 3.4.: **a)** Generation of microwave pulses by an IQ mixer where the LO signal (red) is modulated by a signal $s_{\text{mod}}(t)$. A pulse with a shape $A(t)$ **(b)** can be generated by direct modulation **(c)** or sideband modulation where the leakage at the LO frequency (red) does not lie in the band of the pulse **(d)**.

mitigate the impact of this leaking radiation we apply so-called *single sideband modulation* of our microwave pulses. In this case the modulation signal is not given by the shape $A(t)$ of the desired pulse but by $s_{\text{mod}}(t) = A(t)e^{-i\omega_{\text{IF}}t}$ where we choose an intermediate frequency ω_{IF} of typically 100 MHz. The resulting pulse is then described by

$$E^{(+)}_{\text{RF}}(t) = A(t)e^{-i(\omega_{\text{LO}}+\omega_{\text{IF}})t}, \tag{3.3}$$

and centered around $\omega_{\text{LO}} + \omega_{\text{IF}}$ as shown in Fig. (3.4). The leakage is now at a different frequency than the pulse where it typically does not influence the experiment. Note that the intermediate frequency can be chosen positive or negative, also denominated as *upper* and *lower sideband modulation* respectively.

Pulsed low frequency signals

For the control of the qubit frequency via the flux line [31] we prepare low frequency pulses with a bandwidth from d.c. up to 500 MHz. These pulses are subject to several imperfections which have to be corrected to achieve high fidelity operation. First we correct for the distortion of the pulses introduced by the AWG and the transmission line including the filters by the method described in App. A. Furthermore we have to compensate for the non-zero voltage offset which the AWG outputs when a digital zero is programmed. This offset is presumably due to imperfections in the AWG electronics and stabilizes only after several hours of continuous operation of the AWG to a magnitude of $\pm 1 - 10$ mV. This effect becomes more pronounced for asymmetric output ranges e.g. $+1$ V to -3 V where the offset can exceed 10 mV. The offset is compensated using a d.c. voltage source connected to the AWG's *add input port* such that digital zero and a turned off channel have both the same voltage of exactly 0.000 V.

3.4. Signal acquisition

To detect the radiation coming out of the microwave resonator we installed two detection chains at each output of the resonator as depicted in Fig. (3.2). The measurements which take place at a single photon level are enabled by the use of cryogenic low noise amplifiers (LNA) installed at the 4K stage of the cryostat. These amplifiers are implemented using high electron mobility transistors (HEMT) and define the amount of noise in the detection system. The noise level is quantified by the noise temperature which is the equivalent temperature of a black body radiator in front of a noiseless amplifier producing the same amount of noise as our system. Frii's law for the noise temperature shows that the system noise temperature is dominated by the first device in the detection chain

$$T_{\text{sys}} = T_{\text{LNA}} + \frac{T_{\text{rest}}}{G_{\text{LNA}}}, \tag{3.4}$$

because the power gain of the first amplifier $G_{\text{LNA}} \sim 33\,\text{dB} = 2000 \gg 1$. The noise temperature of the LNAs is specified at 4.5 K which poses a lower boundary to the noise performance of the total system. From measurements we can extract a much higher effective system noise temperature relative to the resonator output of $\sim 17\,\text{K}$. This is significantly (5.8 dB) higher than the LNA noise temperature due to cable and insertion losses in front of the amplifiers.

At room temperature, the signal is further amplified by $\sim 60\,\text{dB}$ to a level where it becomes detectable by digital electronics. The amplified high frequency signal is converted down to an intermediate frequency (IF) of typically 10 MHz or 25 MHz. For the down conversion we use a single sideband mixer driven by a local oscillator which is phase locked to the input microwave signals. The resulting IF signal is digitized by an *Acqiris Data Acquisition Board (AP240)* and a *Xilinx Xtreme DSP board* where data processing, averaging and recording of the measurement outcome takes place. For the details of the data processing steps involved refer to Sec. 4.2.1 and App. B.

From a technical perspective the two data acquisition boards are in use because they offer different advantages. The AP240 features a sampling period of 1 ns and automatically averages the recorded data over up to 65536 repetitions of an experiment. On two input channels it can average in total 16.7 MPoints. This device is well established and integrated into the measurement software and was used for all calibration and qubit measurements in the experiments.

The Xilinx Xtreme DSP board only features 10 ns sampling period on two channels but can be programmed to perform arbitrary operations on the data prior to averaging. A significant part of the technical work in this thesis was the implementation of a signal processing algorithm on this board to perform statistical analyses on the incoming signals. This includes the measurement of averages, powers, cross-powers and different correlation functions. The theoretical descriptions of these measurements are given in Sec. 4.3 whereas the technical details of the implementation are presented in App. B.

4. Theory

In this chapter, we present the necessary theoretical aspects to understand the experimental results presented in this thesis. Three topics will be discussed. First the *correlation functions of the electric field* are introduced as a powerful tool to characterize light sources. In the *theory of detection* we describe how these correlation functions and other observables of the system can be measured using our setup. Finally the implementation of a microwave single photon source is discussed theoretically.

4.1. Correlation functions of the electric field

Before we introduce the correlation functions of the electric field we need to establish some definitions how to talk about correlation functions. In statistical terms the correlation between any two complex variables A, B is given by

$$C = \langle A^* \cdot B \rangle \tag{4.1}$$

where $\langle \cdot \rangle$ denotes the expectation value which can be measured by ensemble averaging over many realizations of the variables. C is also called the *auto-correlation of A* when $A = B$ or the *cross-correlation between A and B* for $A \neq B$. If the variables A, B are functions of time one also considers the *time-resolved correlation function*

$$C(t, t+\tau) = \langle A^*(t) \cdot B(t+\tau) \rangle \, . \tag{4.2}$$

In many experiments the detectors perform implicitly or explicitly an integration over the time variable t so that we only have access to the *time-integrated* version of the correlation function. For a given correlation function $C(t, t+\tau)$ this is defined as

$$C(\tau) = \frac{1}{N} \int_{t_1}^{t_2} C(t, t+\tau) dt = \frac{1}{N} \int_{t_1}^{t_2} \langle A^*(t) \cdot B(t+\tau) \rangle \, dt. \tag{4.3}$$

In this expression the values for N, t_1, t_2 depend on the context and are often chosen as $N = t_2 - t_1$ and $t_1 = 0, t_2 \to \infty$.

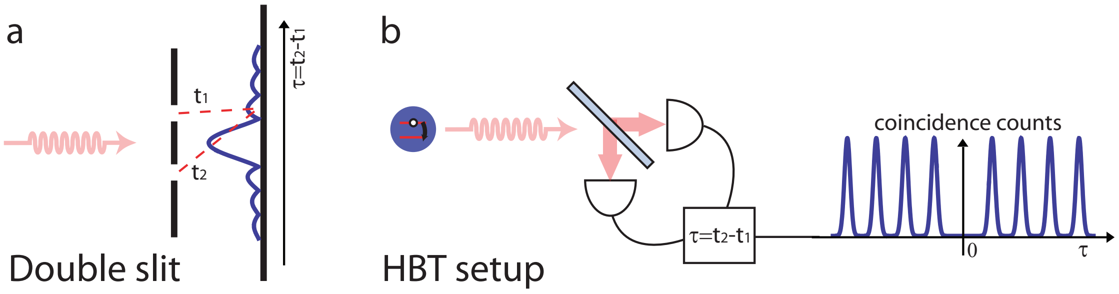

Figure 4.1.: **a**) Setup of the young double slit experiment. The incident light passes through two slits and interferes on the detector plate. The temporal resolution τ is achieved through spacial resolution using the traveling time difference of the light. **b**) Hanbury Brown Twiss setup. The incident light passes a beam splitter and is measured on both arms by photon detectors. The following electronics extracts the photon-photon arrival time distribution which is a direct measurement of the second order correlation function.

4.1.1. First-order correlation function

One of the first experiments measuring an electric field correlation function were performed by Thomas Young in 1802. In his famous double slit experiment depicted in Fig. (4.1a) one observes interference fringes in the intensity after an opaque wall with two slits. In the double-slit experiment the observed intensity is given in terms of the electric field $E(t)$ and its intensity $I(t) = E^*(t)E(t)$ by

$$\begin{aligned} I &= \langle (E^*(t) + E^*(t+\tau))(E(t) + E(t+\tau)) \rangle \\ &= \left\langle I(t) + I(t+\tau) + \underbrace{E^*(t)E(t+\tau)}_{G^{(1)}} + E^*(t+\tau)E(t) \right\rangle \\ &= \left\langle I(t) + I(t+\tau) + 2\Re\{G^{(1)}(t,t+\tau)\} \right\rangle . \end{aligned} \tag{4.4}$$

The time shift τ is the traveling time difference between the two possible paths and can be resolved spatially on the detector plate. If the source is stationary such that $\langle I(t) \rangle = \langle I(t+\tau) \rangle = I_0$ this expression simplifies to

$$I = 2I_0 + 2\Re\left\langle G^{(1)}(t,t+\tau) \right\rangle . \tag{4.5}$$

The factor

$$G^{(1)}(t,t+\tau) = \langle E^*(t)E(t+\tau) \rangle \,, \tag{4.6}$$

is the origin of the interference fringes and is known as the *first-order correlation function* of the electric field, or also the *temporal coherence function*.

In a quantum mechanical treatment of the electric field we can use the relation

$$E^{(+)}(t) = \left(i\sqrt{\hbar\omega/2\epsilon V} \right) a \cdot e^{-i\omega t} \tag{4.7}$$

where a is the annihilation operator, ω the frequency, V the volume of the the relevant field mode and ϵ the dielectric constant. The first-order correlation function is then written as

$$G^{(1)}(t, t+\tau) = \left\langle a^{\dagger}(t) a(t+\tau) \right\rangle = \operatorname{tr}\left\{\rho a^{\dagger}(t) a(t+\tau)\right\}, \tag{4.8}$$

where ρ is the density operator describing the state of the mode a. Constant prefactors were dropped here to match the commonly used form. For a coherent field state $|\alpha\rangle$ this correlation function is constant for all times τ and given by

$$G^{(1)}(t, t+\tau) = |\alpha|^2 . \tag{4.9}$$

The fact that the correlation stays constant for $\tau \to \infty$ is known as *coherence* and is the characteristic property of a coherent field. In contrast, a chaotic light source in a thermal state ρ shows minimal temporal coherence and has

$$G^{(1)}(t, t+\tau) = n_{\text{th}} \delta(\tau), \tag{4.10}$$

where $\delta(\tau)$ is the Dirac delta distribution and $n_{\text{th}} = \operatorname{tr}\{\rho n\}$ the thermal population of the source.

4.1.2. Second-order correlation function

The other correlation function of great interest is the field intensity auto-correlation

$$G^{(2)}(t, t+\tau) = \langle I(t) I(t+\tau) \rangle \tag{4.11}$$

also known as the the *second-order correlation function*. In the quantum-mechanical formulation introduced by Glauber $G^{(2)}$ is expressed in terms of the field operators as

$$\begin{aligned} G^{(2)}(t, t+\tau) &= \langle : I(t) I(t+\tau) : \rangle \\ &= \left\langle : a^{\dagger}(t) a(t) a^{\dagger}(t+\tau) a(t+\tau) : \right\rangle \\ &= \left\langle a^{\dagger}(t) a^{\dagger}(t+\tau) a(t) a(t+\tau) \right\rangle . \end{aligned} \tag{4.12}$$

In this expression $\langle : \cdot : \rangle$ denotes an average where all operators are *normally ordered* such that all annihilation operators are placed right of all creation operators.

The first experiments to measure this function were performed by Hanbury Brown and Twiss (HBT) in the context of stellar interferometry [34] in 1956. Their setup in Fig. (4.1b) splits an incident beam in equal parts which are measured by photon detectors. When two photons arrive at the detectors the arrival time difference τ between the two is measured and its probability distribution is extracted. This photon-photon arrival time distribution is then a direct measurement of $G^{(2)}(\tau)$.

There are two important effects which can be observed in the second-order correlation function. In the case of classical light sources it can be shown that

$$G^{(2)}(0) \geq G^{(2)}(\tau). \tag{4.13}$$

The interpretation is that the detection of two photons simultaneously is more probable than one after another. In other words photons tend to arrive in *bunches*, which is why this effect is known as *photon bunching* [35].

In contrast we find for a field in a Fock state $|n\rangle$ that

$$G^{(2)}(0) = n^2 - n \quad \text{and} \quad G^{(2)}(\tau) = n^2, \tag{4.14}$$

so that $G^{(2)}(0) \leq G^{(2)}(\tau)$. Here the opposite interpretation is true: the photons tend to arrive after one another, called *photon antibunching*. For the Fock state $|1\rangle$ this effect can be understood graphically in the HBT experiment setup. On arriving at the beam splitter the photon being the smallest quantum of energy cannot split, but has to choose between left and right. The probability to detect two photons at the same time in both arms is therefore zero which is expressed by $G^{(2)}(0) = 0$.

In contrast to photon bunching, photon antibunching is a purely quantum-mechanical effect and cannot be treated by classical physics because it arises through the energy quantization of the electric field. Measurements of the second-order correlation function therefore make it possible to probe if the source under investigation emits classical or non-classical light. In the microwave regime we are not aware of any direct observation of photon antibunching by correlation measurements up to now.

4.2. Detection

Measuring correlation functions to characterize light sources is a well established method in the field of modern quantum optics. Most experimental setups are variations of the HBT setup or the Young's double slit and use beam splitters and photon detectors/counters. These methods are well understood and theoretically documented.

However, in the microwave regime where our experiments take place no photon detectors are available at present. Instead classical microwave components such as linear amplifiers and mixers are used to detect radiation. These types of devices are uncommon in a quantum optics context and are therefore less integrated in the methodology of quantum optics.

In the following we discuss our detection scheme from two perspectives. First we discuss which physical quantity we measure and how it is accessible using classical signal processing. Secondly we relate these measurements to the quantum mechanical observables of the resonator field and show how this can be used to extract different kinds of information about the field.

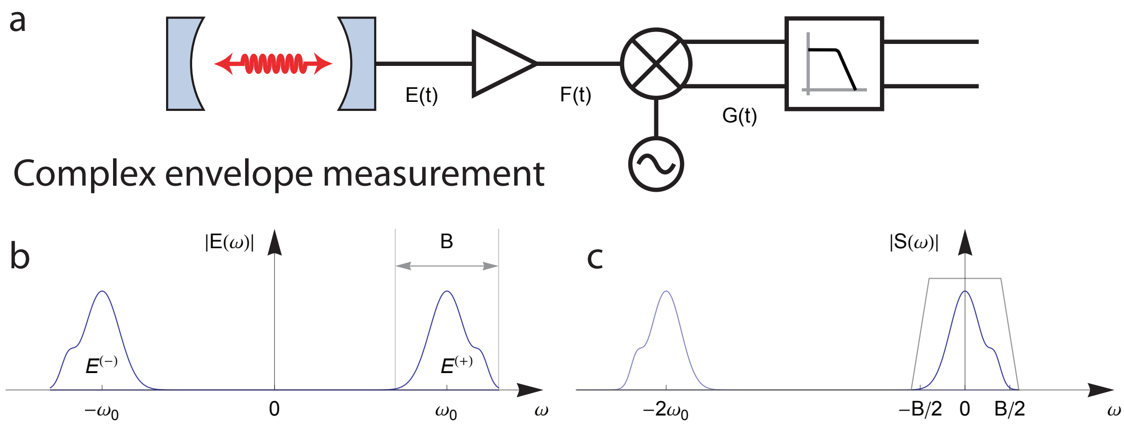

Figure 4.2.: **a**) Equivalent measurement setup for a single detection chain consisting of an amplifier, an IQ-Mixer and a low-pass filter. **b**) Schematic of E-field spectrum at the output of the cavity under the assumption of quasi-monochromatic light with bandwidth B. **c**) Schematic of the IQ-Mixer output spectrum. The following low-pass filter is indicated in gray and filters out the high frequency sideband.

4.2.1. Classical detection

The full detection setup was introduced in Sec. 3 and is depicted in Fig. (3.2). While it consist of a variety of devices including hardware and software components it can be simplified for the theoretical treatment. The equivalent[1] model has one amplifier, one IQ-mixer and one low pass filter as shown in Fig. (4.2a). The input to the detection chain is given by the electric field $E(t)$ at the first amplifiers input which is assumed to be noiseless for now. Since the electric field can only take real values we know from Fourier theory that its spectrum is hermitian symmetric [36], i.e.

$$E(\omega) = E^*(-\omega) \tag{4.15}$$

The field can then be decomposed in an incoming wave $E^{(-)}$ and outgoing wave $E^{(+)}$ which are the negative and positive frequency components of the spectrum as in Fig. (4.2b). Using this decomposition and the hermitian symmetry we can write

$$E(t) = E^{(-)}(t) + E^{(+)}(t) = \left(E^{(+)}(t)\right)^* + E^{(+)}(t). \tag{4.16}$$

We assume further that the electric field is *quasi-monochromatic* with a center frequency ω_0 and a limited bandwidth $B \ll \omega_0/2\pi$. In this case we can rewrite $E^{(+)}$ in terms of a complex valued function $S(t)$ with center frequency 0 and a bandwidth limited to B

$$E^{(+)}(t) = S(t)e^{-i\omega_0 t}. \tag{4.17}$$

---

[1] This equivalence is true under the assumptions discussed later in this section

This function $S(t)$ is called the *complex envelope of E(t)* following Ref. [36]. Using the above equations $E(t)$ can be fully described by the complex envelope as

$$E(t) = S(t)^* e^{i\omega_0 t} + S(t) e^{-i\omega_0 t}. \tag{4.18}$$

We show now that the measurement setup extracts precisely the complex envelope of the electric field at the input. After the amplifier with an amplitude amplification factor of g_{amp} we find

$$F(t) = g_{\text{amp}} E(t). \tag{4.19}$$

At the single sideband mixers output we have two signals which are the real and the imaginary part of a complex signal G(t) as in Fig. (4.2c). The real(imaginary) part is generated by the multiplication of the input signal with a local oscillator (LO) at the frequency ω_0 and phase $0\,°(90\,°)$. We find for the output signal

$$\begin{aligned} G(t) &= \underbrace{F(t)\cos(\omega_0 t)}_{I(t)} + i\,\underbrace{F(t)\sin(\omega_0 t)}_{Q(t)} \\ &= g_{\text{amp}} E(t) e^{i\omega_0 t} = g_{\text{amp}}(S(t)^* e^{2i\omega_0 t} + S(t)). \end{aligned} \tag{4.20}$$

The high frequency components oscillating at $2\omega_0$ are removed by a low pass filter of bandwidth $B_{\text{LP}} \geq B$ and we finally measure the amplified complex envelope of the input signal

$$g_{\text{amp}}(S(t)^* e^{2i\omega_0 t} + S(t)) \quad \overset{\text{low pass}}{\rightarrow} \quad g_{\text{amp}} S(t). \tag{4.21}$$

4.2.2. Quantum detection

By performing complex envelope measurement as described above we want to investigate the electric field in the resonator of our sample. To this end, both output ports of the resonator b and c are connected to a detector line and we record the two output signals $S_b(t)$ and $S_c(t)$. The resonator is in our case dominated by its quantum mechanical behavior which makes the signals we observe ultimately a quantum mechanical measurement. Such a measurement in the formalism of quantum mechanics is described by an operator acting on the quantum state of the measured system. The expectation value or average outcome of the measurement is given by

$$\langle A \rangle = \text{tr}\,\{A\rho\} \tag{4.22}$$

where A is the measurement operator and ρ is the density operator which describes the state of the system. We deduce such operators for our measurements of $S_b(t), S_c(t)$ in terms the annihilation operator of the resonator field a. In this derivation we use the Heisenberg picture, where time evolution of the system is described by time dependent operators. As a simplification, our reference system will be the frame rotating at the resonator frequency ω_{r} such that the terms of the frequency dependence $e^{-i\omega_{\text{r}} t}$ can be dropped.

As shown in Fig. (4.3a) the resonator mode a is coupled to two transmission lines with a

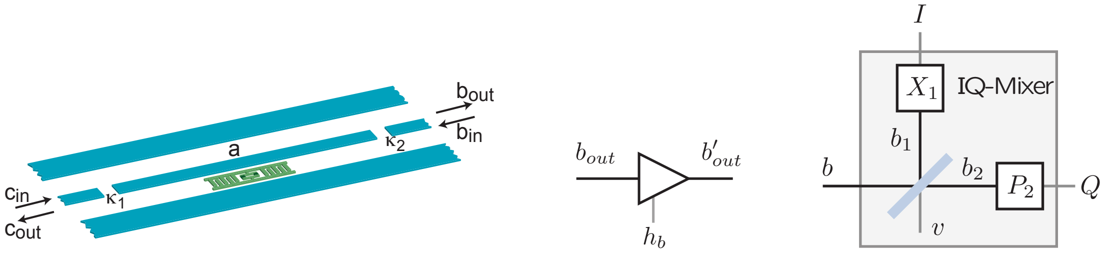

(a) Circuit QED cavity (b) Amplifier (c) IQ-mixer

Figure 4.3.: Operator description of the different parts of the detection chain. **a**) Input-output theory applied to two-port circuit QED. The two modes b and c of the transmission lines are decomposed into input c_{in}, b_{in} and output modes c_{out}, b_{out}. **b**) Schematic of a linear amplifier with an intrinsic noise mode h_b and output mode b'_{out}. **c**) Schematic of an IQ-mixer measurement of both incoming field quadratures. The vacuum mode v is an internal mode of the IQ-mixer.

coupling quantified by the decay rates κ_b, κ_c. The behavior of this system is described by the *input-output formalism* [37]. In this formalism each transmission line is described by an *input mode* $(b_{\text{in}}, c_{\text{in}})$ and an output mode $(b_{\text{out}}, c_{\text{out}})$. These modes interact with the resonator mode a obeying the following boundary conditions

$$b_{\text{out}} = \sqrt{\kappa_b}a - b_{\text{in}}, \qquad c_{\text{out}} = \sqrt{\kappa_c}a - c_{\text{in}}. \tag{4.23}$$

These equations give us a complete description of the outputs if the dynamics of the operators a, b_{in}, c_{in} are known. Note that if the total decay rate of the resonator is κ (as obtained from the linewidth), then in the symmetric case we have $\kappa_c = \kappa_b = \kappa/2$.

The output modes are connected to linear amplifiers which are formally described by the equations [38]

$$b'_{\text{out}} = g_b b_{\text{out}} + \sqrt{g_b^2 - 1}h_b^\dagger, \qquad c'_{\text{out}} = g_c c_{\text{out}} + \sqrt{g_c^2 - 1}h_c^\dagger \tag{4.24}$$

where g_i is the amplitude gain of the amplifier i and h_i the additional noise mode added by the amplifier. These internal noise modes of the amplifiers are required by quantum mechanics to preserve the commutation relations of the output modes. The output of each amplifier is finally measured by a single sideband mixer which we model as in Fig. (4.3c). The main functionality is given by an integrated 50/50 beam splitter with output modes given by $b_1 = (b + v)/\sqrt{2}$ and $b_2 = (b - v)/\sqrt{2}$, with the input mode b and the mode of the vacuum port v. On each arm of the beam splitter a mixing operation is performed corresponding to a quadrature measurement in the rotating frame of the resonator. Since the IQ-mixer performs these quadrature measurements with a 90° phase shift on the second arm we get the two measurements

$$X_1 = \frac{1}{\sqrt{2}}(b_1^\dagger + b_1) \qquad \text{and} \qquad P_2 = \frac{-i}{\sqrt{2}}(b_2 - b_2^\dagger). \tag{4.25}$$

from which we can construct a complex valued observable by the operator

$$\hat{S} = X_1 + iP_2 = b + v^\dagger. \tag{4.26}$$

Note that this observable effectively behaves like a complex number, because $\hat{S}^\dagger = \hat{S}^*$ and $\left[\hat{S}^\dagger, \hat{S}\right] = 0$ so that this measurement operator really behaves classically. To understand that $\hat{S}$ describes a complex envelope measurement we write down the quantum mechanical and the classical formulas for the electric field

$$\hat{E} \propto a + a^\dagger \qquad \longleftrightarrow \qquad E \propto s + s^* \tag{4.27}$$

and realize that there is a formal equivalence between the complex envelope and the annihilation operator.

We now have all the equations to describe our measurement in terms of the relevant system operators. Starting from Eq. (4.26) we write down the measurement results of the two detection lines as

$$\hat{S}_b = b'_{\text{out}} + v_b^\dagger, \qquad \hat{S}_c = c'_{\text{out}} + v_c^\dagger. \tag{4.28}$$

By Eq. (4.24) we get

$$\hat{S}_b = g_b b_{\text{out}} + \sqrt{g_b^2 - 1}h_b^\dagger + v_b^\dagger = g_b(b_{\text{out}} + n_b^\dagger) \tag{4.29}$$

$$\hat{S}_c = g_c c_{\text{out}} + \sqrt{g_c^2 - 1}h_c^\dagger + v_c^\dagger = g_c(c_{\text{out}} + n_c^\dagger), \tag{4.30}$$

As a simplification we combine the two sources of noise h_i and v_i to a single effective noise mode as

$$n_b = \frac{\sqrt{g_b^2 - 1}h_b + v_b}{g_b}, \qquad n_c = \frac{\sqrt{g_c^2 - 1}h_c + v_c}{g_c}. \tag{4.31}$$

Checking the commutation relation $[n_b, n_b^\dagger] = [n_c, n_c^\dagger] = 1$ shows that these effective modes behave formally correct. Inserting Eq. (4.23) we finally get the expressions

$$\hat{S}_b = g_b(\sqrt{\kappa_b}a + n_b^\dagger - b_{\text{in}}), \qquad \hat{S}_c = g_c(\sqrt{\kappa_c}a + n_c^\dagger - c_{\text{in}}). \tag{4.32}$$

4.2.3. Noise and input modes

From Eq. (4.23) we know now that the measurement on each channel is governed by three sources of radiation. On both channels we measure the resonator field a, but also the noise sources n_b, n_c and the input fields $b_{\text{in}}, c_{\text{in}}$. To investigate the resonator field we therefore have to make assumptions on the other contributions or compensate for them. For all contributions we assume that they are statistically independent, i.e.

$$\langle f_1(a) f_2(n_b, n_c) f_3(b_{\text{in}}) f_4(c_{\text{in}})\rangle = \langle f_1(a)\rangle \langle f_2(n_b, n_c)\rangle \langle f_3(b_{\text{in}})\rangle \langle f_4(c_{\text{in}})\rangle\,, \tag{4.33}$$

where the noise between the two channels is allowed to be correlated.

For the input fields we assume that they are in the vacuum state at all times. This is correct if we do not insert any radiation at the resonator frequency and thermal excitations are negligible[2]. This leads to the following expressions

$$\langle b_{\text{in}}(t)\rangle = 0, \qquad \left\langle b^\dagger_{\text{in}}(t_1) b_{\text{in}}(t_2)\right\rangle = 0, \qquad \left\langle b_{\text{in}}(t_1) b^\dagger_{\text{in}}(t_2)\right\rangle = \left[b_{\text{in}}(t_1), b^\dagger_{\text{in}}(t_2)\right] = \delta(t_2 - t_1), \tag{4.34}$$

and equivalently for mode c_{in}.

From Friis law Eq. (3.4) we know that the noise contributions are dominated by the thermal noise of the first amplifier which obey

$$\langle n_b(t)\rangle = 0, \qquad \langle n_c(t)\rangle = 0. \tag{4.35}$$

If we assume additionally a flat power spectrum of the noise [36] (white noise) we find the first order correlations of the noise

$$G_b(t, t+\tau) = \left\langle n^\dagger_b(t) n_b(t+\tau)\right\rangle = N_b \delta(\tau), \tag{4.36}$$

$$G_c(t, t+\tau) = \left\langle n^\dagger_c(t) n_c(t+\tau)\right\rangle = N_c \delta(\tau), \tag{4.37}$$

$$G_{bc}(t, t+\tau) = \left\langle n^\dagger_b(t) n_c(t+\tau)\right\rangle = N_{bc} \delta(\tau), \tag{4.38}$$

Ignoring the physical origin of the noise, we introduced effective noise photon numbers N_b, N_c, N_{bc} for the noise on each channel and for the correlated noise. It normally should be assumed that the noise between the channels is uncorrelated so that $N_{bc} = 0$, but due to technical imperfections of the measurement setup a finite level of correlated noise is always retained. For convenience we also define the anti-normally ordered noise correlations

$$H_b(t, t+\tau) = \left\langle n_b(t) n^\dagger_b(t+\tau)\right\rangle = (N_b + 1)\delta(\tau) \tag{4.39}$$

$$H_c(t, t+\tau) = \left\langle n_c(t) n^\dagger_c(t+\tau)\right\rangle = (N_c + 1)\delta(\tau). \tag{4.40}$$

4.3. Measuring different cavity observables

Using the full quantum mechanical description of our measurement process in Eq. (4.32) and the assumptions on the input and noise modes, we now describe how measurements of different resonator observables can be realized. The general strategy is to describe a mathematical transformation of the measurement data $S_b(t)$ and $S_c(t)$ before it is ensemble averaged over many repetitions of the experiment. The outcome of such a measurement is then described by using the relation $\langle f(S_b, S_c)\rangle = \langle f(\hat{S}_b, \hat{S}_c)\rangle$. Before focusing on correlation function measurements, we show how the average quadratures and the average photon number of the cavity field can be measured.

---

[2] This assumption is only approximately correct in the experiment due to incomplete thermalization of the inputs.

4.3.1. Field quadratures and photon number

A time resolved measurement of the resonator field quadratures $\langle a(t)\rangle$ is straight forward by averaging the complex envelope of either channel

$$\langle S_b(t)\rangle = g_b(\sqrt{\kappa_b}\,\langle a(t)\rangle + \underbrace{\langle n_b^\dagger\rangle}_{=0} - \underbrace{\langle b_{\text{in}}\rangle}_{=0}) = g_b\sqrt{\kappa_b}\,\langle a(t)\rangle\,. \tag{4.41}$$

To measure the average resonator photon number $\langle n(t)\rangle$ we take the absolute square of the data from one channel corresponding to the instantaneous power and find by averaging

$$\begin{aligned}\left\langle S_b^\dagger(t)S_b(t)\right\rangle &= \left\langle g_b^2(\sqrt{\kappa_b}a^\dagger + n_b - b_{\text{in}}^\dagger)(\sqrt{\kappa_b}a + n_b^\dagger - b_{\text{in}})\right\rangle\\ &= g_b^2(\kappa_b\,\langle a^\dagger a\rangle + \left\langle n_b n_b^\dagger\right\rangle + \left\langle b_{\text{in}}^\dagger b_{\text{in}}\right\rangle)\\ &= g_b^2(\kappa_b\,\langle n(t)\rangle + (N_b+1)\delta(0)),\end{aligned} \tag{4.42}$$

where $\delta(0)$ is finally a finite factor given by the effective detection bandwidth. This average photon number measurement is possible but has a constant offset given by the noise power of the amplifier which is $N_b \gg \langle n(t)\rangle$.

This background noise power can be significantly reduced by using both channels and measuring the instantaneous *cross-power* between both channels

$$\left\langle S_b^\dagger(t)S_c(t)\right\rangle = g_b g_c(\sqrt{\kappa_b\kappa_c}\,\langle n(t)\rangle + N_{bc}\delta(0)), \tag{4.43}$$

where N_{bc} is the power of the correlated noise defined in Eq. (4.38). Since the noise on both channels is mostly uncorrelated we expect $N_{bc} \ll N_b$ and as such an improved measurement of $\langle n(t)\rangle$.

4.3.2. First-order correlation function

For measurements of the first-order correlation function $G^{(1)}(\tau)$ we present two alternative methods using one or both channels.

One Channel

Using only the channel b we analyze the measurement given by

$$\Gamma^{(1A)}(\tau) = \int \left\langle S_b^\dagger(t)S_b(t+\tau)\right\rangle dt \tag{4.44}$$

where the boundaries of the integral can be defined later. We use the index $(1A)$ to distinguish this measurement from other possible measurements of the first-order correlation function.

As in Eq. (4.43) the integrand of this expression is

$$\begin{aligned}\Gamma^{(1A)}(t,t+\tau) &= \left\langle S_b^\dagger(t) S_b(t+\tau)\right\rangle \\ &= g_b^2(\kappa_b \left\langle a^\dagger(t)a(t+\tau)\right\rangle + \left\langle n_b(t)n_b^\dagger(t+\tau)\right\rangle) \\ &= g_b^2(\kappa_b G^{(1)}(t,t+\tau) + H_b(t,t+\tau)).\end{aligned} \tag{4.45}$$

The cross terms between a and n_b vanished due to the assumptions on the noise modes. Therefore we understand that this measurement gives the sum of the first-order correlation functions of the cavity field and the noise

$$\Gamma^{(1A)}(\tau) = g_b^2(\kappa_b G^{(1)}(\tau) + H_b(\tau)). \tag{4.46}$$

To get rid of the noise correlations a reference measurement can be subtracted. When the resonator is left in the steady state close to the ground state we have $G_{ss}^{(1)} \approx 0$ and $\Gamma_{\mathrm{ss}}^{(1A)} \approx H_b$. In other words,

$$\frac{\Gamma^{(1A)}(\tau) - \Gamma_{\mathrm{ss}}^{(1A)}(\tau)}{g_b^2\kappa_b} = G^{(1)}(\tau). \tag{4.47}$$

Two Channel

Using both channels we can define a similar measurement by calculating the cross-correlation of the measurement data.

$$\Gamma^{(1)}(\tau) = \int \left\langle S_b^\dagger(t) S_c(t+\tau)\right\rangle dt. \tag{4.48}$$

We find then

$$\Gamma^{(1)}(\tau) = g_b g_c(\sqrt{\kappa_b\kappa_c} G^{(1)}(\tau) + G_{bc}(\tau)). \tag{4.49}$$

where again all cross terms vanish. If we assume that the noise on b and c is uncorrelated so that $G_{bc} = 0$, this is already the first-order correlation function

$$\Gamma^{(1)}(\tau)/\left(g_b g_c\sqrt{\kappa_b\kappa_c}\right) = G^{(1)}(\tau). \tag{4.50}$$

For $N_{bc} \neq 0$ subtracting the correlation of the noise by a reference measurement is also possible, so that

$$\frac{\Gamma^{(1)}(\tau) - \Gamma_{\mathrm{ss}}^{(1)}(\tau)}{g_b g_c\sqrt{\kappa_b\kappa_c}} = G^{(1)}(\tau). \tag{4.51}$$

4.3.3. Second-order correlation function

Similar to the construction of first-order correlation measurements we also derive how the second-order correlation function can be measured using the record of $S_b(t), S_c(t)$. From the variety of four point correlations of this data we present two which allow to extract the second-order correlation function.

Cross-power auto-correlation

First we analyze a measurement of the auto-correlation of the cross-power $S_b^\dagger S_c$

$$\Gamma^{(2Y)}(t, t+\tau) = \left\langle S_b^\dagger(t) S_c(t) S_b^\dagger(t+\tau) S_c(t+\tau) \right\rangle . \tag{4.52}$$

Again an index $(2Y)$ is introduced to distinguish this measurement from other second-order measurements. By using Eq. (4.32) this expression can be written as a fourth-order polynomial in the system operators $a, b_{\text{in}}, c_{\text{in}}, n_c, n_b$. For simplicity of the calculation we assume that correlated noise is sufficiently small and take $N_{bc} = 0$. The correctness of this assumption depends strongly on the experimental context and has to be verified. In this case we can apply simplifications presented in Eqs. (C.2) – (C.4) and find directly the second-order correlation function of the resonator field

$$\Gamma^{(2Y)}(t, t+\tau) = g_b^2 g_c^2 \kappa_b \kappa_c \left\langle a^\dagger(t) a^\dagger(t+\tau) a(t) a(t+\tau) \right\rangle . \tag{4.53}$$

From the integrated form

$$\Gamma^{(2Y)}(\tau) = \int \Gamma^{(2Y)}(t, t+\tau) dt \tag{4.54}$$

we conclude

$$\Gamma^{(2Y)}(\tau)/(g_b^2 g_c^2 \kappa_b \kappa_c) = G^{(2)}(\tau). \tag{4.55}$$

Note in particular that no noise subtraction is necessary.

Power cross-correlation

A different possibility to construct a measurement of the second-order correlation function is the cross-correlation of the powers on each channel

$$\Gamma^{(2A)}(t, t+\tau) = \left\langle S_b^\dagger(t) S_b(t) S_c^\dagger(t+\tau) S_c(t+\tau) \right\rangle . \tag{4.56}$$

By inserting Eq. (4.29) we find again a fourth-order polynomial in the system operators. The order of the S operators was chosen such, that all the operators $b_{\text{in}}^\dagger, c_{\text{in}}$ are normally ordered and vanish by the argument in App. C.4. Then we can write

$$\begin{aligned} &\Gamma^{(2A)}(t, t+\tau) = \\ &\quad g_b^2 g_c^2 \langle (\sqrt{\kappa_b} a^\dagger(t) + n_b(t))(\sqrt{\kappa_c} a^\dagger(t+\tau) + n_c(t+\tau)) \\ &\quad\quad (\sqrt{\kappa_b} a(t) + n_b^\dagger(t))(\sqrt{\kappa_c} a(t+\tau) + n_c^\dagger(t+\tau)) \rangle . \end{aligned} \tag{4.57}$$

Expanding this multiplication and using the same assumptions on the noise as before we get

$$\begin{aligned}\Gamma^{(2A)}(t, t+\tau) = \\ & g_b^2 g_c^2 (\kappa_b \kappa_c \langle a^\dagger(t) a^\dagger(t+\tau) a(t) a(t+\tau)\rangle \\ & \quad + \kappa_c G^{(1)}(t+\tau, t+\tau) H_b(t,t) \\ & \quad + \kappa_b G^{(1)}(t,t) H_c(t+\tau, t+\tau) \\ & \quad + H_b(t,t) H_c(t+\tau, t+\tau)).\end{aligned} \tag{4.58}$$

Integrating over time gives

$$\Gamma^{(2A)}(\tau) = \int dt \Gamma^{(2A)}(t, t+\tau) = g_b^2 g_c^2 \kappa_b \kappa_c G^{(2)}(\tau) + C, \tag{4.59}$$

where the constant offset C is defined as

$$\begin{aligned}C = g_b^2 g_c^2 \int dt (\kappa_c G^{(1)}(t+\tau, t+\tau) H_b(t,t) \\ + \kappa_b G^{(1)}(t,t) H_c(t+\tau, t+\tau) \\ + H_b(t,t) H_c(t+\tau, t+\tau)).\end{aligned} \tag{4.60}$$

We find this integral constant with respect to τ so that it is only a function in the resonator photon number and the noise levels on the output channels. The simplified expression is given by

$$C = g_b^2 g_c^2 \left(\kappa_c G^{(1)}(0) H_b(0) + \kappa_b G^{(1)}(0) H_c(0) + H_b(0) H_c(0) \right). \tag{4.61}$$

Although it might not always be necessary to compensate for this constant offset we will show how C can be measured. The last term on the r.h.s. can be measured by turning off the state preparation because it contains only noise operators

$$g_b^2 g_c^2 H_b(0) H_c(0) = \Gamma_{\text{ss}}^{(2A)}(0). \tag{4.62}$$

From the results of the first-order correlation measurement on one channel Eq. (4.45) we find

$$g_b^2 H_b(0) = \Gamma_{b,ss}^{(1A)}(0) \quad \text{and} \quad g_c^2 H_c(0) = \Gamma_{c,ss}^{(1A)}(0) \tag{4.63}$$

and

$$g_b^2 \kappa_b G^{(1)}(0) = \Gamma_b^{(1A)}(0) - \Gamma_{b,ss}^{(1A)}(0) \quad \text{and} \quad g_c^2 \kappa_c G^{(1)}(0) = \Gamma_c^{(1A)}(0) - \Gamma_{c,ss}^{(1A)}(0) \tag{4.64}$$

The offset C can now be written in terms of measurements

$$\begin{aligned}C = \Gamma_{\text{ss}}^{(2A)}(0) + (\Gamma_c^{(1A)}(0) - \Gamma_{c,\text{ss}}^{(1A)}(0)) \Gamma_{b,\text{ss}}^{(1A)}(0) \\ + (\Gamma_b^{(1A)}(0) - \Gamma_{b,\text{ss}}^{(1A)}(0)) \Gamma_{c,\text{ss}}^{(1A)}(0).\end{aligned} \tag{4.65}$$

This estimation of the offset C can be understood as a comprehensive characterization of the detection system. By switching on and off the source under consideration, one can characterize only the detector or a combination of the source and the detector. By performing all measurements indicated above it is then possible to separate the influences of the source and the detectors.

4.3.4. Other correlations

Apart from first and second-order correlation functions it is also possible to measure any other correlation function in terms of the field operator a as it is indicated in the App. C. Although in the context of quantum optics alternative correlation measures are rarely used, proposition and experiments exist allowing for relevant insights to the character of non-classical light sources. In particular for a *third-order* type correlation[3] violations of classical bounds by up to two orders of magnitude were predicted [39, 40] and measured [41]. Although no measurements of other correlations are presented here we want to point out that they are readily accessible and suggest the experimental implementation and interpretation of these correlation functions for future work.

4.4. Single photon source

To measure the different quantities derived in the last section we implemented a single photon source which we describe theoretically here. The idea in the implementation was to use the qubit as a tool to prepare non-classical states in the resonator similar to Refs. [6, 7, 8]. With our preparation scheme it is possible to generate deterministically any resonator state out of a family of *single photon states*

$$|\psi\rangle = \alpha|0\rangle + \beta|1\rangle. \tag{4.66}$$

4.4.1. State preparation

To prepare these states a two-step procedure is applied. First the qubit is excited from the ground state to a superposition state by controlled Rabi rotations by an angle θ_r

$$|g\rangle \xrightarrow{\text{Rabi pulse}} \alpha|g\rangle + \beta|e\rangle, \tag{4.67}$$

where $\alpha = \cos(\theta_r/2)$ and $\beta = \sin(\theta_r/2)$. In the second step the qubit interacts resonantly with the resonator such that they coherently exchange excitations, known as vacuum Rabi oscillations. If the interaction time is set to half a vacuum Rabi period we achieve the following mapping [42]:

$$|g0\rangle \to |g0\rangle, \qquad |e0\rangle \to i|g1\rangle, \tag{4.68}$$

$$|g1\rangle \to i|e0\rangle, \qquad |e1\rangle \to \cos\sqrt{2}\pi|e1\rangle + i\sin\sqrt{2}\pi|g2\rangle. \tag{4.69}$$

---

[3] which actually should be called 1.5-order correlation

From the first line we can see that this operation maps the qubit state to the resonator state when the resonator was in its ground state $|0\rangle$. After the operation the qubit is then left in $|g\rangle$. If there was a photon in the resonator at the beginning of the operation the situation is different and the system will end up in an entangled state. This is because with N excitations in the system the vacuum Rabi frequency increases as $\sqrt{N}$. For now we want to assume, that the resonator starts out in the ground state and our system is described by $|g\rangle \otimes |0\rangle$ and we get after the first step

$$|\psi_1\rangle = (\alpha|g\rangle + \beta|e\rangle) \otimes |0\rangle. \tag{4.70}$$

The second step maps the qubit state to the resonator state successfully, because there is no two-excitation component in the system:

$$|\psi_2\rangle = |g\rangle \otimes (\alpha|0\rangle + i\beta|1\rangle) \tag{4.71}$$

Tracing out the qubit, the final resonator state is

$$|\psi_{\mathrm{f0}}\rangle = \alpha|0\rangle + i\beta|1\rangle. \tag{4.72}$$

In the experiment the assumption that the resonator is in the ground state at the beginning of the state preparation is only approximately correct. Due to coupling to the input lines and ambient temperature, the resonator is always found in a thermal state with a small thermal photon number n_{th}. This thermal field limits the fidelity of our state preparation as we discuss here.

As a first order approximation, we take the steady state of the resonator to be

$$\rho_{\mathrm{ss}} = (1 - n_{\mathrm{th}})|0\rangle\langle 0| + n_{\mathrm{th}}|1\rangle\langle 1| \tag{4.73}$$

where we dropped all the higher-order terms because $n_{\mathrm{th}} \ll 1$. We now calculate the result of the state preparation when there is a photon in the cavity. Starting with a system state $|g\rangle \otimes |1\rangle$ we find the final joint state of the qubit and resonator to be

$$|\psi_{\mathrm{f1}}\rangle = i\alpha|e0\rangle + \beta\Gamma_{\mathrm{c}}|e1\rangle + \beta\Gamma_{\mathrm{s}}|g2\rangle \tag{4.74}$$

with the constants $\Gamma_{\mathrm{s}} = i\sin\sqrt{2}\pi$ and $\Gamma_{\mathrm{c}} = \cos\sqrt{2}\pi$. Combining this result with Eq. (4.72) by using the linearity of quantum mechanics we can write the final resonator state ρ_f when starting out from ρ_{ss} as

$$\begin{aligned}
\rho_{\mathrm{f}} &= \mathrm{tr}_{\mathrm{qubit}}\{(1 - n_{\mathrm{th}})|\psi_{f0}\rangle\langle\psi_{f0}| + n_{\mathrm{th}}|\psi_{f1}\rangle\langle\psi_{f1}|\} \\
&= |\alpha|^2\,|0\rangle\langle 0| + \Big(1 + n_{\mathrm{th}}(|\Gamma_{\mathrm{c}}|^2 - 1)\Big)\,|\beta|^2\,|1\rangle\langle 1| + n_{\mathrm{th}}\,|\beta|^2\,|\Gamma_{\mathrm{s}}|^2\,|2\rangle\langle 2| \\
&+ (1 - n_{\mathrm{th}}(1 + \Gamma_{\mathrm{c}}))(i\beta\alpha^*|1\rangle\langle 0| - i\alpha\beta^*|0\rangle\langle 1|).
\end{aligned} \tag{4.75}$$

For $n_{\mathrm{th}} = 0$ this state corresponds to the ideal state $|\psi_{\mathrm{f0}}\rangle$ where the qubit state is mapped to a photon state. For finite thermal temperatures different effects result in a deviation of the final state from the ideal state. First one can observe that the final resonator state is a mixed state between a zero and one photon superposition state and a two photon Fock state. The two photon component is directly proportional to the thermal photon number and can be interpreted as the cases where the state preparation effectively fails. At the same time the off-diagonal elements which are a part of the zero and one photon superposition state decrease for higher temperatures.

4.4.2. Observables

Based on the state ρ_f prepared in our single photon source we can calculate the expectation values of different observables. Generally the expectation value of a measurement with an operator A is given by $\langle A\rangle = \mathrm{tr}\left\{A\rho_\mathrm{f}\right\}$. In the measurements which are used for correction the resonator is left in its steady-state and the expectation value of the same observable is given by $\langle A\rangle_\mathrm{ss} = \mathrm{tr}\left\{A\rho_\mathrm{ss}\right\}$.

When measuring the average field quadratures we effectively measure the expectation value of the annihilation operator as shown in Eq. (4.41). This is found to be

$$\langle a(0)\rangle = i\beta\alpha^*(1 - n_\mathrm{th}(1-\Gamma_\mathrm{c})) = \left\langle a^\dagger(0)\right\rangle^* \tag{4.76}$$

and the steady state

$$\left\langle a^\dagger(0)\right\rangle_\mathrm{ss} \;=\; \langle a(0)\rangle_\mathrm{ss} = 0. \tag{4.77}$$

The real part of $\langle a(0)\rangle$ is plotted in Fig. (4.4a) against the Rabi angle of the preparation for different thermal background fields. The imaginary part not plotted, since it can be chosen to be zero, by adjusting the phase of the reference frame. The value of this observable is related to the phase of the superposition in the prepared state and decreases for stronger background fields. This can be interpreted as a decoherence effect by the thermal field which randomizes the phase of the prepared state.

For the second-order moments which appear in power and correlation measurements we find

$$\begin{aligned}\langle n(0)\rangle &= |\beta|^2\left(1 + n_\mathrm{th}\left|\Gamma_\mathrm{s}\right|^2\right) && (4.78)\\ \langle n(0)\rangle_\mathrm{ss} &= n_\mathrm{th} && (4.79)\end{aligned}$$

and

$$\left\langle a(0)^2\right\rangle = \left\langle a^\dagger(0)^2\right\rangle = \left\langle a(0)^2\right\rangle_\mathrm{ss} = \left\langle a^\dagger(0)^2\right\rangle_\mathrm{ss} = 0. \tag{4.80}$$

The relevant observable from the second-order moments is the average photon number $\langle n(0)\rangle$ which is plotted against the Rabi angle for different thermal background fields in Fig. (4.4b). The maximum value is achieved for the Fock state $|1\rangle$ ($\theta_r = \pi$) because we only prepare states with one excitation. For stronger thermal background fields the average photon number increases in the preparation scheme for the $|1\rangle$ state. This is due to the increasing probability

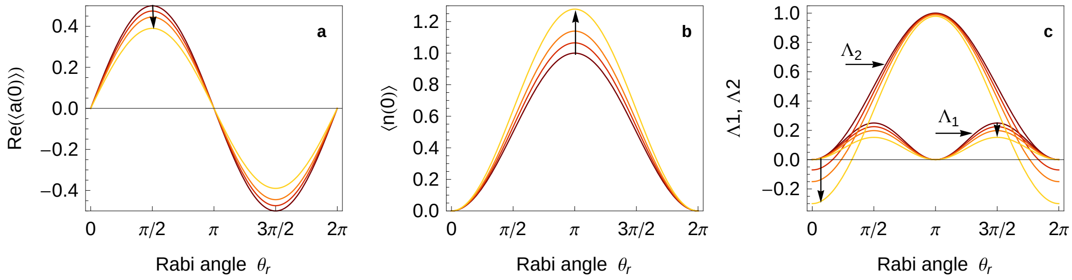

Figure 4.4.: Different observables of the single photon source at time $t = 0$ when the state preparation is finished. All observables are plotted against the Rabi angle θ_r which is used in the state preparation for different thermal steady-state fields of the resonator $n_{\text{th}} = \{0, 0.07, 0.15, 0.3\}$.

of preparing a $|2\rangle$ state indicated in Eq. (4.75).

For the fourth-order moment appearing in the second-order correlation function we find

$$\begin{aligned} \left\langle a^\dagger a^\dagger a a(0) \right\rangle &= 2n_{\text{th}} \left|\beta\right|^2 \left|\Gamma_{\text{s}}\right|^2 && (4.81)\\ \left\langle a^\dagger a^\dagger a a(0) \right\rangle_{\text{ss}} &= 0. && (4.82) \end{aligned}$$

For the measurement of the first-order correlation function we also introduce the quantities

$$\begin{aligned} \Lambda_1 &= \langle a(0)\rangle \left\langle a^\dagger(0)\right\rangle - \left\langle a^\dagger(0)\right\rangle_{\text{ss}} \langle a(0)\rangle_{\text{ss}} \\ &= \left|\alpha\beta\right|^2 \left(1 - n_{\text{th}}(1 + \Gamma_{\text{c}})\right)^2 && (4.83)\\ \Lambda_2 &= \langle n(0)\rangle - \langle n(0)\rangle_{\text{ss}} \\ &= \left|\beta\right|^2 \left(1 + n_{\text{th}} \left|\Gamma_{\text{s}}\right|^2\right)) - n_{\text{th}} && (4.84) \end{aligned}$$

which are plotted in Fig. (4.4c). These two values which relate to the peak heights in the first-order correlation function are essentially given by the expectation values of the annihilation operator and the photon number and therefore share the behavior discussed before.

4.4.3. Time dependence of observables

Based on the observables for $t = 0$ we can now calculate the time evolution of these quantities. The dynamics of the cavity is given by the equation of motion [35] for a which is

$$\dot{a} = -i\omega_r a - \frac{\kappa_c + \kappa_b}{2} a + \sqrt{\kappa_c} c_{\text{in}} + \sqrt{\kappa_b} b_{\text{in}}. \qquad (4.85)$$

Although the qubit could be included in this equation we neglect it here for reasons of simplicity. Note that this is an equation for the operator a, not its expectation value. Solving this equation in a rotating frame we can derive the expectation value of the field operator a resulting in

$$\langle a(t)\rangle = \langle a(0)\rangle e^{-\kappa t/2}, \qquad t > 0. \qquad (4.86)$$

At $t = 0$ the cavity state is prepared by a pulse with dynamics which are taken to be infinitely fast (certainly much faster than any other time scales in the problem). Moreover, the state preparation is repeated every $t_\mathrm{p} \gg 1/\kappa$, so that to a good approximation the cavity state has decayed to the steady state by the end of a repetition period. The fact that many photons are prepared one after another is taken into account by writing $\langle a(t)\rangle$ as a train of pulses

$$\langle a(t)\rangle = \langle a(0)\rangle \sum_k \Pi(t - kt_\mathrm{p}, \kappa/2) \tag{4.87}$$

where we introduced a function for the peak of the exponential decay of each photon as

$$\Pi(t,\kappa) = \Theta(t)\Theta(t_\mathrm{p} - t)e^{-\kappa t}, \tag{4.88}$$

with $\Theta(t)$ is the Heaviside step function. The final form of the peak is effectively determined by the low pass filtering in the detection chain which is discussed in Sec. C.3. In Fig. (4.5a) this filtered exponential decay is plotted for typical experimental parameters and differend filter bandwidths. For very narrow band filtering one can see that the peak is strongly distorted and cannot be neglected.

The higher-order multi-time correlations of the field operators can be calculated using the quantum regression theorem as shown in App. C.2. Here we consider two cases. When t and $t+\tau$ are in the same repetition period we assume that the operator values at these times are correlated whereas for larger time differences they are taken to be independent.

t and $t+\tau$ in the same period

When t and $t+\tau$ are both in the kth period we find the second-order moment of the field operators which corresponds to the first-order correlation function using [43] as

$$\langle a^\dagger(t)a(t+\tau)\rangle = \langle n(0)\rangle e^{-\kappa(t-kt_\mathrm{p}+\tau/2)}, \tag{4.89}$$

where k denotes the largest integer such that $t - kt_\mathrm{p} \geq 0$, and $\langle n(0)\rangle$ is the average number of photons at the times of state preparation ($t = kt_\mathrm{p}$).

From all the higher moments we only evaluate the one corresponding to the second-order correlation function

$$\langle a^\dagger(t)a^\dagger(t+\tau)a(t+\tau)a(t)\rangle = \langle a^\dagger a^\dagger aa(0)\rangle e^{-\kappa(2t-2kt_\mathrm{p}+\tau)} \tag{4.90}$$

as it is done in Eq. (C.13).

t and $t+\tau$ in the different periods

When t is in the kth period and $t+\tau$ in the $k+l$th period the two different measurements can be taken to be independent and thus factorize. For two measurement operators $f(t)$ and

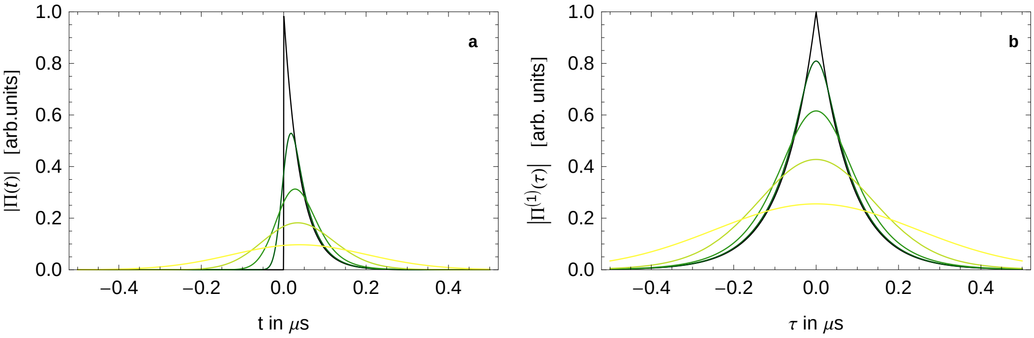

Figure 4.5.: Theoretical peak functions Π in **a**) and $\Pi^{(1)}$ in **b**) for $\kappa/2\pi = 4\,\mathrm{MHz}$ and different low pass filters. Black: no filtering, then 10MHz, 4MHz, 2MHz, Yellow: 1MHz

$g(t+\tau)$ this means

$$\langle f(t)g(t+\tau)\rangle = \langle f(t)\rangle \langle g(t+\tau)\rangle\,. \tag{4.91}$$

The expectation values of above then become

$$\langle a^\dagger(t)a(t+\tau)\rangle = |\langle a(0)\rangle|^2 e^{-\kappa[t-kt_\mathrm{p}+(\tau-lt_\mathrm{p})/2]}, \tag{4.92}$$

where $l \neq 0$ is the number of periods separating t and $t+\tau$. From the higher moments we only evaluate

$$\langle a^\dagger(t)a^\dagger(t+\tau)a(t+\tau)a(t)\rangle = \langle n(0)\rangle^2 e^{-\kappa(2t-2kt_\mathrm{p}+\tau-lt_\mathrm{p})}. \tag{4.93}$$

We can re-write the above expressions by summing up the two distinct cases over all repetitions of the photon preparation. Additionaly we replace the exponential terms by the peak function $\Pi(t,\kappa)$ and find

$$\begin{aligned}\langle a^\dagger(t)a(t+\tau)\rangle = \sum_k \Pi(t-kt_\mathrm{p},\kappa/2)\times \\ \Bigg[\Pi(t+\tau-kt_\mathrm{p},\kappa/2)\langle n(0)\rangle + \\ \sum_{l\neq 0}\Pi(t+\tau-(k+l)t_\mathrm{p},\kappa/2)|\langle a(0)\rangle|^2\Bigg]\,.\end{aligned} \tag{4.94}$$

For the higher order correlations we can similarly write

$$\langle a^\dagger(t)a^\dagger(t+\tau)a(t+\tau)a(t)\rangle = \sum_k \Pi(t-kt_\mathrm{p},\kappa)\times \Bigg[\Pi(t+\tau-kt_\mathrm{p},\kappa)\langle a^\dagger a^\dagger aa(0)\rangle + \sum_{l\neq 0}\Pi(t+\tau-(k+l)t_\mathrm{p},\kappa)\langle n(0)\rangle^2\Bigg]. \quad (4.95)$$

4.4.4. First-order correlation function

From the relevant moments of the field operator a for the single photon source, we now derive an analytical expression for the first-order correlation function in its time integrated form. Based on Eq. (4.94) we want to integrate

$$G^{(1)}(\tau) = \int_0^{t_c} \left\langle a^\dagger(t)a(t+\tau)\right\rangle dt \quad (4.96)$$

where we assume that the integration limit is given by an integer number of repetitions $t_c = Nt_\mathrm{p}$ and as before $t_\mathrm{p} \gg 1/\kappa$. By swapping the sum in Eq. (4.94) with the integration in Eq. (4.96) the relevant integration remaining is

$$\Pi^{(1)}(\tau) = \int_0^{t_c} dt\ \Pi(t,\kappa/2)\Pi(t+\tau,\kappa/2) \approx \frac{e^{-\kappa|\tau|/2}}{\kappa}. \quad (4.97)$$

This function gives us the peak shape which defines the first-order correlation function depicted in Fig. (4.5b) for different low pass filters. Again the filtering blurs out the acute peak in the correlation function and by that sets a lower limit for the detection bandwidth. From the discussion in Sec. C.3 one can see that effect can be fully incorporated into the $\Pi^{(1)}$ function and therefore we can write the first-order correlation function in a closed form

$$G^{(1)}(\tau) = N\langle n(0)\rangle\Pi^{(1)}(\tau) + N|\langle a(0)\rangle|^2\sum_{l\neq 0}\Pi^{(1)}(\tau - lt_\mathrm{p}). \quad (4.98)$$

Later it will be shown that experimentally it is easier to access the difference between $G^{(1)}$ with cavity state preparation and $G^{(1)}$ without cavity state preparation (*i.e.* using only the steady state of the cavity). For a thermal steady state we find

$$G^{(1)}{}_\mathrm{ss}(\tau) = N\langle n(0)\rangle\Pi^{(1)}_\mathrm{ss}(\tau), \quad (4.99)$$

where the steady state can have a different dynamic behavior described by $\Pi^{(1)}_\mathrm{ss}(\tau)$. The

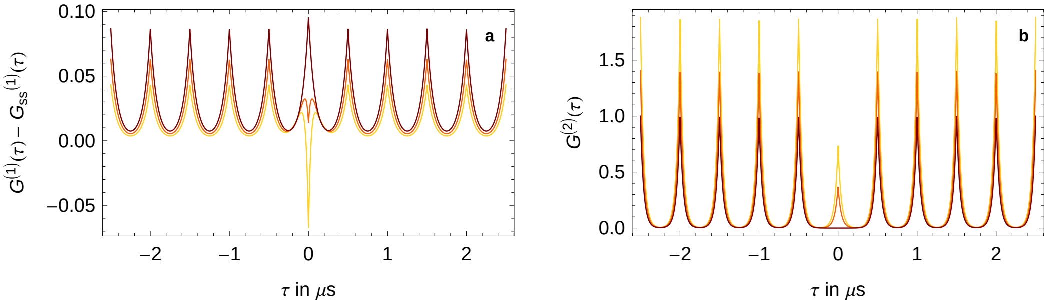

Figure 4.6.: **a**) Theoretical $G^{(1)}(\tau)$ of the single photon source with subtracted steady state measurement for $\theta_r = 0.2\pi, \kappa/2\pi = 4\text{MHz}, t_\text{p} = 0.5\mu s$ and a thermal background field in the resonator for $n_\text{th} = 0$ (brown), $n_\text{th} = 0.2$ (orange), $n_\text{th} = 0.4$ (yellow). **b**) Theoretical $G^{(2)}(\tau)$ of the single photon source for the same thermal background fields as in **a**.

difference between measurements becomes then

$$(G^{(1)}(\tau) - {G^{(1)}}_\text{ss}(\tau))/N = \langle n(0)\rangle \Pi^{(1)}(\tau) - \langle n(0)\rangle_\text{ss} \Pi^{(1)}_\text{ss}(\tau) + |\langle a(0)\rangle|^2 \sum_{l\neq 0} \Pi^{(1)}(\tau - l t_\text{p}). \tag{4.100}$$

An example of this function is given in Fig. (4.6a) for $\theta_r = 0.2\pi$ and three different thermal background fields. In this plot we chose a repetition time of $t_\text{p} = 0.5\mu s$ and neglected the influence of low pass filtering. The first effect which can be observed is that the center peak decreases for stronger background fields and even becomes negative for small θ_r. The height of this peak is essentially given by the photon number difference between the state preparation and the steady state. In the case where the center peak becomes negative the state preparation can be interpreted as cooling of the resonator field which is discussed in Sec. 5.4. Furthermore, the height of the outer peaks reduces for stronger background fields as a result of the decoherence in the state preparation as discussed in Sec. 4.4.2.

A second example for the measured $G^{(1)} - {G^{(1)}}_\text{ss}$ function of the single photon source is given in Fig. (4.7) for different state preparation angles θ_r and a fixed finite background field. For the preparation with $\theta_r = 0$ (top left) a negative peak is expected which corresponds to the cooling of the resonator field through the state preparation. For larger preparation angles $0 < \theta_r \leq \pi/2$ the center and the outer peaks grow because states with more energy are prepared. For $\pi/2 < \theta_r$ the center peak continues to grow since it is proportional to the average photon number whereas the outer peaks decrease again. Over the whole range of θ_r the center peak(outer peaks) follows closely the dependence which was derived for $\Lambda_2(\Lambda_1)$ in Eq. (4.83) and are plotted in Fig. (4.4c).

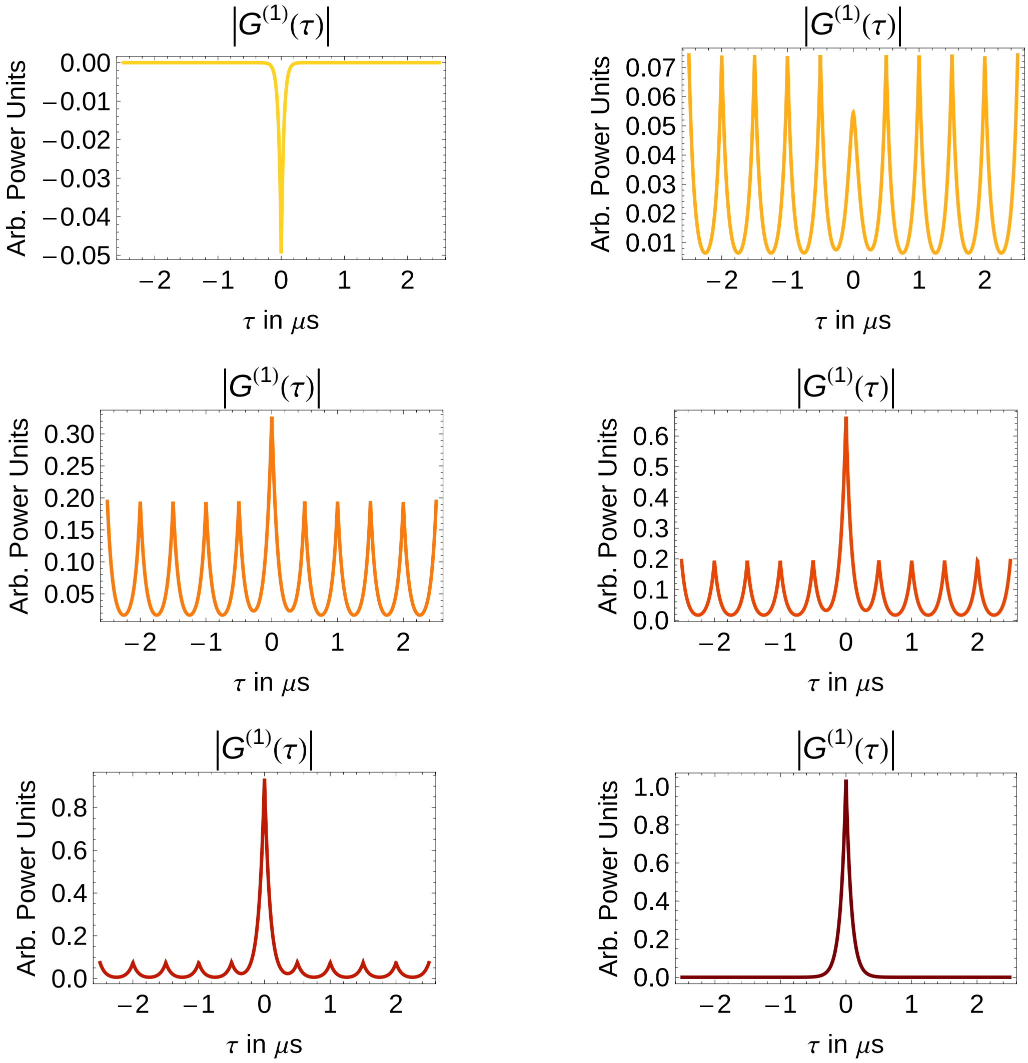

Figure 4.7.: Theoretical $G^{(1)}$of the single photon source for different Rabi angles. Top left $\theta_r = 0$ to bottom right $\theta_r = \pi$. Other parameters are $\kappa/2\pi = 4\,\text{MHz}$, $t_\text{p} = 0.5\,\mu s$, $n_\text{th} = 0.05$.

4.4.5. Second-order correlation function

In the same way as before we also derive an analytical expression for the second-order correlation function of the single photon source. Using the result of Eq. (4.95) we integrate

$$G^{(2)}(\tau) = \int_0^{t_c} \langle a^\dagger(t+\tau) a^\dagger(t) a(t+\tau) a(t) \rangle dt. \tag{4.101}$$

The relevant integration is found to be

$$\Pi^{(2)}(\tau) = \int_0^{t_c} \Pi(t,\kappa)\Pi(t+\tau,\kappa)\ dt \approx \frac{e^{-\kappa|\tau|}}{\kappa}. \tag{4.102}$$

Finally we rewrite the sum from Eq. (4.95) as

$$G^{(2)}(\tau) = N\langle a^\dagger a^\dagger aa(0)\rangle \Pi^{(2)}(\tau) + N\langle n(0)\rangle^2 \sum_{l\neq 0} \Pi^{(2)}(\tau - l t_{\mathrm{p}}). \tag{4.103}$$

In Fig. (4.6b) we see an exemplary plot of $G^{(2)}$ for which a $|1\rangle$ state was prepared in the resonator. If the cavity is initially in its ground state, we find that the middle peak is absent, whereas for weak thermal fields a small peak exists. However any case where the middle peak is smaller than the outer peaks can be interpreted as antibunching of the emitted radiation and is a signature of the quantum nature of the prepared light.

5. Experiments

This last chapter contains the experimental results which could be obtained during this thesis. First we present the measurements and methods to characterize the microwave cavity and the transmon qubit. Based on these measurements we were able to perform experiments in which the qubit state and the interaction between qubit and cavity are controlled and detected. These experiments serve as a calibration to implement the single photon source which is discussed theoretically in Sec. 4.4. In the last set of experiments the single photon source is characterized and we present measurements of the first and second-order correlation function of the emitted radiation.

5.1. Sample characterization

The first step in the characterization of our sample is a transmission measurement of the resonator. For this purpose we apply a continuous coherent tone to the input of the resonator and measure the average quadratures of the transmitted signal $T = \left|\int \langle S_b(t)\rangle \, dt\right|$. By sweeping the frequency in a small range around the resonance frequency of our cavity we observe a characteristic Lorentzian line shape as in Fig. (5.1a) which allows us to extract the relevant parameters of the resonator as $\nu_r = 6.433\,\mathrm{GHz}$ and $\kappa = 3.12\,\mathrm{MHz}$ (equivalently $Q = 2060$).

Performing this measurement for different static magnetic fields on our sample we can observe how the qubit which has a flux tunable transition frequency influences the resonator. As a signature of the strong coupling between qubit and resonator we can observe the vacuum Rabi mode splitting at the point where qubit frequency and the resonator frequency coincide. The splitting is visible as two peaks in the transmission spectrum in Fig. (5.1b) which are separated by twice the coupling constant. This allows to extract the qubit-resonator coupling constant $g = 54\,\mathrm{MHz}$ for our sample.

In a second step we characterize the qubit by spectroscopic measurements. For a certain magnetic field we first measure the resonator transmission spectrum and find the frequency of the maximum transmission. Then we keep the measurement tone constant at this frequency and apply a *spectroscopy tone* of variable frequency to excite transitions in the qubit. If the frequency matches a qubit transition and the qubit is excited the effective resonator frequency is changed by the dispersive shift χ described in Sec. 2.1. This becomes visible as a reduced transmission of the measurement tone and allows us to detect the qubit transition frequencies as shown in Fig. (5.2a). The $|g\rangle \rightarrow |e\rangle$ transition is easily identified as the transition with the

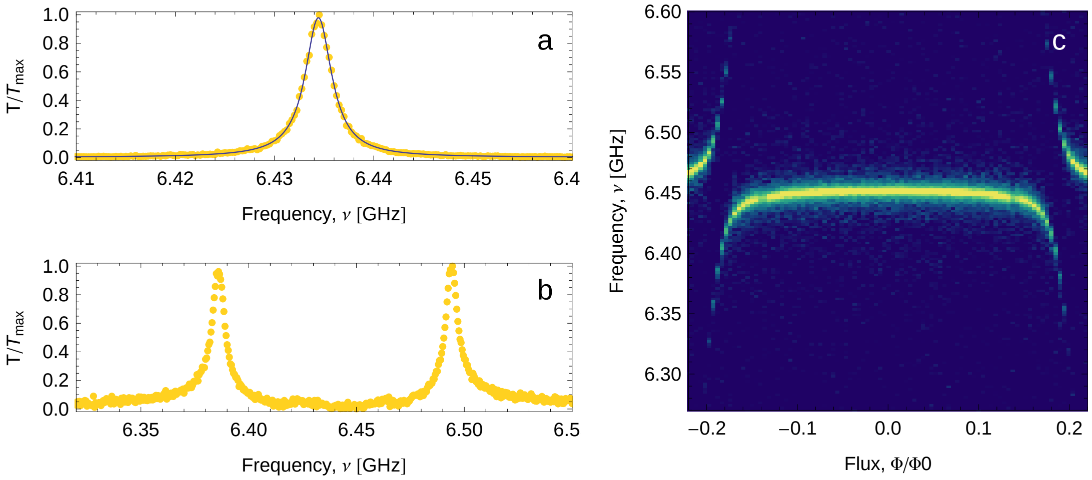

Figure 5.1.: **a**) Measurement of the transmission through the resonator at the working point for the qubit state preparation used in the single photon source experiments. The qubit is strongly detuned in this case and the relevant resonator parameters ν_r and κ can be extracted from this measurement (dots: measurement, lines: fit). **b**) Transmission spectrum of the resonator in the vacuum Rabi mode splitting. The splitting is visible as two peaks in the measurement, which are separated by twice the coupling constant g. **c**) Transmission spectra of the resonator for different static magnetic fields. The vacuum Rabi mode splitting is visible as avoided crossings on the left and right.

strongest response, because the qubit is mostly in the ground state and all other transitions in this frequency range are due to less probable multi-photon processes. The second peak in Fig. (5.2a) is due to the ac-Stark shift [44, 45] of the qubit frequency by the finite photon number of the measurement tone in the cavity. By increasing the power of the measurement tone more peaks can be observed which correspond each to $0, 1, \ldots$ photons in the cavity and have the characteristic Poissonian distribution of the photon number of a coherent field (Fig. (5.2b)). The spacing of these peaks is twice the dispersive shift χ and can be used to extract χ.

Finally we perform this spectroscopy measurement for different static magnetic fields and get a full characterization of the qubits transition frequencies and their flux dependence as in Fig. (5.2c). In this measurement we can observe three lines which correspond to the transitions $|g0\rangle \rightarrow |e0\rangle$, $|g1\rangle \rightarrow |e1\rangle$ and $|g1\rangle \rightarrow |f0\rangle$. Based on this measurement we choose a working point by adjusting the magnetic field such that the qubit $|g0\rangle \rightarrow |e0\rangle$ transition has a certain transition frequency. For the experiments implementing a single photon source we chose $\nu_a = 6.933\,\text{GHz}$ so that the qubit is detuned around 500 MHz above the resonator frequency. At this point we find the following parameters for the cavity and the qubit:

- $\nu_r = 6.433\,\text{GHz}$, $\kappa = 3.12\,\text{MHz}$
- $\nu_a = 6.933\,\text{GHz}$, $\chi = 22.3\,\text{MHz}$

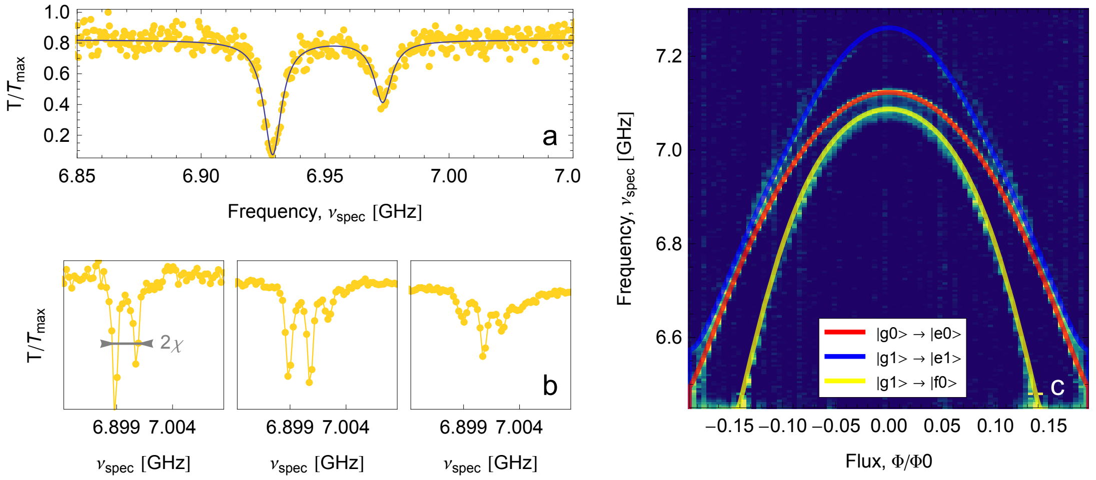

Figure 5.2.: **a**) Spectroscopic measurement of the qubit at the working point for the qubit state preparation used in the single photon source experiments. The $|g\rangle \rightarrow |e\rangle$ transition is visible as the large dip in the measurement. (dots: measurement, lines: fit). **b**) Similar spectroscopic measurement as in a) for three different powers of the measurement tone. For higher powers (right) additional peaks become visible due to the broader photon number distribution of the coherent measurement tone. **c**) Spectrum of the qubit for different magnetic fields. Colored lines are theoretical predictions for three different transitions.

5.2. Coherent control and qubit read-out

In a second set of experiments we choose the working point described above and perform controlled preparation and read-out of the qubit state. The excitation of the qubit from the ground state to the excited state is achieved by a coherent microwave pulse at the qubit frequency. For the pulse preparation we use single sideband modulation as described in Sec. 3.3. The pulses have a gaussian envelope with a pulse length of 18 ns[1] and variable amplitude A_r as depicted in Fig. (5.3a).

After the qubit excitation we extract the qubit state by the dispersive read-out scheme [18] described in Sec. 2.2. This is done by switching on a coherent measurement tone and measuring the time-resolved response of the cavity. By fitting this response to the theoretical responses given by the solutions of the cavity Bloch equations we can then extract the population $P_e = |\langle\psi_q|e\rangle|^2$ of the qubit state $|\psi_q\rangle$. An exemplary measurement of the qubit in the ground(excited) state with the respective fits are given in Fig. (5.3c(d)).

In Fig. (5.3b) we see the extracted qubit population of this preparation and read-out experiment where the pulse amplitudes A_r were chosen between 0 % and 100 % of some maximal amplitude. We can clearly observe *Rabi oscillations* in the qubit population (dots) which are in excellent agreement with the theoretical prediction (red line). The qubit states which are

---

[1] The gaussian shape has a standard deviation of $\sigma = 3\,\text{ns}$ and is cropped after $\pm 3\sigma$.

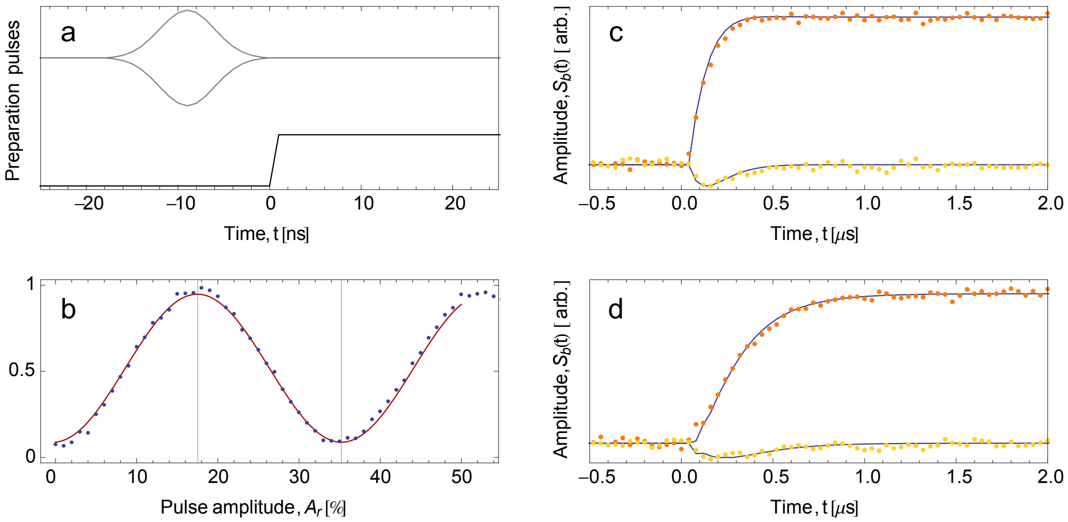

Figure 5.3.: **a**) Pulse pattern for the Rabi experiment. On top the gaussian shaped (gray) microwave pulse at the qubit frequency with variable amplitude A_r. Below the measurement tone (black) at the resonator frequency. **b**) Extracted qubit populations from the experiments for different amplitudes. **c**) Measurement trace of the resonator response when the qubit is in the $|g\rangle$ state. Each of this type of traces allow the extraction of the qubit population in this experiment, by comparison to the theoretical model. **d**) same as **c**) for the qubit in the $|e\rangle$ state.

prepared in this experiment are best parametrized by the Rabi angle θ_r

$$|\psi_q\rangle = \cos(\theta_r/2)|g\rangle + \sin(\theta_r/2)|e\rangle. \tag{5.1}$$

The Rabi angle is proportional to the applied amplitude A_r and is given by

$$\theta_r = \pi A_r / A_{r,\pi}, \tag{5.2}$$

where $A_{r,\pi}$ is the smallest amplitude necessary to prepare the $|e\rangle$ state which corresponds to a Rabi angle of π. By extracting the value for $A_{r,\pi} = 17.5\,\%$ from this measurement we effectively have established a calibration to prepare any qubit state parametrized by Eq. (5.1).

As the last calibration experiment we characterize the interaction between qubit and resonator. For this experiment the qubit is prepared in the $|e\rangle$ state by a microwave pulse like in the previous experiment. Subsequently we tune the qubit frequency towards the resonator frequency by applying a square pulse to the flux line with an amplitude A_{vr} and a length t_{vr}. When the qubit comes close to the resonator it exchanges its excitation coherently back and forth with the resonator during the time t_{vr}. By measuring the qubit population after the flux pulse (Fig. (5.4c)) we observe this interaction as *vacuum Rabi oscillations* which are theoretically treated in Ref. [42] and measured in Ref. [46]. The frequency of these oscillations takes a minimum of $g/\pi = 108\,\mathrm{MHz}$ at the point where the qubit frequency during the flux pulse matches the resonator frequency. At this particular amplitude of the flux pulse which is denoted by $A_{\mathrm{vr},0}$ also the contrast of the oscillation reaches a maximum and the qubit population

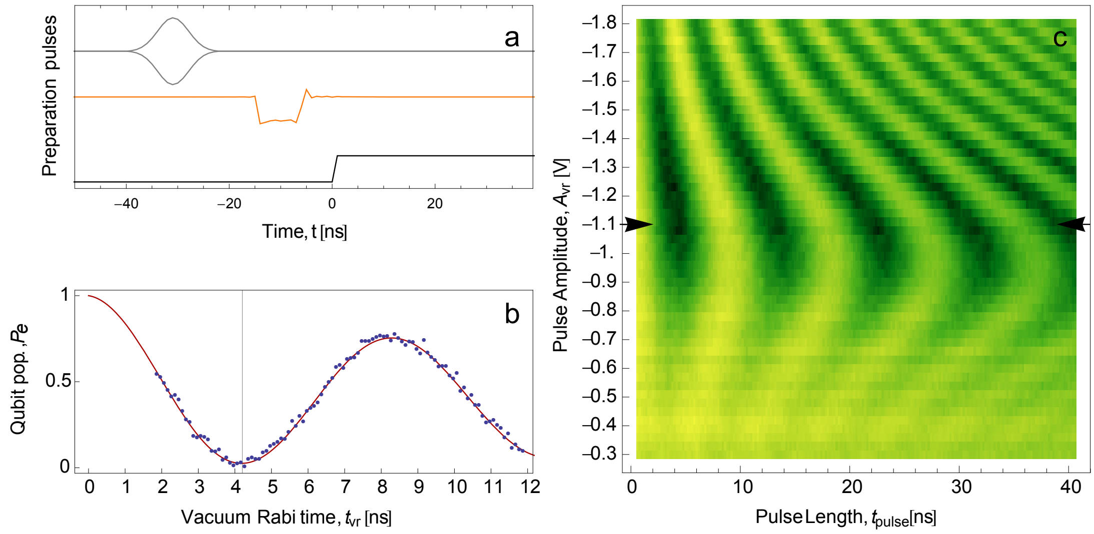

Figure 5.4.: **a**) Pulse pattern for the vacuum Rabi experiment. On top microwave pulse (gray) which corresponds to a rotation $\theta_r = \pi$ and prepares the qubit in the $|e\rangle$ state. Subsequently a pulse on the flux line (orange) to tune the qubit frequency. Finally the measurement tone is turned on to measure the qubit state. **b**) Extracted qubit populations for different lengths of the flux pulse with the height of -1.1 V. **c**) Plot of the qubit population (bright:1, dark:0) after the vacuum Rabi experiment with variable pulse lengths and amplitudes.

oscillates between 0 and 1 as shown in Fig. (5.4b).

In principle, oscillation pattern in Fig. (5.4c) should be symmetric about $A_{\mathrm{vr},0}$ because the form of the vacuum Rabi oscillations only depends on the absolute value of the detuning between qubit and resonator. In the experiment though, we observe a clear asymmetry between the part where the qubit crosses the cavity (upper part of Fig. (5.4b)) and the part where it does not (lower part). This asymmetry can be reproduced in simulations and is attributed to the imperfections of the square pulse such as the finite rise-time and overshoots. To minimize the effect of these imperfections we investigated pulse correction schemes as they are described in App. A. This correction method also enabled us to improve the time resolution of the flux pulse length to 0.1 ns.

The controlled interaction between qubit and resonator can finally be used to perform an operation in which the qubit state is coherently mapped to the state of the resonator. If the qubit was prepared in a state $|\psi_q\rangle = \alpha|g\rangle + \beta|e\rangle$ and the interaction time is chosen as $t_{\mathrm{vr}} = t_{\mathrm{vr},0} = \pi/(2g) = 4.6$ ns corresponding to half a vacuum Rabi oscillation the state of the system after the interaction is then

$$|\psi_{sys}\rangle = |g\rangle \otimes (\alpha|0\rangle + i\beta|1\rangle). \tag{5.3}$$

In this sense the initial superposition state of the qubit is mapped to a superposition state of zero and one resonator photon while the qubit ends up in the ground state. To achieve this operation we first find the amplitude $A_{\mathrm{vr},0}$ where qubit and resonator frequencies match during the flux pulse. For this amplitude we find the smallest pulse length leaving the qubit in the

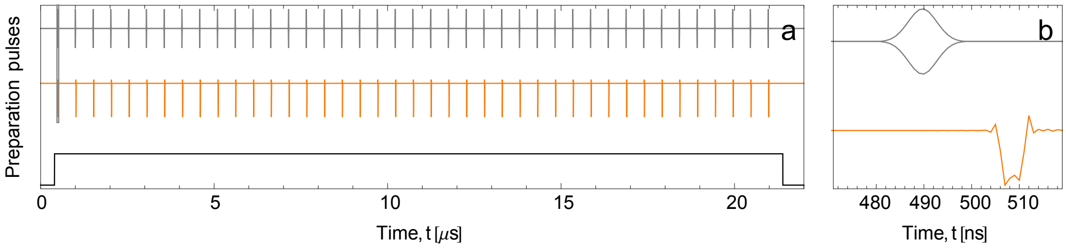

Figure 5.5.: **a**) Pattern for the generation of 40 photons. Top: microwave pulse (yellow). Middle: flux pulses (orange). Bottom: trigger defining the measurement window (20.48 μs) of the FPGA (black). **b**) Zoom in to one preparation of a photon.

ground state. The fact that the qubit reaches the ground state ($P_e < 0.05$) serves as a good criterion to determine the point where the mapping is successful and the effective interaction time is $t_{\mathrm{vr},0}$. This is because on the time scale of $t_{\mathrm{vr},0}$ the other dissipative effects, photon decay and qubit decay, are negligible, so that we can assume that the only channel by which the qubit gets de-excited is the energy transfer to the resonator.

The plot in Fig. (5.4b) is taken for the flux pulse amplitude $A_{\mathrm{vr},0}$ and shows that after a pulse of nominal length of 2.2 ns the qubit ends up in the ground state. The difference of 2.4 ns between the nominal pulse length and inferred interaction time can be explained by the finite rise and fall times of the square pulse which are known to be on the order of 2 ns.

5.3. Implementation and characterization of a single photon source

Qubit state preparation and the mapping of the qubit state to the resonator state can now be used to implement a deterministic single photon source. In the first step we prepare a qubit superposition state parametrized by the Rabi angle θ_r. This state is mapped to the resonator by vacuum Rabi oscillations resulting in a single photon superposition state

$$|\psi\rangle = \cos(\theta_r/2)|0\rangle + \sin(\theta_r/2)|1\rangle. \tag{5.4}$$

For the implementation of the single photon source we use the pulse sequence in Fig. (5.5) where we perform 40 photon preparations, one every $t_{\mathrm{p}} = 512\,\mathrm{ns}$. Each photon preparation consists of a qubit preparation pulse with amplitude $A_{r,\pi}\theta_r/\pi$ followed by a flux pulse with amplitude $A_{\mathrm{vr},0}$ and length $t_{\mathrm{vr},0}$ as calibrated from the vacuum Rabi experiment (Fig. (5.5b)).

In the preparation of this pattern several timing constraints were taken into account which are worth to be mentioned. As indicated in the pattern scheme in Fig. (5.5) the measurement of the FPGA takes a time of 20.48 μs. This measurement window is fixed and is imposed by the implementation of the discrete Fourier transform (DFT) used in the data processing algorithm. The implicit assumption of the DFT that signals are periodic makes it desirable to prepare signals which are either periodic in the time window of 20.48 μs or continuous[2]. The repetition period t_p was therefore chosen as the smallest commensurable time bigger than the typical cavity decay time.

Furthermore the phases of the preparation pulses were adjusted carefully to achieve identical photon preparations. The reference frame used in our experiments to define the phases of signals is fixed at the resonator frequency. In this reference frame the microwave signal used in the qubit state preparation acquires a phase shift of $(\omega_a - \omega_r)t_\text{p}$ between two subsequent photon preparations. This phase is compensated by the the pulse modulation signal so that all prepared photons in one sequence have the same relative phase. To ensure additionally that the phases between all repetitions of the sequence are the same we chose the repetition time as 25 μs and round the relevant frequencies ω_r, ω_a to be commensurable with $(25\,\mu\text{s})^{-1} = 40\,\text{kHz}$.

The measurements presented in the following are all based on the preparation scheme discussed above. The only free parameter which is varied in the experiments is the Rabi angle θ_r to prepare different initial photon states in the cavity.

5.3.1. Quadrature measurements

To characterize the single photon source we first measure the time-resolved average of the complex envelope on one output channel. This gives us the time dependent expectation value of the annihilation operator of the cavity for the state prepared in the cavity

$$\langle S_b(t)\rangle = g_b\sqrt{\kappa_b}\,\langle a(t)\rangle\,. \tag{5.5}$$

For each prepared state the experiment was repeated for about 8×10^5 times. The data of the 40 photons in one sequence is collapsed to one response and the global phase was chosen such that the relevant signal is in the real part of our complex measurement outcome.

When preparing a $|\psi_c^+\rangle = (|0\rangle + |1\rangle)/\sqrt{2}$ we observe the leaking out of the prepared photon to the mode b as a characteristic peak with an exponential decay as shown in Fig. (5.6b). The characteristic decay time is given by twice the cavity decay time[3] $2T_\kappa = 102\,\text{ns}$. The rise of this peak is significantly slower than would be expected from $t_\text{vr} = 4.6\,\text{ns}$ due to the limited detection bandwidth of 15 MHz. The rising edge is therefore determined by the last low pass filter in our detection which is nicely reproduced theoretically by including a filter function in Eq. (4.88). The detection bandwidth in these experiments is restricted intentionally to reject as much noise as possible while keeping the signal distortion low.

For different initial cavity states with Rabi angles between $0 \leq \theta_r \leq 2\pi$ we measure the data presented in Fig. (5.6a,c). The real part of this measurement shows a maximum signal for the state $|\psi_c^+\rangle$, no signal for the Fock state $|1\rangle$ and a maximum negative signal for

---

[2] If these are not possible refer to App. B where the zero padding option is presented to circumvent the restriction on periodicity.

[3] This is because the cavity decay time refers to the *energy* decay. Considering the amplitude the exponential decay is half as fast.

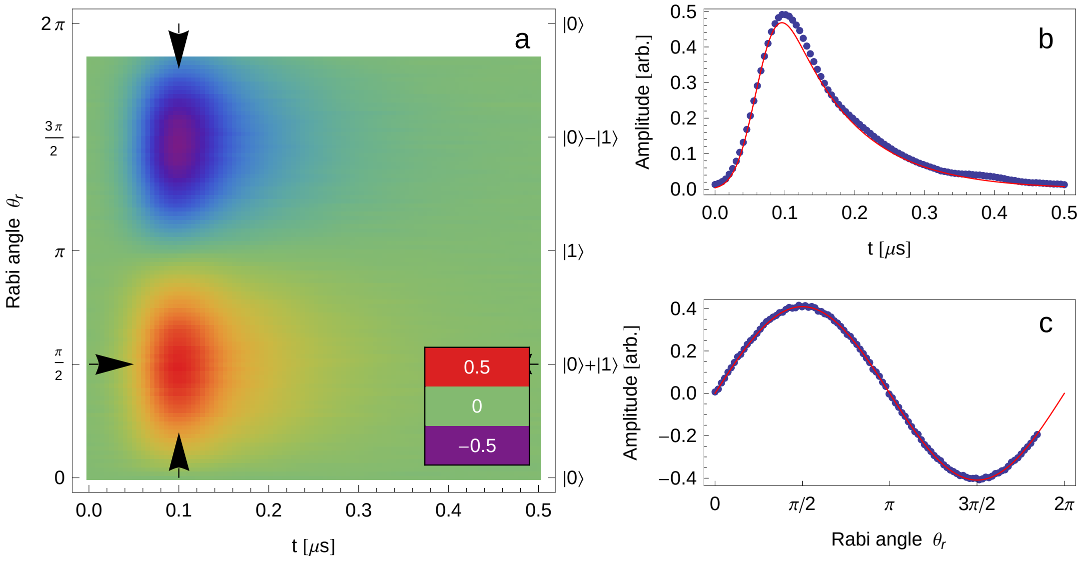

Figure 5.6.: **a**) Real part of the time-resolved quadrature measurement of the single photon source for different states prepared in the cavity (left and right axis). **b**) Single trace from a) for the preparation of the $|0\rangle + |1\rangle$ state. The temporal shape of this signal is fully explained by the cavity decay time (falling edge) and the limited bandwidth of the detection (rising edge). **c**) Quadrature signal at time 0.1 μs for different prepared states. The characteristic oscillation fits excellently to the theoretical model of our single photon source.

$|\psi_c^-\rangle = (|0\rangle - |1\rangle)/\sqrt{2}$. This oscillation of $\langle a\rangle$ with the Rabi angle is characteristic for the states we prepare and fits excellent to the theoretical form of Eq. (4.76) as demonstrated in Fig. (5.6c).

The imaginary part of the measurement result is omitted since it shows hardly any signature of the prepared photons. In fact small deviations are present in the imaginary part but were not further investigated in this thesis. They are assumed to be due to the non-linearity of the qubit/cavity system. This can induce a self-phase modulation which can lead to a small intensity-dependent phase shift becoming visible in the imaginary part.

5.3.2. Power measurements

After investigating the average quadrature amplitudes we measured the time-resolved average of the emitted power. For the preparation of the single photon Fock state $|1\rangle$ ($\theta_r = \pi$) we first measured the power emitted from the two ends of the cavity $\langle S_b^*(t)S_b(t)\rangle$ and $\langle S_c^*(t)S_c(t)\rangle$ as well as the cross-power between these channels $\langle S_b^*(t)S_c(t)\rangle$ which are shown in Fig. (5.7).

The peak which is clearly visible in these measurements is caused by the photon leaking out from the cavity and allows us to determine the effective noise temperature of both our detection chains. By a simple argument we can compare the area under the peak corresponding to an energy of $\hbar\omega_r$ with the background power which is due to the amplifier noise and find for both channels effective noise temperatures of $\sim 17K$. From an analytical model (solid lines) based on Eq. (4.89) including noise and filtering we can reproduce the data correctly and get

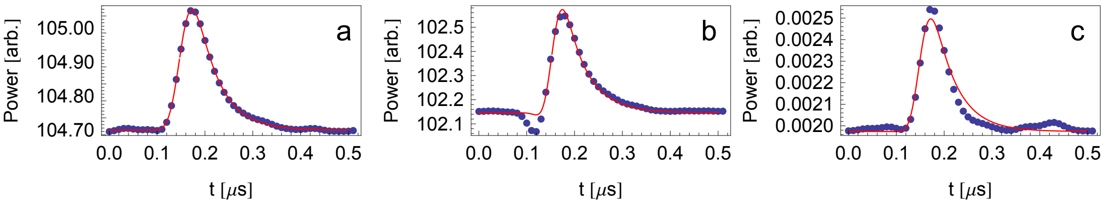

Figure 5.7.: Time-resolved power measurements with the characteristic peaks from the photon generated in the cavity. **a**) Power on channel b. **b**) Power on channel c. **c**) Cross-power between channels b and c.

similar values for the noise temperature on both channels. In the case of the cross-power measurement most of the amplifier noise is rejected, because the noise between both channels is mostly uncorrelated. The residual correlated noise is a factor of 500 smaller than the noise on each channel. It can have several technical origins such as insufficient isolation between both lines, thermal noise in the resonator and imperfections in the circulators.

All three of these measurements give us in principle access to the same physical quantity of our system which is the time-resolved expectation value of the cavity photon number $\langle n(t)\rangle$, as it was shown in Sec. 4.3.1. In the further investigation of the cavity photon number we will only use measurements of the cross-power because the noise is effectively rejected and the residual detected noise is reduced to the single photon level.

The cross-power was measured for the cavity states characterized by $0 \leq \theta_r \leq 2\pi$ for 3.2×10^8 times for each state. The result in Fig. (5.8a) shows the maximum signal for the Fock state $|1\rangle$ and a characteristic dependence on θ_r. This dependence is analyzed in Fig. (5.8c) and fits the expected photon number dependence $\langle n\rangle = \sin^2(\theta_r/2)$ from Eq. (4.78). The time dependence for the peak in the measurements is shown in Fig. (5.8b) and fits well with the theoretical line where the limited bandwidth of the detection is accounted for. The deviations in this time dependence are expected to be of technical rather then of physical origin and are probably due to a known asymmetry in the filtering.

5.4. First-order correlation function measurements

In a next step the first-order correlation function of the single photon source was measured. Based on the findings in Sec. 4.3.2 we performed cross-correlation measurements between both detection chains which are described by

$$\Gamma^{(1)}(\tau) = \int \left\langle S_b^\dagger(t) S_c(t+\tau) \right\rangle dt = g_b g_c(\sqrt{\kappa_b\kappa_c}G^{(1)}(\tau) + G_{bc}(\tau)). \tag{5.6}$$

To get the first-order correlation we removed the correlated background noise G_{bc} by subtracting a reference measurement as described by Eq. (4.51) which gives us the quantity

$$G^{(1)}(\tau) - {G^{(1)}}_{\mathrm{ss}}(\tau) \approx G^{(1)}(\tau). \tag{5.7}$$

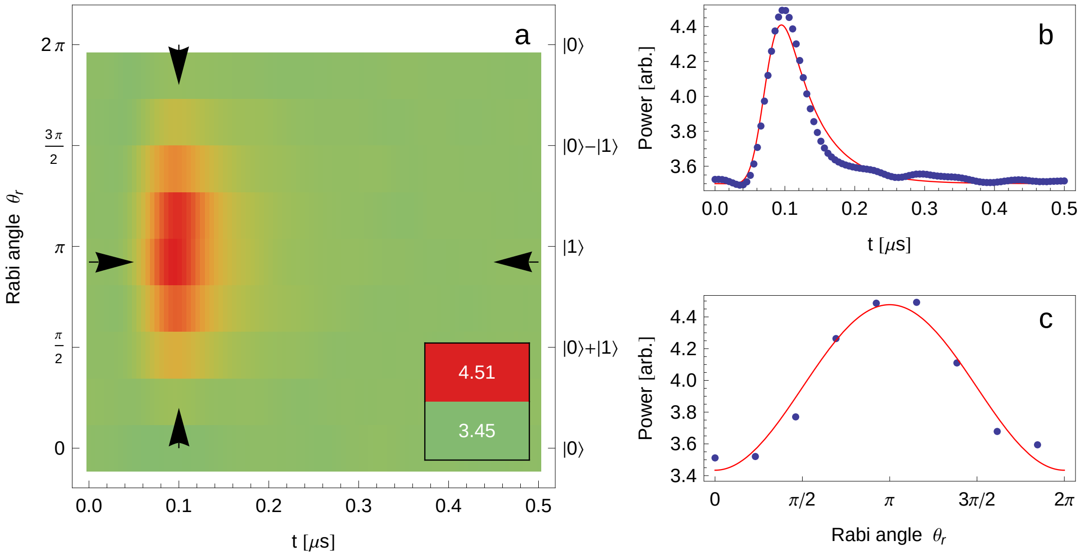

Figure 5.8.: **a**) Time-resolved cross-power measurement of the single photon source for the same family of states as in the quadrature measurement. **b**) Single trace from a) for the preparation of a $|1\rangle$ state. The temporal shape is explained by the cavity decay time and the limited bandwidth (red line). **c**) Cross-power at time $0.1\,\mu$s for the different prepared states. The characteristic oscillation fits well to the theoretical model of the single photon source.

It is assumed that the steady state is close to the ground state and $G^{(1)}{}_{\mathrm{ss}}(\tau) \approx 0$. This measurement was implemented by alternating measurements with the preparation sequence turned on and off. This has the advantage that G_{bc} is removed efficiently and is robust to drifts in amplifiers and other devices because the reference is measured only $25\,\mu$s after the actual measurement.

For the preparation of the equal superposition state $|\psi^+\rangle$ ($\theta_r = \pi/2$) with 1.2×10^8 repetitions of the experiment we find the middle trace in Fig. (5.9a). Note that the data is offset for visibility. The form of this correlation function is dominated by peaks at integer multiples of the repetition time $t_\mathrm{p} = 512\,$ns of the photon generation. The shape of these peaks is given by a combination of the cavity decay time $T_\kappa = 51\,$ns and the low pass filtering in the detection. The middle peak at $G^{(1)}(0)$ shows the interference of each photon with itself and is characterized in height by the average photon number ($G^{(1)}(0) \propto \langle n(0) \rangle$). The other peaks are results of interference between subsequent photons and are described in height by $G^{(1)}(nt_\mathrm{p}) \propto \left\langle a^\dagger \right\rangle \langle a \rangle$.

In Fig. (5.9b) we analyzed the peak height for the center peak (red) and the side peaks (blue). For the Fock state one observes the maximum for the center peak because it has the highest photon number in the family of states we prepare. At the same time, the interference between subsequent photons in the Fock state disappears due to the completely undefined phase of this state (Fig. (5.9a) top). This interference is maximized by the equal superposition states $|\psi^\pm\rangle$ because it is the state with the most well defined defined phase.

If we look at the theoretical dependence of the peak heights on the Rabi angle θ_r in Fig. (5.9b)

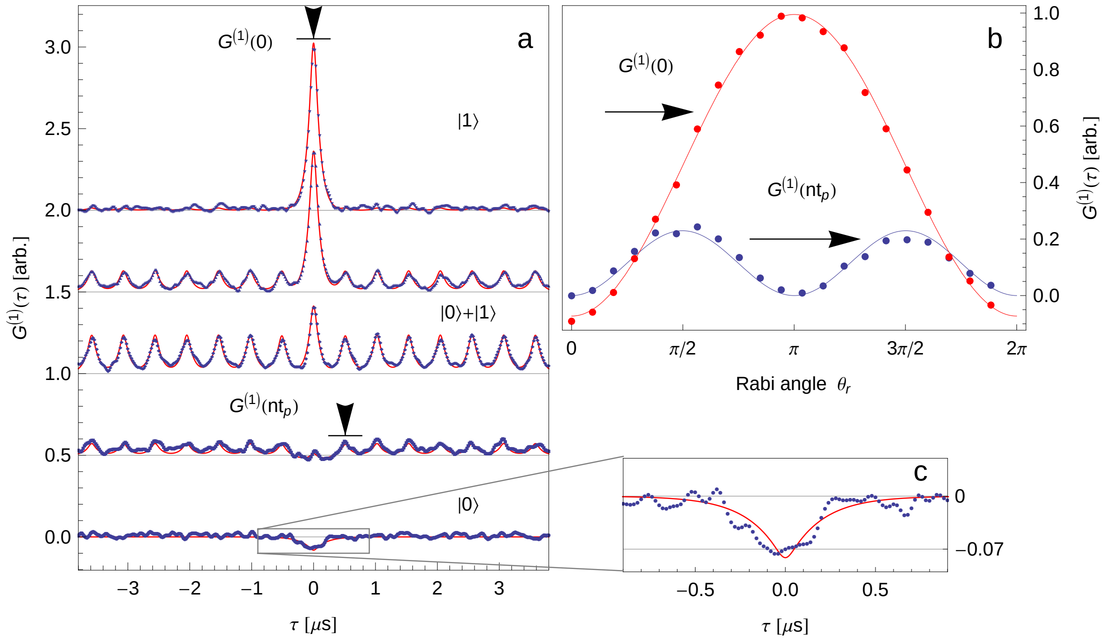

Figure 5.9.: **a**) First-order correlation measurements for different states of the single photon source. **b**) Analysis of the middle peak height $G^{(1)}(0)$ and the outer peak heights $G^{(1)}(nt_\mathrm{p})$. **c**) Zoom into the small dip observed when preparing the $|0\rangle$ state.

we find excellent agreement with the model from Eq. (4.83) and Eq. (4.84). In fact we understand not only the peak heights but the full time dependence of the correlation function as can be seen by the theoretical lines in Fig. (5.9a) by the model from Eq. (4.100).

Cooling

Finally, we explain the small dip in the $G^{(1)}(\tau)$ data when preparing the $|0\rangle$ state. Although $G^{(1)}$ for this state should be 0 we observe the dip shown in Fig. (5.9c). During the state preparation the qubit is prepared in a $|0\rangle$ state. In the interaction with the resonator the qubit absorbs any existing thermal photon in the resonator and emits it later at a different frequency. This is possible because the qubit thermal population is normally much lower than the thermal population of the resonator, because external noise at the qubit frequency cannot enter the resonator and reach the qubit. In this way the state preparation *cools* the resonator field which can be measured as the dip in Fig. (5.9c) due to the subtraction of the steady state signal as expressed by Eq. (5.7). In fact, the depth of this dip indicates the number of photons by which we cool with a successful state preparation in this case $n_\mathrm{th} = 0.07$. If we assume that fidelity of our state preparation is high this corresponds to the thermal population of the resonator in the steady state. The equivalent temperature of 115 mK agrees very well with independent measurements [47] in which we extracted a field temperature of ~ 100 mK.

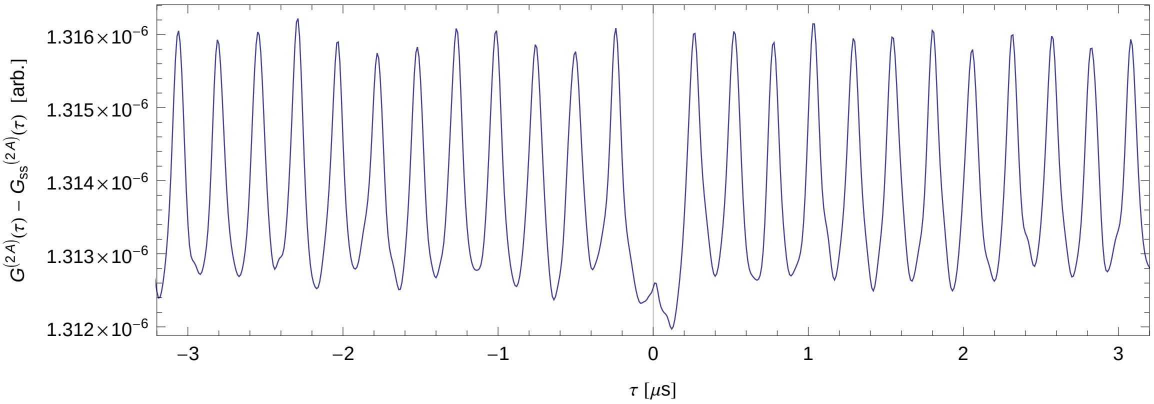

Figure 5.10.: Second-order correlation measurement for the $|1\rangle$ state for a repetition time of 256 ns.

5.5. Second-order correlation function measurement

As a last measurement we present the second-order correlation function. For technical reasons this data was taken in a different sample using an integrated on-chip beam splitter. As shown in App. C.5 this setup is equivalent to the one described above.

The source is the same single photon preparation scheme as before which we use to prepare the $|1\rangle$ state in the cavity every 256 ns. The measurement we perform is

$$\Gamma^{(2A)}(\tau) - \Gamma_{\mathrm{ss}}^{(2A)}(\tau) = g_b^2 g_c^2 \kappa_b \kappa_c G^{(2)}(\tau) + C' \tag{5.8}$$

as given by Eq. (4.56) and shown in Fig. (5.10). The center peak at $\tau = 0$ is significantly smaller than the other peaks at integer multiples of the repetition time. This is the necessary condition for the observation of photon-antibunching which therefore demonstrates the non-classical nature of the radiation produced in our experiment. In fact, this type of measurement outcome is the characteristic feature of a single photon source and was demonstrated in a variety of optical systems [48, 49].

Two issues in these measurements are left open for future work. The residual peak at $\tau = 0$ is non-zero and should be quantified. This residual bunching in the generated photons is most probably due to the cases when the state preparation generates a $|2\rangle$ state as discussed in Sec. 4.4.1. Furthermore we did not try to estimate the value of the background C' which is possible from other reference measurements as described in Sec. 4.3.3.

6. Conclusion and Prospects

The goal of this thesis was the realization of measurements of correlation functions of the electric field to investigate non-classical microwave radiation. The necessary work to achieve this goal was structured in three steps.

In the theory part of this thesis we discuss how the complex envelope of the electric field can be measured using standard microwave equipment. It turns out that this type of measurement can be conveniently described in terms of quantum mechanical measurement operators including all relevant influences of the detection system. By measuring different statistical moments of these operators it is shown to be possible to extract amongst other quantities the first and second-order correlation function of field under consideration.

Based on the theoretical results, we developed a signal processing algorithm to extract the desired information from the available measurement signals. The efficiency of the final solution was the main design goal, since the high level of noise in our system required an extensive amount of experimental repetitions. The algorithm was finally implemented in hardware using a field programmable gate array (FPGA) which allows us to perform measurements with close to optimal utilization of the measurement time. The system was optimized such that it achieves a computational performance equivalent to over 10 GFlops on a data stream of 1 TByte/h.

To demonstrate the performance of our system in the quantum regime we implemented a source emitting non-classical microwave radiation. This source was realized in a superconducting electronic circuit consisting of a microwave resonator and an artificial atom of the transmon type which is known as circuit QED. We showed in this system that we can deterministically prepare a family of *single photon states* by controlling the state of the atom and its interaction with the light field. The working of the source was verified by a number of time-resolved measurements which are in excellent agreement with our theoretical understanding of this source.

In the end, we were able to demonstrate successful measurements of the first- and second-order correlation function of the single photon source. In particular, we were able to observe antibunching of microwave photons which was not reported before and is known to be a strictly quantum mechanical effect. This shows that the methods we apply are not restricted to classical states of light, but work correctly for non-classical radiation.

By developing these new measurement method we created a novel tool in the investigation of the quantum mechanics of microwave light fields. It will allow us to observe more properties of propagating microwave radiation than before, opening up a new realm of possible experiments. In that sense our measurements can be seen as a starting point for the investigation of a variety of other phenomena, e.g. squeezing or photon blockade in circuit QED systems.

The main limitation to this measurement and to all the developed techniques is clearly the high level of noise in the current detection system based on high electron mobility amplifiers. A novel type of amplifier, as the currently investigated parametric amplifier, could greatly reduce the noise and improve the detection efficiency. The current measurement times of hours and days would then be reduced by one or more orders of magnitude and would allow for many more exciting experiments, such as quantum state tomography of propagating microwaves or tests of non-locality through violation of Bell-type inequalities.

Appendices

A. Pulse Correction

This chapter summarizes the efforts to generate high-quality pulses used in the local flux control of our qubits. We start with a review of the theory of time-discrete signals and then propose an algorithm to correct pulse shapes in the presence of imperfections in real-world signal generation.

A.1. Shannon sampling theorem

To generate fast, high quality pulses to control qubits on a nano second time scale *arbitrary waveform generators* (AWGs) are an indispensable tool. These devices are programmed with an arbitrary time-discrete signal (or *waveform*) which they convert to a time-continuous voltage signal. To have a meaningful description for the conversion between time-discrete and time-continuous signals we introduce the Shannon Sampling Theorem.

Assume a continuous signal $x(t)$ and its Fourier transform $X(f) = F\{x(t)\}$ satisfy the following relation

$$X(f) = 0 \qquad \text{forall} \quad |f| > \frac{B}{2}, \tag{A.1}$$

where B is a frequency limiting the bandwidth of $x(t)$. If the sampling rate $1/T_s > B$, it can be shown [50] that $x(t)$ is fully described by the sampled signal

$$x[n] = x(nT_s). \tag{A.2}$$

In other words no information is lost if a continuous signal is sampled, given that the sampling frequency $1/T_s$ is bigger than the *Nyquist-frequency* $B/2$. In this case $x(t)$ can be reconstructed from $x[n]$ by

$$x(t) = \sum_{n=-\infty}^{\infty} x[n] \operatorname{sinc}\left(\frac{t - nT_s}{T_s}\right), \tag{A.3}$$

where the normalized sinc function is

$$\operatorname{sinc}(x) = \frac{\sin(\pi x)}{\pi x}. \tag{A.4}$$

The reconstruction from Eq. (A.3) can be seen as a discrete convolution of $x[n]$ with a kernel (or impulse function) $h(t) = \mathrm{sinc}(t/T_s)$ given by

$$x(t) = x[n] * h(t - nT_s) \tag{A.5}$$

A.2. Signal reconstruction

In any real system the ideal reconstruction as in Eq. (A.3) is in principle impossible to implement since the sinc function extends up to $t = \pm\infty$. Instead other kernels can be used to approximate the ideal signal.

A.2.1. Zero-order hold

One common choice for such an approximation is the *zero-order hold* (ZOH) where a given signal level is kept constant during one sampling period. The kernel for this type of 0th-order interpolation is given by

$$h_{\mathrm{ZOH}}(t) = \begin{cases} 1 & 0 < t < T_s \\ 0 & else \end{cases}. \tag{A.6}$$

The higher frequency components in the reconstructed signal can afterwards be filtered by a low-pass filter at half the sampling frequency

$$F_{\mathrm{lp}}(f) = \begin{cases} 1 & |f| < \frac{1}{2T_s} \\ \epsilon \ll 1 & else \end{cases}. \tag{A.7}$$

In Fig. (A.1) the spectrum of the zero-order hold is compared to the ideal reconstruction and shows a characteristic roll-off towards the Nyquist frequency due to the constant interpolation in the time domain. The

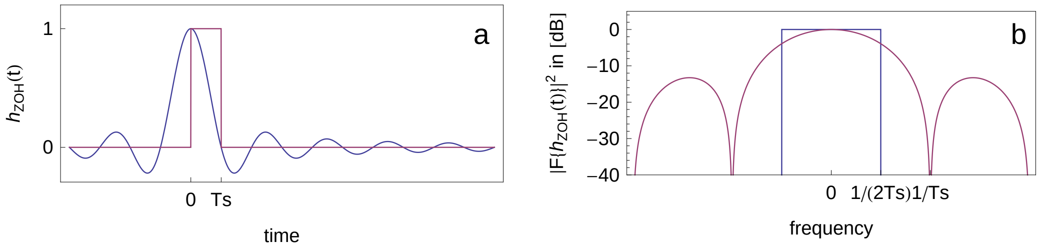

Figure A.1.: **a**) Theoretical impulse response of a zero-hold digital analog conversion (red) and a sinc for the ideal signal reconstruction (blue) with a sampling time T_s. **b**) Spectra of a) with the characteristic roll off towards the Nyquist frequency for the zero-order hold. Also the out-of-band high-frequency components are clearly visible and a distortion compared to the ideal reconstruction (blue).

A.2.2. General kernels

As a general model for the generation of signals, we want to describe a system consisting of two parts. First an AWG transforms a given waveform $x[n]$ to a voltage signal, which is filtered by a linear system described by the transfer function $G(f)$. The resulting time continuous signal can be written in this case as

$$y(t) = g(t) * (x[n] * h(t - nT_s)), \tag{A.8}$$

where $g(t) = F^{-1}\{G(f)\}$ is the impulse response of the channel filter. By using the commutation relations for the convolution we can simplify this expression and find

$$\begin{aligned} y(t) &= x[n] * (g(t) * h(t - nT_s)) \\ &= x[n] * \tilde{h}(t - nT_s)), \end{aligned} \tag{A.9}$$

where now the complete description of the system is in the kernel $\tilde{h}(t)$. In fact this kernel can be measured by applying a test signal $x[n] = \delta[n]$:

$$y(t)\Big|_{x[n]=\delta[n]} = \delta[n] * \tilde{h}(t - nT_s)) = \tilde{h}(t). \tag{A.10}$$

Having a measurement of this impulse function we have a full characterization of the signal generation chain and can *predict* with Eq. (A.9) the exact form of the output signal for any given waveform.

A.3. Signal correction

Being able to predict the resulting signal for any given waveform allows us to correct for the distortions of the AWG and the channel. This can be done by finding the waveform which results in a signal most similar to the desired signal. It is clearly impossible to achieve *any* arbitrary desired signal at the output, since the available frequency and amplitude range are always limited by the channel bandwidth as well as the AWG bandwidth and amplitude range. We present instead a method to find a waveform which approximates a desired signal in a least-square error sense using linear regression.

A.3.1. Signal prediction by linear mapping

To find an applicable algorithm we want to restrict all signals to finite length and assume for the resulting signal $y(t)$ the kernel $h(t)$ and the waveform $x[n]$

$$\begin{aligned} y(t) &\neq 0 \quad \text{only for} \quad 0 \leq t \leq t_y \\ h(t) &\neq 0 \quad \text{only for} \quad 0 \leq t \leq t_h \\ x[n] &\neq 0 \quad \text{only for} \quad 0 \leq nT_s \leq t_x. \end{aligned} \tag{A.11}$$

Under these restrictions $x[n]$ can be written as a vector $\mathbf{x}$ of length $l_x = \lceil t_x/T_s \rceil$ and Eq. (A.9) becomes a linear equation

$$y(t) = (h(t), h(t - T_s), \dots, h(t - (l - 1)T_s)) \cdot \mathbf{x}, \tag{A.12}$$

where $\mathbf{x}$ is multiplied by a time dependent row vector constructed from $h(t)$.

To treat this equation numerically we replace the time-continuous signals $y(t)$, $h(t)$ by quasi-continuous signals which are sampled with a very high sampling rate $(1/T_c)$ with respect to the relevant frequencies/time scales. To simplify the calculation T_c will be assumed to be an integer fraction of T_s, e.g. $T_s = 10T_c$. Then we write

$$\begin{aligned} y[n] &= y(nT_c) \\ h[n] &= h(nT_c), \end{aligned} \tag{A.13}$$

also as vectors $\mathbf{y}$ of length $l_y = \lceil t_y/T_c \rceil$ and $\mathbf{h}$ of length $l_h = \lceil t_h/T_c \rceil$. This reduces Eq. (A.12) for the output signal $\mathbf{y}$ to a matrix equation

$$\mathbf{y} = H \cdot \mathbf{x}, \tag{A.14}$$

where H is a $(l_y \times l_x)$-matrix whose elements are given by

$$H_{i,j} = h(iT_c - jT_s) = h[i - j\frac{T_s}{Tc}]. \tag{A.15}$$

Note that we use an unusual convention and start counting rows(columns) from 0 to $l_y - 1(l_x - 1)$.

A.3.2. Solving by linear regression

The description how a waveform is translated to a signal was reduced by Eq. (A.14) to a simple multiplication by the matrix H. Trying to solve this equation for a given $\mathbf{y}$ will always result in a highly overdetermined system of equations, because $t_x \approx t_y$ will lead to $l_y \gg l_x$. It implies that not all desired signals $\mathbf{y}$ are in the image space of H and therefore not reachable by any waveform $\mathbf{x}$. This fact is mearly a reflection of the physical restrictions imposed by the system due to the finite sampling time and the channel distortions. The best thing which can be done is to find an $\mathbf{x}$ which minimizes the error $\|\mathbf{y} - H\mathbf{x}\|$ for some given norm. For a quadratic norm the problem reduces to a linear-regression. The solution to the linear regression can be described analytically by the pseudo-inverse L of the mapping matrix H as

$$\mathbf{x} = L \cdot \mathbf{y}, \tag{A.16}$$

with the pseudo-inverse calculated from

$$L = \left(H^{\mathsf{T}} H\right)^{-1} H^{\mathsf{T}}. \tag{A.17}$$

A.3.3. Weighting the error

This linear regression technique will find a waveform which resembles a given output signal best in a least square error sense. The error will be minimized over all points in time uniformly. In some cases it is desirable though that the error in some parts of the signal are minimized at the cost of more irrelevant parts. For our experiment e.g. the flattness during the plateau of a square pulse was most important whereas overshoots and the form of the edges were less important.

For these cases the linear regression technique can be extended by introducing weights for the error at all points in time. These weights can be given as a vector $\mathbf{w}$ of equal length as $\mathbf{y}$ by quantifying the importance of the corresponding point in $\mathbf{y}$ on a scale from 0 (unimportant) to 1 (important). We write this vector as a diagonal matrix $W = \mathrm{diag}\left(\mathbf{w}\right)$ and write down a modified linear regression problem

$$\mathbf{y}' = H' \cdot \mathbf{x} \tag{A.18}$$

where $\mathbf{y}' = W \cdot \mathbf{y}$ and $H' = W \cdot H$. By solving this equation we find a $\mathbf{x}$ such that the residual error $\|\mathbf{y} - H\mathbf{x}\|$ is distributed in time according to $\mathbf{w}$.

A.3.4. Algorithm

Summing up the above derivation the following algorithm allows to find an optimal waveform for a given desired signal:

1. Define the sampling time of the AWG (e.g. $T_s = 1\text{ns}$) and the sampling time of the quasi-continuous signals (e.g. $T_c = 10T_s = 0.1\text{ns}$).
2. Measure the transfer function $h(t)$ of the signal generating system by applying a waveform $\delta[n]$. The position at which the transfer function is measured determines which parts of the signal chain are included in the correction.
3. Find/Define the length of the transfer function $l_h = t_h/T_c$, the maximal length of the desired signal $l_y = t_y/T_c$ and the waveform $l_x = t_x/T_s$. It is beneficial to respect the relation $t_y \geq t_x + t_h$, which is $l_y \geq l_x \frac{T_c}{T_s} + l_h$, to avoid samples in the waveform which are underdetermined.
4. Calculate the mapping matrix H from the measurement data of the transfer function by Eq. (A.15) and the correction matrix L from Eq. (A.17)
5. Define a desired signal $y(t)$ and calculate its vector $\mathbf{y}$.
6. Calculate the waveform by $\mathbf{x} = L\mathbf{y}$.
7. Check if the achieved signal $\mathbf{y} = H\mathbf{x}$ fulfills your requirements.

Note that for a given system the steps 1-4 have to be done only once and the matrix L can be stored. The modification for error weighting was not included here, because it can be easily included as a modification to the last two steps in the algorithm.

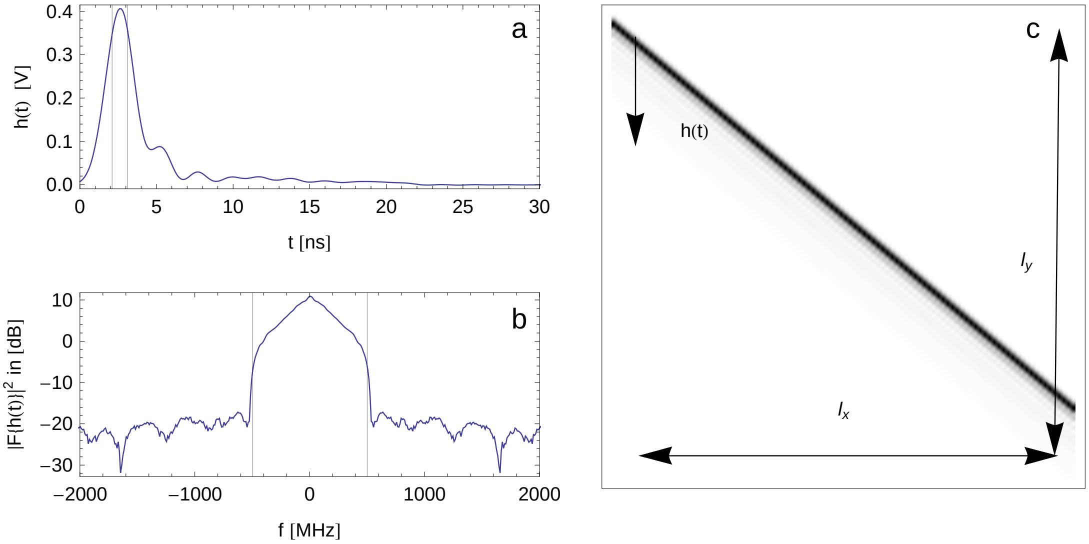

Figure A.2.: **a**) Measured impulse response of the AWG Tek5014 in the 4 V amplitude setting. The shape is clearly different from a sinc in the ideal reconstruction and features trailing oscillations for $t > 5$ns. **b**) Spectrum of **a** with a characteristic roll off towards the Nyquist frequency. Frequency components above this frequency are successfully suppressed by the AWG. **c**) Mapping matrix H constructed from measurement in **a**. Note that normally $l_y \gg l_x$ in contrast to the graphical representation here.

A.4. Examples

As an example we show the results of this algorithm applied to an Tektronix 5014 AWG. The sampling times are chosen as

$$T_s = 1\text{ns} \qquad \text{and} \qquad T_c = 0.1\text{ns} \tag{A.19}$$

The measured impulse response of the AWG is shown in Fig. (A.2a). This measurement was done for the highest amplitude range of the device where clear distortions at the end of the pulse are visible. In Fig. (A.2b) the spectrum of this measurement is shown. As for the perfect reconstruction frequencies above the Nyquist frequency are effectively suppressed. At the same time the spectrum roles off strongly towards higher frequency, which is a clear deviation from the perfect reconstruction.

In the measurement the impulse response pulse vanishes after about 20ns and we restrict ourselves to signals with less than 100ns. We choose for the algorithm

$$\begin{aligned} t_h = 20\text{ns} \quad &\rightarrow \quad l_h = 200 \\ t_x = 100\text{ns} \quad &\rightarrow \quad l_x = 100 \\ t_y = 120\text{ns} \quad &\rightarrow \quad l_h = 1200 \end{aligned} \tag{A.20}$$

The mapping matrix H constructed by Eq. (A.15) is shown in Fig. (A.2c). Using this matrix we can predict the output signal for an uncorrected square pulse which is the blue line in Fig. (A.3b). The distortions by the AWG are predicted to be a slow rising edge and a 10 ns tail after the pulse. As a corrected square pulse we designed a pulse with a controlled rise time and a small gaussian overshoot which is desirable for some of the vacuum Rabi experiments. The algorithm finds a waveform which is predicted to approximate the desired pulse well as can be seen in Fig. (A.3b). Interestingly the corrected pulse is prepared already 20ns before the rising edge as can be seen in Fig. (A.3a) to produce a fast undisturbed edge. This behavior is not added intentionally but rather a result of the optimization procedure.

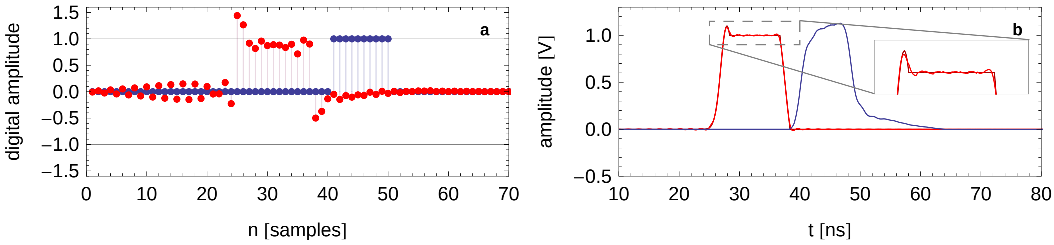

Figure A.3.: **a**) Waveforms of an uncorrected 5ns square pulse (blue) and a corrected square pulse (red). **b**) Predicted output signals calculated from the waveforms in **a** using the mapping matrix H from Fig. (A.2c). The predicted output for the corrected pulse (red) fits nicely to the desired pulse (orange) and reproduces the small requested overshoot precisely (inset).

To verify the effectiveness of the correction we measured different uncorrected and corrected pulses using a LeCroy 13 GHz oscilloscope. First an uncorrected 5 ns square pulse was measured which features the expected defects as can be seen in Fig. (A.4a). Note that this measurement was performed with a lower amplitude setting at the AWG than the previous example and features smaller distortion. In fact, we could observe that the AWG features three internal output configurations which are used in different amplitude ranges. For these configurations the pulse quality decreased for the higher amplitude ranges.

In the second measurement we prepared a square pulse which maximizes the flatness and minimizes the rise time of the pulse. By weighting the error before the plateau very small the correction introduces preparational oscillations which are clearly visible in the output prediction in Fig. (A.4b) (dashed). The measurement of this pulse fits excellently to the prediction and shows that the correction method works correctly.

Finally the correction method was tested for very strong distortions. In this measurement we used a broken filter which was known to introduce strong distortions and introduced an impedance mismatch at the measurement port to create additional reflections. By measuring an uncorrected 5 ns pulse Fig. (A.4c) (blue) we were able to observe the strong distortion of this system including the reflections of the mismatched output. Performing the correction algorithm for this system we measured the red trace in Fig. (A.4c) which is close to an ideal square pulse. In particular the trailing oscillations are completely suppressed demonstrating the strength of our proposed pulse correction scheme.

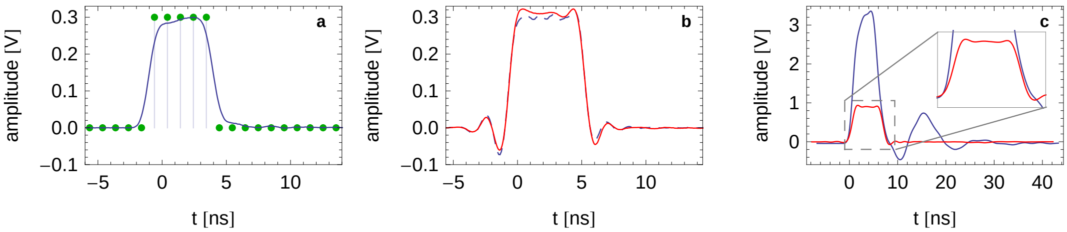

Figure A.4.: Measurements of uncorrected and corrected pulses. **a**) Waveform of uncorrected 5 ns square pulse (green) and measurement of the pulse which is produced by the AWG (blue). Note that the AWG is used in a different voltage range here, so that the distortions are different than in Fig. (A.3b). **b**) Measured corrected 5 ns pulse (red) and theoretical prediction (blue, dashed) where the flatness of the plateau was optimized. **c**) Measurement of uncorrected 5 ns pulse (blue) after a highly distortive filter with an impedance mismatch at the measurement device. Correction produces an excellent square pulse (red) and completely compensates for the AWG and the filter distortion.

B. FPGA Design

In this appendix we present aspects of the implementation of a signal processing design to measure correlation functions of microwave signals. The implementation is based on the *Xilinx Xtreme DSP board* which is currently used in the Qudev Lab [51, 27, 52].

To measure very small correlation signals (e.g. of single microwave photons) one has to perform extensive measurements where large amounts of data are acquired. The main design goal was therefore maximally efficient processing and reduction of the data. The final implementation now can do continuously various mathematical operations on the incoming data and average the results up to 4×10^9 times.

The design follows the pipeline structure depicted in Fig. (B.1), where the continuous flow of data passes different programmable stages. These stages process the data simultaneously and operate truly parallel due to their implementation in independent hardware parts. The data flow is synchronous to the clock speed of the FPGA at 100 MHz and the sampling rate of the analog-digital converters, so that one sample per clock cycle is processed in each stage.

B.1. Signal Processing in the FPGA

B.1.1. Binary representation of real and complex numbers

Before the signal processing chain is described in detail, we introduce a notation how real or complex-valued data points are represented in binary hardware. While in principle there are different possibilities for this representation we use the *fixed-point formats* provided by Xilinx.

To specify the binary format of a real number we write `(U)Fix_N_M`, where U specifies an unsigned number, N the total number of bits to represent the number and M the position of the binary point. For example the binary representation of the number 14.75 as a `UFix_14_6`

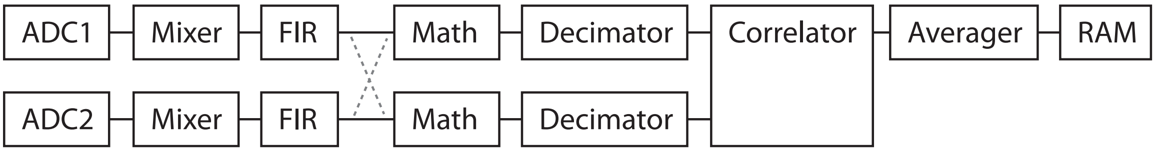

Figure B.1.: Schematic of signal processing pipeline implemented in our FPGA design. The data acquired by two ADCs undergos several processing steps and is finally averaged into the memory of the FPGA. All stages work in parallel allowing for a high data throughput.

is

$$\underbrace{0000001110}_{\text{integer part: 14}}.\underbrace{110000}_{\text{fractional part: 0.75}}. \tag{B.1}$$

A more detailed description of fixed point representations can be found in [53]. It is important to note that all formats have restrictions on the range and accuracy of the numbers they can represent. For unsigned types the maximal and minimal numbers and the smallest possible increment are given by

$$\texttt{UFix\_N\_M}_{\text{Max}} = 2^{N-M} - 2^{-M} \tag{B.2}$$

$$\texttt{UFix\_N\_M}_{\text{Min}} = 0 \tag{B.3}$$

$$\texttt{UFix\_N\_M}_{\Delta} = 2^{-M}, \tag{B.4}$$

whereas for signed types this is

$$\texttt{Fix\_N\_M}_{\text{Max}} = 2^{N-M-1} - 2^{-M} \tag{B.5}$$

$$\texttt{Fix\_N\_M}_{\text{Min}} = -2^{N-M-1} \tag{B.6}$$

$$\texttt{Fix\_N\_M}_{\Delta} = 2^{-M}. \tag{B.7}$$

As an example in a `UFix_14_6` number one can encode numbers from 0 to 255.984375 with a resolution of 0.015625 . For complex numbers we will use `CFix_M_N`, where the real and the imaginary part are encoded in a `Fix_M_N` real number each.

When implementing an algorithm based on fixed point data types special care has to be taken to respect the limited range and accuracy. The mathematical operations performed usually change the range and the accuracy, e.g. a multiplication of two `Fix_14_6` numbers result in a `Fix_28_12` number. To avoid this *bit growth* effect rounding is used to reduce the number of bits after such operations. Since rounding necessarily introduces errors in the algorithm a good trade off between accuracy and resource utilization has to be found in the design procedure.

B.1.2. Sampling and Mixing

The analog data sources on the FPGA board are two *analog-to-digital converters* (ADC) each sampling an incoming voltage signal between ±1.1 V every $T_s = 10\,\text{ns}$ and digitizing it to a `Fix_14_13` number between ±1. Note that although the samples from the ADC come with 14 bit the effective number of bits (ENOB) is only ~ 10.2 bit due to the intrinsic noise of the ADC. The signal from each ADC is multiplied with a local oscillator (LO) as depicted in Fig. (B.2.) The LO signal is generated nummerically in the FPGA and is given by $e^{-i\omega_{\text{IF}}t}$, where the LO frequency ω_{IF} can be chosen for both channels individually. This multiplication results in a complex-valued signal which is stored in a `CFix_17_16` format.

The effect of the mixing operation is a shift of the original signal spectrum such that the frequency ω_{IF} is down converted to d.c. as discussed in Sec. 4.2.1. The output signals of this

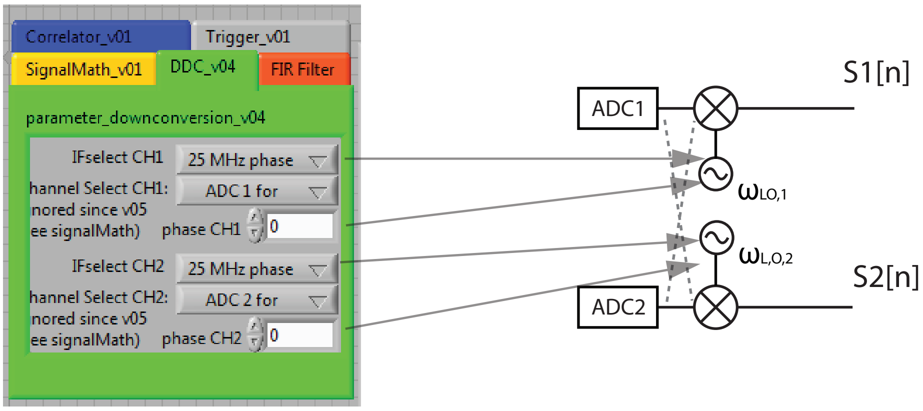

IFselect CH1: 25 MHz phase
hannel Select CH1: nored since v05 ee signalMath): ADC 1 for
phase CH1: 0
IFselect CH2: 25 MHz phase
hannel Select CH2: nored since v05 ee signalMath): ADC 2 for
phase CH2: 0

Figure B.2.: Schematics of the parametrization of the data acquisition on the FPGA board. Dashed lines indicate possible alternative configurations.

stage are:

$$s_1[n] = s_{\mathrm{ADC1}}[n] \cdot e^{-i\omega_{\mathrm{IF},1}T_s n} \tag{B.8}$$

$$s_2[n] = s_{\mathrm{ADC2}}[n] \cdot e^{-i\omega_{\mathrm{IF},2}T_s n}. \tag{B.9}$$

The current implementation depicted in Fig. (B.8) offers three choices for $\omega_{\mathrm{IF}}/2\pi \in \{0\,\mathrm{MHz}, 10\,\mathrm{MHz}, 25\,\mathrm{MHz}\}$. In the case of 25 MHz two different ways of how the LO signal is generated are available. The `25 MHz fast` option achieves higher quality of the LO signal but will not allow to set the phase of the LO as for the `25 MHz phase` option [27]. Furthermore in the case of 0 MHz one can choose that the two input channels are interpreted as the two quadratures of one signal and are combined to one complex signal. This option is useful if both outputs of a single sideband mixer are sampled and results in a signal

$$s_1[n] = s_2[n] = s_{\mathrm{ADC1}}[n] + i s_{\mathrm{ADC2}}[n]. \tag{B.10}$$

B.1.3. Filtering

Following the mixing stage we implemented a programmable filter to reject all undesired frequency components of the incoming signals. Normally these filters are symmetric low passes and define the detection bandwidth of the measurement. We will just describe the implementation and refer to Ref. [54] for a general discussion of digital filters.

For the implementation we chose *13-tap real symmetric finite impulse response* (FIR) filters which are readily available in the Xilinx toolset and offer a good compromise between resource requirements and flexibility. A FIR filter is defined by its impulse response $h[k]$ which has only a finite number of non-zero elements as show in Fig. (B.3). For a 13-tap real symmetric FIR

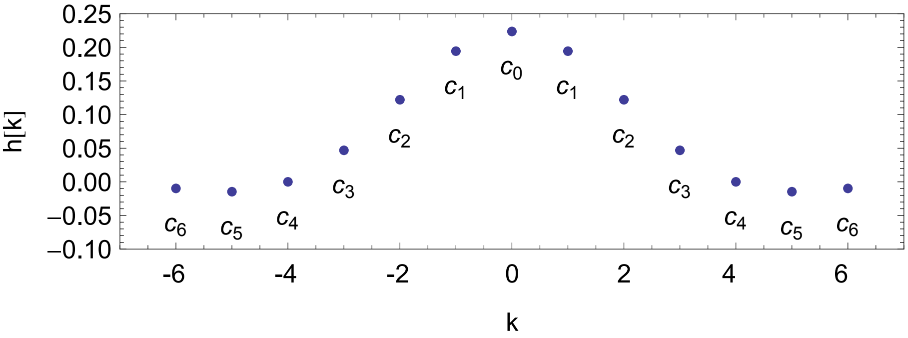

Figure B.3.: Impulse response of a 13-tap symetric FIR filter. The response is given by 7 coefficients c_i.

we have the following restrictions on this response

$$\begin{aligned} \text{Symmetry:} \quad & h[k] = h[-k] \\ \text{Length:} \quad & h[k] = 0 \quad \text{for } |k| > 6 \\ \text{Real:} \quad & h[k] \in \mathbb{R}. \end{aligned} \tag{B.11}$$

In this case the filter can be described by 7 coefficients $c_{0,1,..,6}$ which define its response as:

$$h[k] = \begin{cases} c_{|k|} & |k| \leq 6 \\ 0 & \text{else} \end{cases}. \tag{B.12}$$

Finally the output $s'[k]$ of the filter is given by the convolution of the input signal $s[k]$ with the impulse response $h[k]$

$$s'[k] = \sum_l s[k-l]h[l] = \sum_{l=-6}^{6} c_l s[k-l]. \tag{B.13}$$

To use these filters as tunable bandwidth filters we designed a set of 21 low pass filters of which a selection is shown in Fig. (B.4). These filters were designed by use of an truncated ideal low pass combined with a Chebyshev window as described in Ref. [54] and result in the coefficients of Fig. (B.7). This method is favorable because it gives a good compromise between a high suppression of the unwanted components and a low distortion of the signal of interest.

Since the filtering involves multiplications and summations, one has to assure that the range of the fixed point output is not exceeded. This bit growth effect is characterized by the quantity $A_{max} = \sum_l |c_l|^2$ which is proportional to the worst case output of the filter. To avoid this effect all filters are normalized such that $A_{max} = 1$ so that even in the worst case the output will stay inside the range of the input. The output width of the filter is `Fix_18_17` where we tried to keep a high precision to avoid numerical noise from multiple rounding.

In many cases one can assume that the amplitude of the filtered signal will stay well below the worst case. In fact $A_{max} = 1$ is a conservative choice in particular when the input is dominated

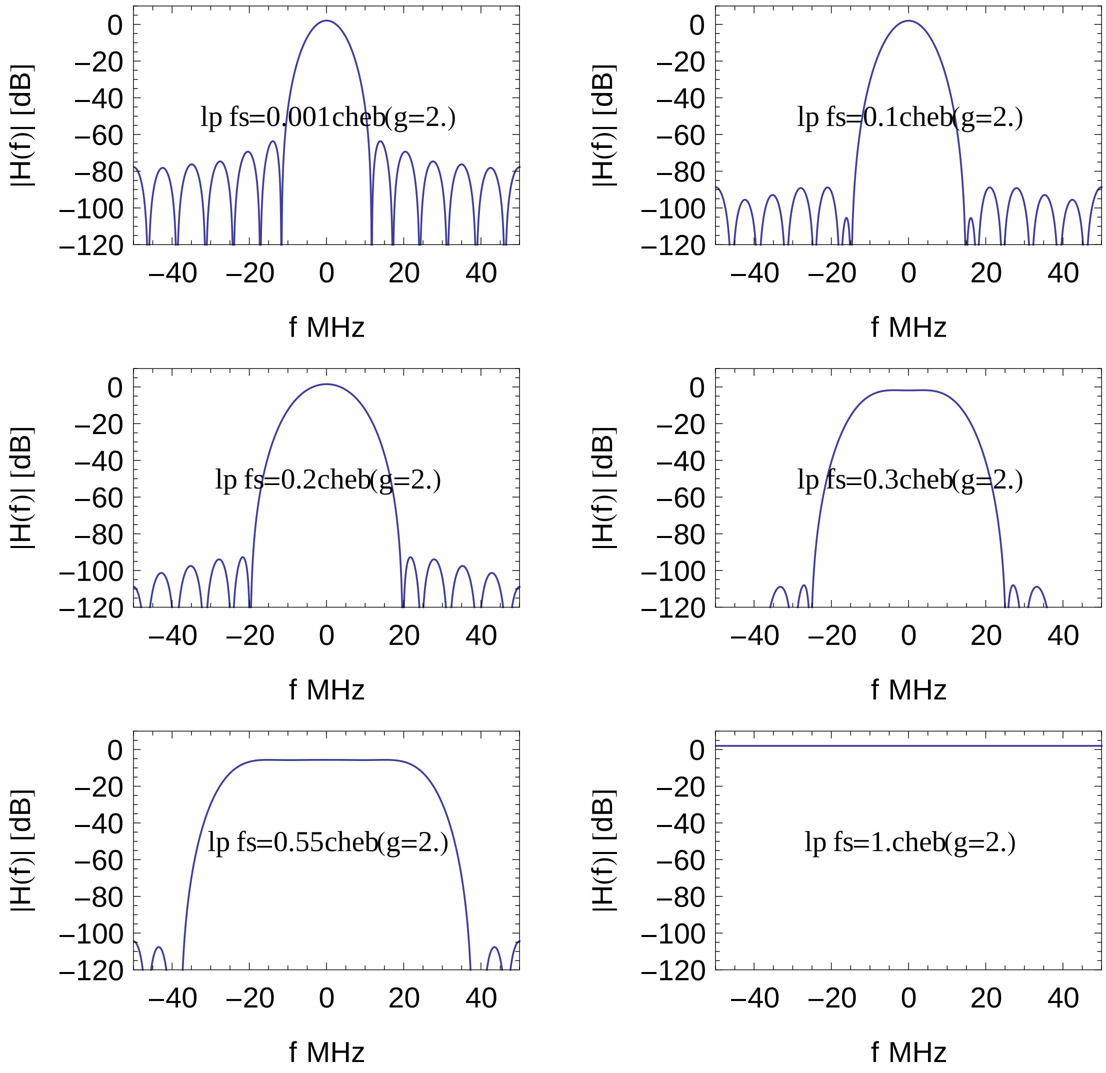

Figure B.4.: Transfer characteristics of different low pass filters which were designed for our experiments.

by random noise. Then the option `filterGain` can be used to scale up the filter coefficients in the software to increase the amplitude of the filtered signal. This helps to retain more significant bits and increasing the numerical accuracy of the subsequent stages, at the cost of a possible violation of the numeric range of the filter (clipping). A `filterGain` of 5 for the filters with $f_s \leq 0.25$ has proven as a good choice.

B.1.4. Signal Maths

Following the filtering stage one has the option to apply a mathematical transformation on the signals (schematic in Fig. (B.5), implementation in Fig. (B.9)). This transformation allows to multiply parts of the incoming signals and strip either the real or imaginary part for the further processing. Note that this transformation goes sample by sample, i.e. no time shifts or other more complicated transformations can be applied at this point. The two output signals of this

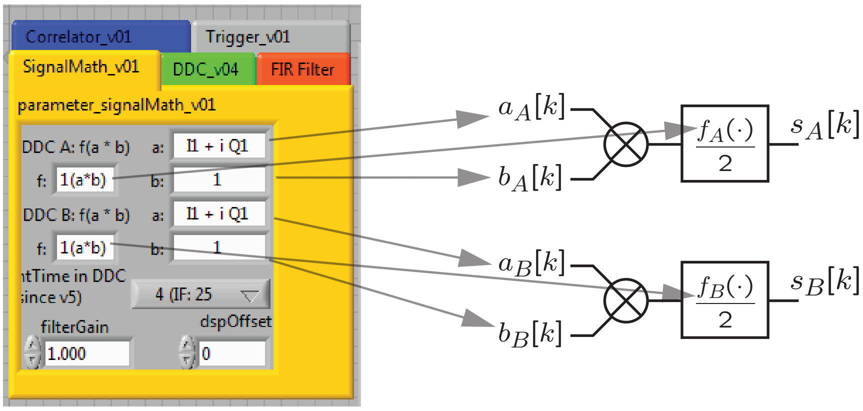

DDC A: f(a * b) a: I1 + i Q1
f: 1(a*b) b: 1
DDC B: f(a * b) a: I1 + i Q1
f: 1(a*b) b: 1
ıtTime in DDC ;ince v5) 4 (IF: 25
filterGain 1.000
dspOffset 0

Figure B.5.: Schematic of the parametrization and implementation of the mathematical transformations which can be applied on the input signals.

stage s_A, s_B are formally described by

$$s_A[k] = \frac{f_A(a_A[k]b_A[k])}{2} \quad \text{and} \quad s_B[k] = \frac{f_B(a_B[k]b_B[k])}{2}, \tag{B.14}$$

where the expressions on the r.h.s. indexed by A, B are two sets of parameters which can be chosen from

$$f_A, f_B \in \{\mathbb{1}, \mathrm{Re}, \mathrm{Im}\} \tag{B.15}$$

$$a_A, b_A, a_B, b_B \in \{1, s_1, s_2, s_1^*, s_2^*\}. \tag{B.16}$$

This allows for example to obtain the instantaneous power of channel 1 choosing

$$f_A = \mathbb{1}, a_A = s_1, b_A = s_1^* \quad \Rightarrow \quad s_A[n] = s_1^*[n]s_1[n], \tag{B.17}$$

or the cross-power between channel 1 and 2 as

$$f_A = \mathbb{1}, a_A = s_1, b_A = s_2^* \quad \Rightarrow \quad s_A[n] = s_2^*[n]s_1[n]. \tag{B.18}$$

B.1.5. Decimation, windowing and zeropadding

To facilitate the calculation of correlations we now apply three further transformations on the signals s_A, s_B. First we can choose to decimate the signals by a factor given as `dfactor`, where only every `dfactor`-th sample is kept and all samples in between are discarded. This is useful to get rid of redundant information when the bandwidth of the signal was sufficiently reduced by the filtering stage (implementation in Fig. (B.10b)).

From the decimated signal 2048 points are then put together to a *window*, which starts at the rising edge of the measurement trigger. These windows will be written as complex vectors $\mathbf{s}_\mathrm{A}, \mathbf{s}_\mathrm{B}$ of length 2048. The duration captured by one window is `dfactor` $\cdot\, 2048 \cdot 10\,\mathrm{ns}$ due to the fixed number of points. The smallest window is $20.48\mu\mathrm{s}$ long for `dfactor` $= 1$.

With the `zeropadding` option we can finally choose to set the second half of these vectors to 0 (implementation in Fig. (B.10c)). This option can be used in connection with the following correlator stage to choose between cyclic and non-cyclic convolutions. The k-th element of the output vectors is given by

$$(\mathbf{s}_{\mathrm{A,B}})_k = \begin{cases} s_{A,B}[dfactor \cdot k] \\ 0 \qquad i \geq 1024 \quad \text{and } \texttt{zeropadding} \text{ enabled} \end{cases} . \tag{B.19}$$

B.1.6. Calculating correlations and averaging

In the last stage of the chain the *cyclic correlation* between the vectors $\mathbf{s}_A$ and $\mathbf{s}_B$ is calculated. The regular correlation between two complex time-discrete signals $a[n]$, $b[n]$ is given by

$$G_{\mathrm{reg}}[\tau] = \sum_{l=-\infty}^{\infty} a[l]b^*[l+\tau]. \tag{B.20}$$

If we assume that these signals are periodic with a period of N and that samples with a time distance larger than $N-1$ are uncorrelated this is equivalent to the cyclic correlation given by

$$G_{\mathrm{cyc}}[\tau] = \sum_{l=0}^{N-1} a[l]b^*[l+\tau \mod N]. \tag{B.21}$$

The condition is in fact unnecessary when applying zeropadding such that the second half of the signal is set to 0. In this case the cyclic convolution is similar to the regular convolution for a finite signal up to a normalization procedure.

It is useful to calculate the cyclic convolution in hardware because it can be implemented in an algorithm based on the discrete Fourier transform (DFT). This transform is very efficient in binary hardware through the fast Fourier transform (FFT) algorithm and is widely established in signal processing applications. To see how the DFT can be used to calculate correlations we note a correlation can be equivalently written as a convolution

$$\begin{aligned} G[-\tau] &= \sum_l a[l]b^*[l-\tau] \\ &= \sum_l a[l]b^*[-(\tau-l)] = (a[l] * b^*[-l])[\tau]. \end{aligned} \tag{B.22}$$

This is true for regular and cyclic correlation with the respective regular and cyclic convolution. By the convolution theorem of the Fourier transform this operation can be expressed in terms of the DFT and the inverse DFT (IDFT) as

$$\begin{aligned} (a[l] *_{\mathrm{cyc}} b[l])[\tau] &= \sum_{l=0}^{N-1} a[l]b[\tau-l] \\ &= \mathrm{IDFT}(\mathrm{DFT}(a[l]) \cdot \mathrm{DFT}(b[n])). \end{aligned} \tag{B.23}$$

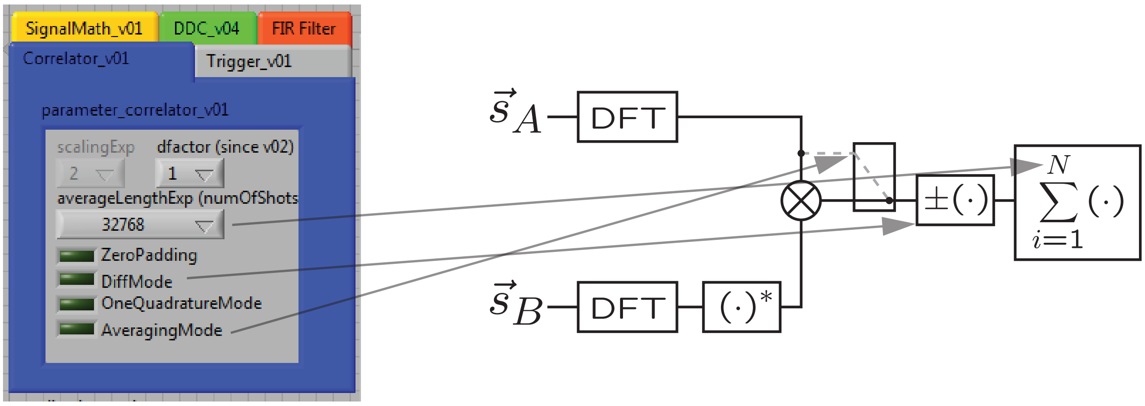

scalingExp 2
dfactor (since v02) 1
averageLengthExp (numOfShots 32768
ZeroPadding
DiffMode
OneQuadratureMode
AveragingMode

Figure B.6.: Schematic of the parametrization and implementation of the mathematical transformations which can be applied on the input signals.

To find the equivalent formula for the correlation one needs to conjugate and time reverse the signal *b*. Most easily this is achieved in the frequency domain by *conjugating the DFT of b* because .

$$\mathrm{DFT}(\mathbf{b}^*[-\mathbf{l}]) = \mathrm{DFT}(\mathbf{b}[\mathbf{l}])^*. \tag{B.24}$$

The frequency domain algorithm by which we compute the cyclic correlation of $\mathbf{s}_A, \mathbf{s}_B$ is then

$$\begin{aligned} G_{s_A,s_B}[-\tau] &= \sum_{l=0}^{2047} (\mathbf{s}_\mathrm{A})_l (\mathbf{s}_\mathrm{B})^*_{l+\tau} \\ &= \mathrm{IDFT}(\mathrm{DFT}(\mathbf{s}_\mathrm{A}) \cdot \mathrm{DFT}(\mathbf{s}_\mathrm{B})^*). \end{aligned} \tag{B.25}$$

The schematics for this algorithm is shown in Fig. (B.6) and its implementation in Fig. (B.11). The result the correlator state is finally summed up over a number of repetitions of experiments specified by `averageLengthExp`. One can note that the inverse DFT is missing in this implementation. Since both averaging and the inverse DFT are both linear operations it is possible to swap them. The IDFT is performed after the experiment in the data analysis software by which a significant amount of hardware resources on the FPGA device can be saved.

The DFT is the most expensive operation which is currently performed in the hardware and is implemented as a FFT. To achieve high numerical precision we chose as input data type `Fix_17_16` and a *phase factor* of 16 bit for the internal phase memory of the FFT implementation. During the FFT the required numerical range can increase significantly which leads to an output data type of `Fix_54_28`.

Two options apart from the number of averages allow to change the behavior of this stage. If the option `AveragingMode` is chosen, only the spectrum of $\mathbf{s}_A$ is averaged. In this mode no correlation is calculated and $\mathbf{s}_B$ is discarded. When option `DiffMode` is turned on the averager will sum up the differences between two subsequent measurement results. To achieve this, the sign of the signal is toggled for each repetition. This allows e.g. to subtract a reference measurement to get rid of unwanted background signals.

The averaging step is not very resource intensive and can retain the full precision of the FFT output (implementation in Fig. (B.10a)). During the summation of up to $2^{32} \approx 4 \times 10^9$ repetitions the range of the data grows by another 32 bit so that we used a `CFix_96_31` data type for the averaging. This data type is useful for our purposes by providing an enormous dynamic range[1] of 10^{28} capturing even tiny signals on large backgrounds without numerical loss.

B.1.7. Read-out

When the specified number of averages was taken the result is written to the on-board memory of the FPGA board. This is only done after all repetitions were performed, so no intermediate result can be extracted in the current implementation. The measurement software *Cleansweep* reads out the memory, applies a IDFT to the summed data and divides the result by the number of averages taken. The data is available as *channel 3* in the software and is saved together with the data of the other acquisition card in a text file format.

B.2. Examples

To perform the experiments presented in Sec. 5 we use the following settings through out the measurements

Sampling:	`ADC1`, `ADC2`
Mixing:	`25MHz phase adjust`, `phase=0`
Filtering:	low pass filter with `fs`=0.2
Signal Maths:	$f_A = f_B = \mathbb{1}$
All other options off	

Quadrature measurements

To perform average quadrature measurements, like $\langle S_b(t) \rangle$ we chose the following options

Signal maths:	$a_A = s_1, b_A = 1$ and $a_B = 1, b_B = 1$
Correlator:	`AveragingMode` on and e.g. 1M `averageLength`

Power measurements

To perform average power measurements, like $\left\langle S_b^*(t) S_b(t) \right\rangle$ we chose the following options

Signal maths:	$a_A = s_1^*, b_A = s_1$ and $a_B = 1, b_B = 1$
Correlator:	`AveragingMode` on and e.g. 1M `averageLength`

---

[1] here defined as largest possible number divided by smallest increment.

For cross-power measurements $b_A = s_2$ can be chosen where $\left\langle S_b^*(t) S_c(t) \right\rangle$ is measured.

First-order correlation function

To perform first-order auto-correlation measurements, like $\int \left\langle S_b^*(t) S_b(t+\tau) \right\rangle dt$ we chose the following options

Signal maths:	$a_A = s_1, b_A = 1$ and $a_B = s_1, b_B = 1$
Correlator:	`AveragingMode` off, `DiffMode` on and e.g. 32M `averageLength`

Note in particular that a_B is not complex conjugated as one might expect. This is due to the algorithm which performs the complex conjugation internally. Again the cross-correlation can be measured by choosing $a_B = s_2$.

Note that to use `DiffMode` on, in every second repetition of the experiment the source/state preparation has to be turned off!

Second-order correlation function

To perform a second-order auto-correlation measurements, like

$$\Gamma^{(2A)}(\tau) = \int \langle S_b^*(t) S_b(t) S_c^*(t+\tau) S_c(t+\tau) \rangle \, dt$$

we chose the following options

Signal maths:	$a_A = s_1, b_A = s_1^*$ and $a_B = s_2, b_B = s_2^*$
Correlator:	`AveragingMode` off, `DiffMode` on and e.g. 256M `averageLength`

Note that to use `DiffMode` on, in every second repetition of the experiment the source/state preparation has to be turned off!

```
[FilterLibrary]
filters.<size(s)>= 21
filters 0. FilterName = lp fs = 0.001 cheb (g = 2.)
filters 0. Coefficients = "<size(s)=7> 0.12207 0.117188 0.104492 0.0859375 0.0644531 0.0429688 0.0253906"
filters 1. FilterName = lp fs = 0.05 cheb (g = 2.)
filters 1. Coefficients = "<size(s)=7> 0.125977 0.121094 0.106445 0.0849609 0.0625 0.0400391 0.0224609"
filters 2. FilterName = lp fs = 0.1 cheb (g = 2.)
filters 2. Coefficients = "<size(s)=7> 0.139648 0.131836 0.112305 0.0839844 0.0556641 0.03125 0.0146484"
filters 3. FilterName = lp fs = 0.15 cheb (g = 2.)
filters 3. Coefficients = "<size(s)=7> 0.164063 0.152344 0.121094 0.0810547 0.0439453 0.0175781 0.00390625"
filters 4. FilterName = lp fs = 0.2 cheb (g = 2.)
filters 4. Coefficients = "<size(s)=7> 0.195313 0.175781 0.126953 0.0693359 0.0244141 0 -0.00585938"
filters 5. FilterName = lp fs = 0.25 cheb (g = 2.)
filters 5. Coefficients = "<size(s)=7> 0.223633 0.194336 0.12207 0.046875 0 -0.0146484 -0.00976563"
filters 6. FilterName = lp fs = 0.3 cheb (g = 2.)
filters 6. Coefficients = "<size(s)=7> 0.248047 0.205078 0.107422 0.0195313 -0.0205078 -0.0185547 -0.00488281"
filters 7. FilterName = lp fs = 0.35 cheb (g = 2.)
filters 7. Coefficients = "<size(s)=7> 0.27832 0.216797 0.0878906 -0.00976563 -0.03125 -0.0126953 0.00292969"
filters 8. FilterName = lp fs = 0.4 cheb (g = 2.)
filters 8. Coefficients = "<size(s)=7> 0.300781 0.21875 0.0605469 -0.0332031 -0.0302734 0 0.0078125"
filters 9. FilterName = lp fs = 0.45 cheb (g = 2.)
filters 9. Coefficients = "<size(s)=7> 0.328125 0.220703 0.0302734 -0.0488281 -0.0175781 0.0117188 0.00683594"
filters 10. FilterName = lp fs = 0.5 cheb (g = 2.)
filters 10. Coefficients = "<size(s)=7> 0.382813 0.234375 0 -0.0566406 0 0.0175781 0"
filters 11. FilterName = lp fs = 0.55 cheb (g = 2.)
filters 11. Coefficients = "<size(s)=7> 0.374023 0.206055 -0.0283203 -0.0449219 0.0166016 0.0107422 -0.00585938"
filters 12. FilterName = lp fs = 0.6 cheb (g = 2.)
filters 12. Coefficients = "<size(s)=7> 0.391602 0.19043 -0.0527344 -0.0283203 0.0263672 0 -0.00683594"
filters 13. FilterName = lp fs = 0.65 cheb (g = 2.)
filters 13. Coefficients = "<size(s)=7> 0.416992 0.174805 -0.0712891 -0.0078125 0.0253906 -0.00976563 -0.00195313"
filters 14. FilterName = lp fs = 0.7 cheb (g = 2.)
filters 14. Coefficients = "<size(s)=7> 0.435547 0.154297 -0.0810547 0.0146484 0.015625 -0.0136719 0.00390625"
filters 15. FilterName = lp fs = 0.75 cheb (g = 2.)
filters 15. Coefficients = "<size(s)=7> 0.463867 0.133789 -0.0849609 0.0322266 0 -0.00976563 0.00683594"
filters 16. FilterName = lp fs = 0.8 cheb (g = 2.)
filters 16. Coefficients = "<size(s)=7> 0.492188 0.111328 -0.0800781 0.0439453 -0.015625 0 0.00390625"
filters 17. FilterName = lp fs = 0.85 cheb (g = 2.)
filters 17. Coefficients = "<size(s)=7> 0.526367 0.0859375 -0.0683594 0.0458984 -0.0244141 0.00976563 -0.00195313"
filters 18. FilterName = lp fs = 0.9 cheb (g = 2.)
filters 18. Coefficients = "<size(s)=7> 0.59375 0.0625 -0.0527344 0.0400391 -0.0263672 0.0146484 -0.00683594"
filters 19. FilterName = lp fs = 0.95 cheb (g = 2.)
filters 19. Coefficients = "<size(s)=7> 0.732422 0.0371094 -0.0322266 0.0263672 -0.0185547 0.0126953 -0.00683594"
filters 20. FilterName = lp fs = 1. cheb (g = 2.)
filters 20. Coefficients = "<size(s)=7> 1. 0 0 0 0 0 0"
```

Figure B.7.: Coefficients for a family of low pass filters.

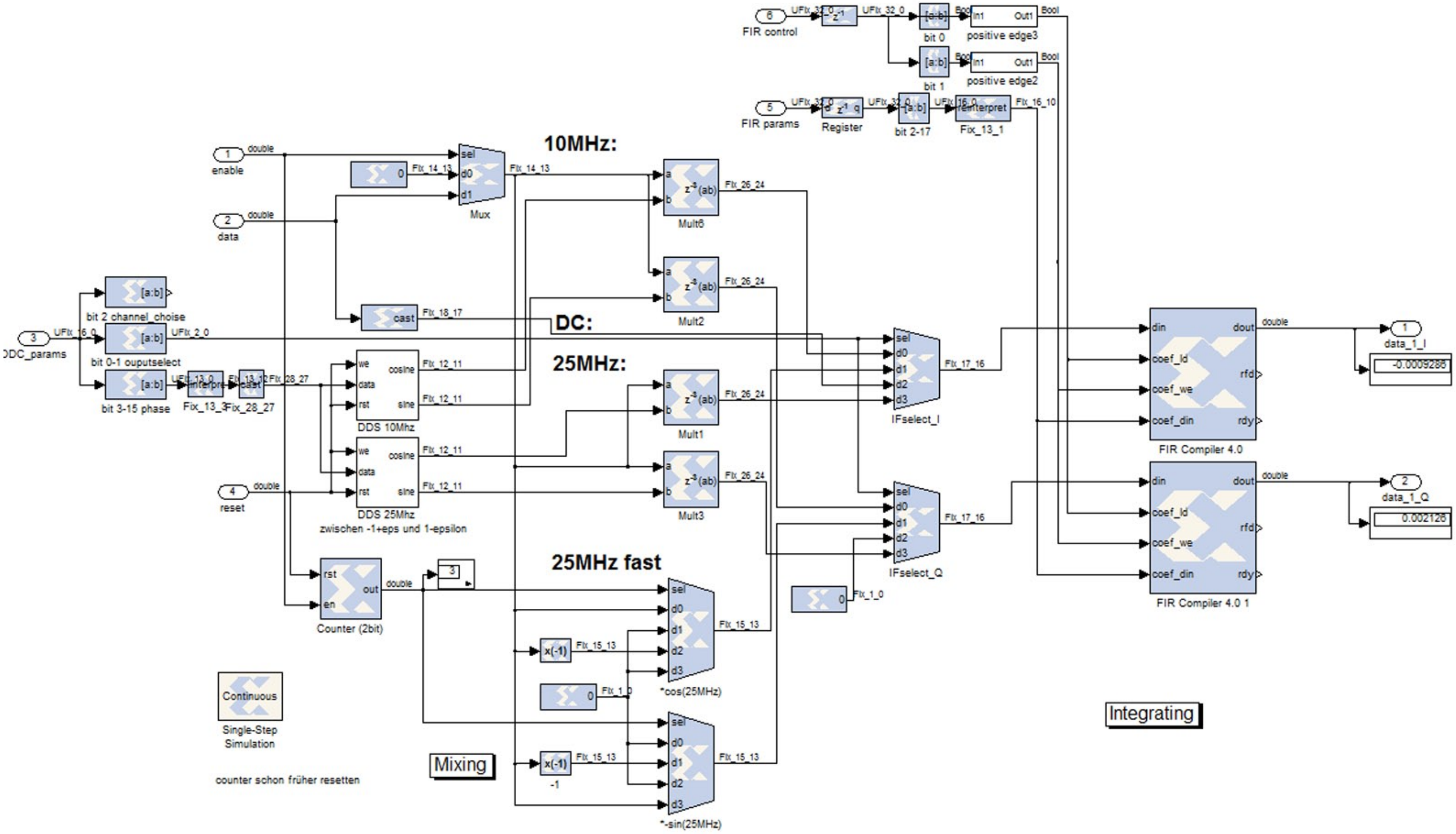

Figure B.8.: Schematics of the digital down conversion implementation in the FPGA design including mixing and filtering stage. This stage is implemented once for each channel.

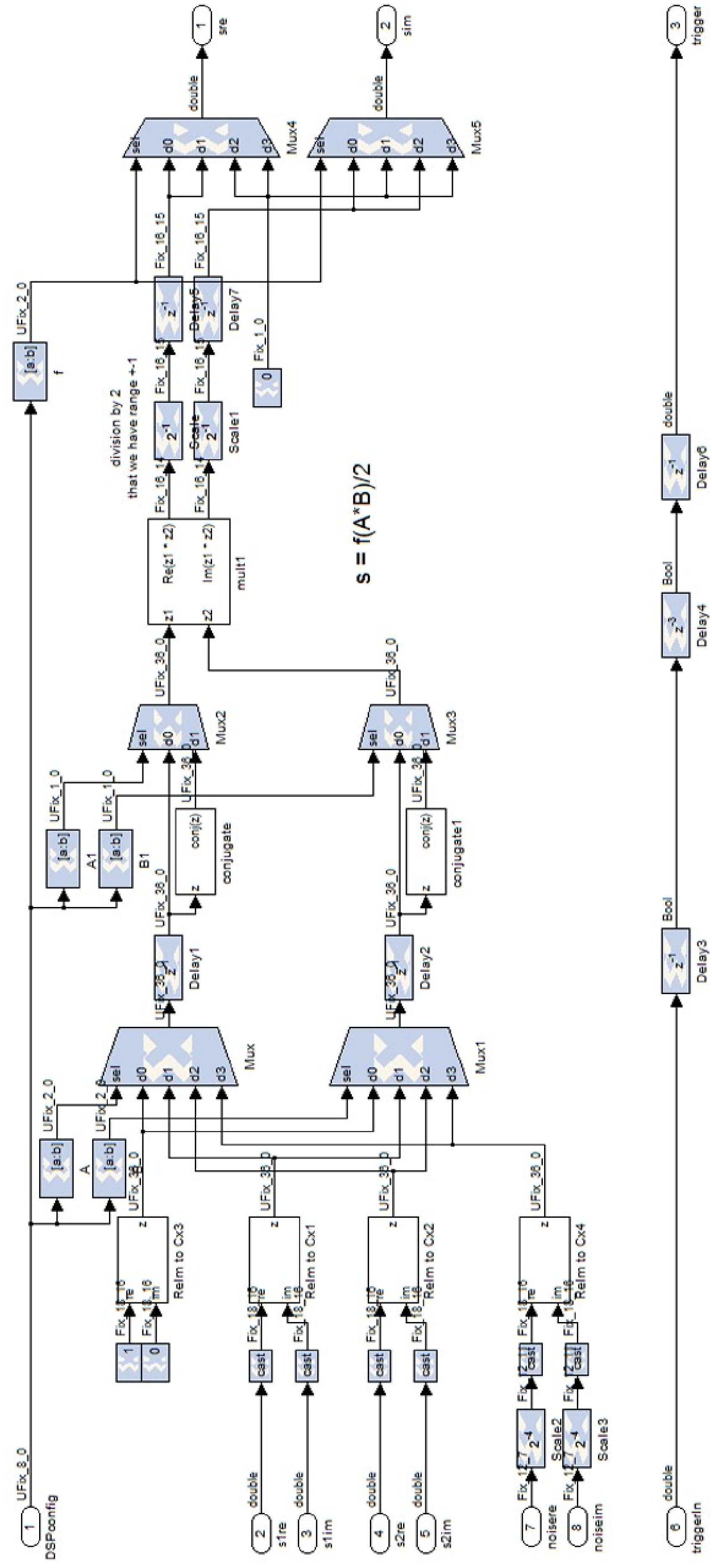

Figure B.9.: Schematics of the signal math stage. This stage is implemented twice to provide two different input signal to the correlator stage.

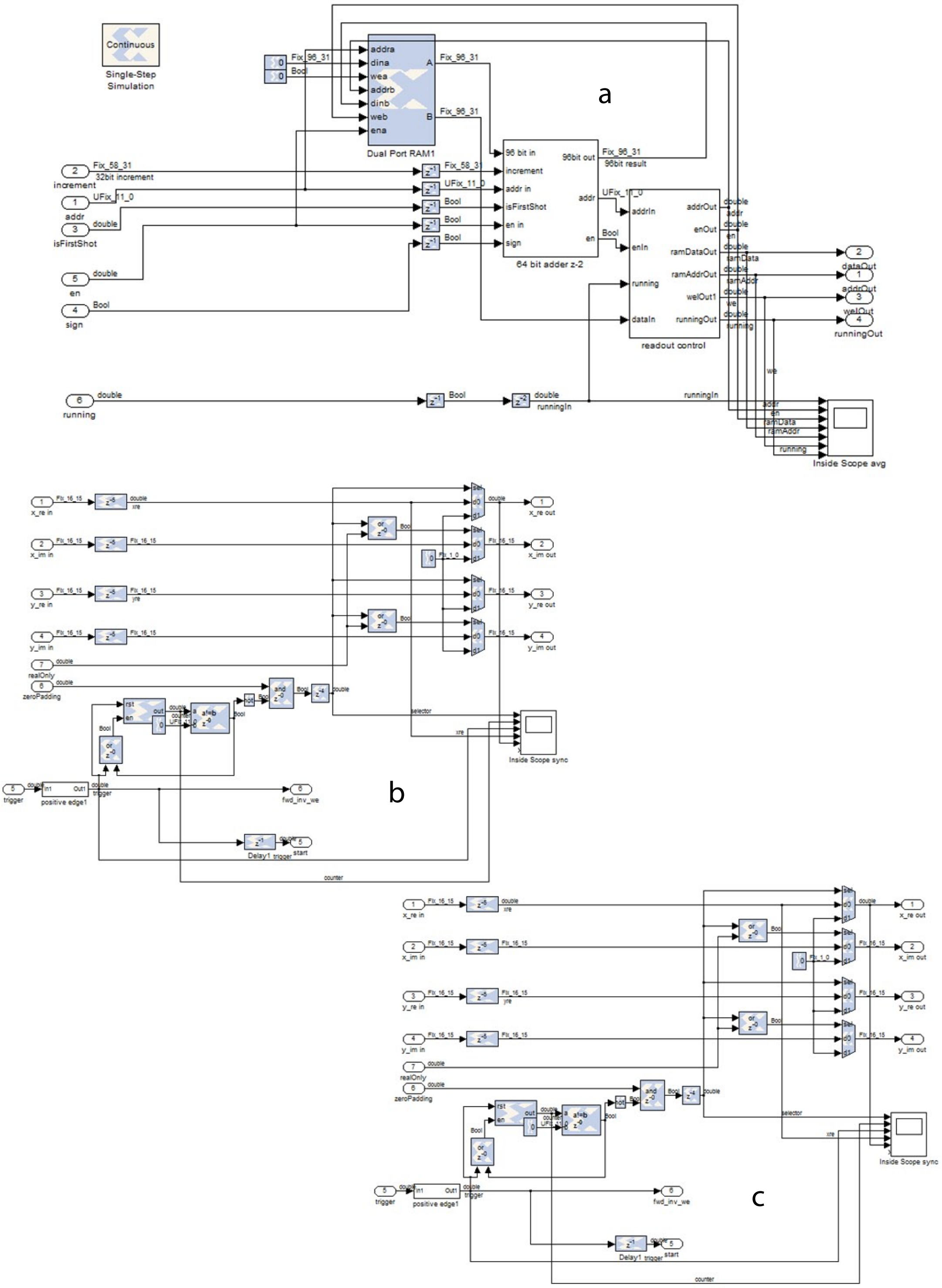

Figure B.10.: **a**) Schematics of the averaging stage. This stage is implemented individually for the real and the imaginary part of the measurement signal. **b**) Schematics of the decimation stage. **c**) Schematics of the zeropadding stage.

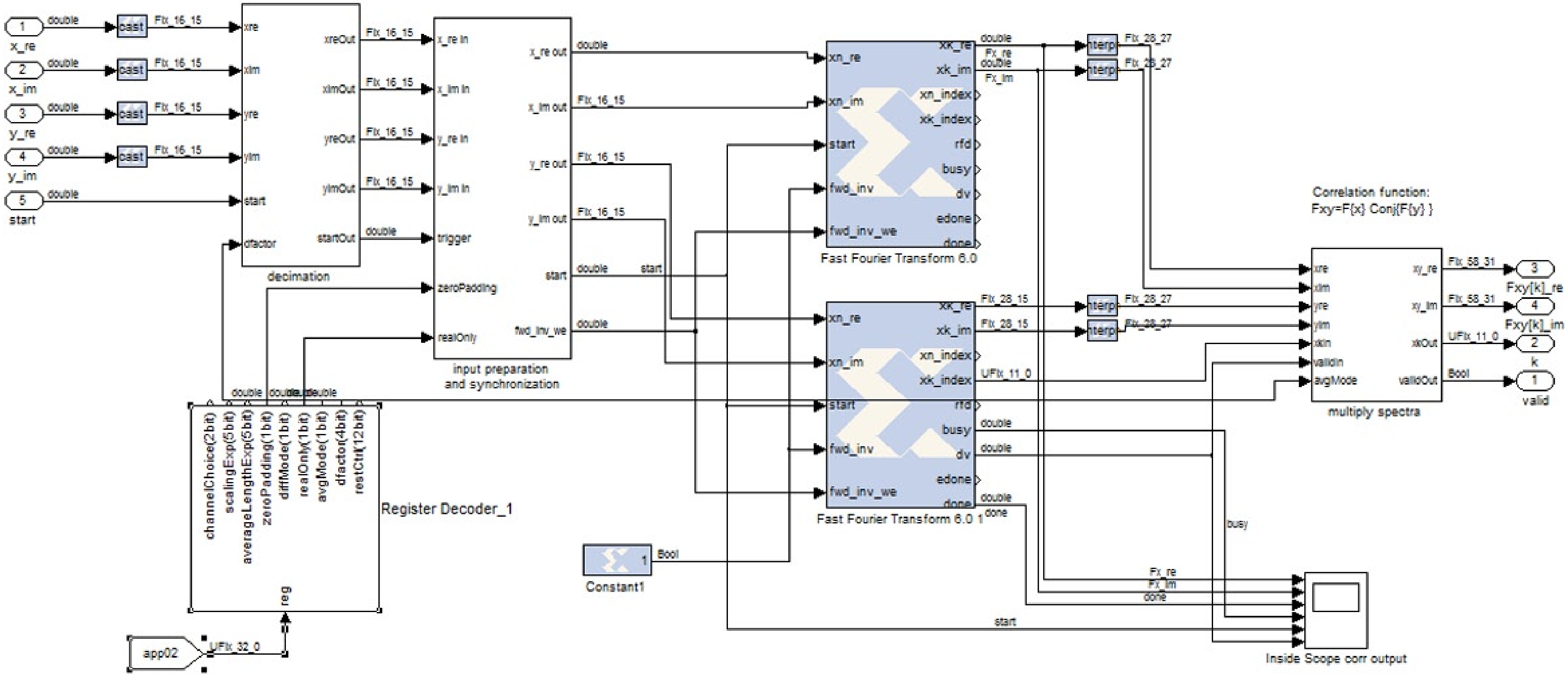

Figure B.11.: Schematics of the correlator stage. After decimation and zeropadding both signals are Fourier transformed and then multiplied. The output of this stage goes to the averaging stage.

C. Further Calculations

In this appendix we present additional calculations which are useful to understand the mathematical background of the theoretical part.

C.1. Useful simplifications

For the derivation of equations for the measurement of the first- and second-order correlation functions we show how general expressions of correlations in the measurement data can be simplified. For two detection channels the most general correlation we can measure is given by

$$\Gamma = \left\langle \left(\hat{S}_b^\dagger\right)^m \left(\hat{S}_c^\dagger\right)^n \left(\hat{S}_b\right)^l \left(\hat{S}_c\right)^p \right\rangle . \tag{C.1}$$

The ordering of the operators in this expression is arbitrary because all operators commute. The above ordering will be useful though to derive measurements of correlations of *normally ordered cavity operators*. Our first simplification comes from the fact that in this ordering all input mode operators $b_{\text{in}}, c_{\text{in}}$ are normally ordered and therefore as shown in Eq. (C.39) have vanishing expectation values, therefore

$$\begin{aligned}\Gamma =& g_b^{(m+l)} g_c^{(n+p)} \\ & \langle \left(\sqrt{\kappa_b} a^\dagger + n_b\right)^m \left(\sqrt{\kappa_c} a^\dagger + n_c\right)^n \\ & \left(\sqrt{\kappa_b} a + n_b^\dagger\right)^l \left(\sqrt{\kappa_c} a + n_c^\dagger\right)^p \rangle .\end{aligned} \tag{C.2}$$

Furthermore if any of $m, n, l, p = 0$ a similar argument is applicable for the noise operators. Assume $l = 0$ then all appearances of the operator n_b are vanishing, since this mode is assumed uncorrelated with all other modes and no $n_b^\dagger$ appears. This means all occurrences of n_b can be replaced by 0. For $m = 0$ or $l = 0$:

$$\begin{aligned}\Gamma = g_b^{(m+l)} g_c^{(n+p)} \langle \left(\sqrt{\kappa_b} a^\dagger\right)^m \left(\sqrt{\kappa_c} a^\dagger + n_c\right)^n \\ \left(\sqrt{\kappa_b} a\right)^l \left(\sqrt{\kappa_c} a + n_c^\dagger\right)^p \rangle .\end{aligned} \tag{C.3}$$

For $n = 0$ or $p = 0$:

$$\begin{aligned}\Gamma = g_b^{(m+l)} g_c^{(n+p)} \langle \left(\sqrt{\kappa_b} a^\dagger + n_b\right)^m \left(\sqrt{\kappa_c} a^\dagger\right)^n \\ \left(\sqrt{\kappa_b} a + n_b^\dagger\right)^l \left(\sqrt{\kappa_c} a\right)^p \rangle .\end{aligned} \tag{C.4}$$

C.2. Computing correlation functions of $a(t)$

The usual statement of the quantum regression theorem is that, given

$$\frac{d}{dt}\langle B(t)\rangle = \sum_i m_i \langle B_i(t)\rangle, \tag{C.5}$$

for some set of operators $B_i(t)$ and coefficients m_i, it follows that [43]

$$\frac{d}{d\tau}\langle A(t)B(t+\tau)C(t)\rangle = \sum_i m_i \langle A(t)B_i(t+\tau)C(t)\rangle. \tag{C.6}$$

In order to compute correlation functions, it is necessary to compute the derivatives of the correlation functions $\langle a(t)a(t)\rangle$, $\langle a^\dagger(t)a(t)\rangle$, $\langle a(t)a^\dagger(t)\rangle$ and $\langle a^\dagger(t)a^\dagger(t)\rangle$, as these can be used to compute the four operator correlations which appear in expressions related to $G^{(2)}$.

Using the equation of motion for $a(t)$, and the chain rule, these can be evaluated directly. In particular, by taking the input modes to be in the vacuum state, we find

$$\frac{d}{dt}\langle a(t)a(t)\rangle = -\kappa\langle a(t)a(t)\rangle, \tag{C.7}$$

$$\frac{d}{dt}\langle a^\dagger(t)a(t)\rangle = -\kappa\langle a^\dagger(t)a(t)\rangle, \tag{C.8}$$

$$\frac{d}{dt}\langle a(t)a^\dagger(t)\rangle = -\kappa\langle a(t)a^\dagger(t)\rangle, \tag{C.9}$$

$$\frac{d}{dt}\langle a^\dagger(t)a^\dagger(t)\rangle = -\kappa\langle a^\dagger(t)a^\dagger(t)\rangle. \tag{C.10}$$

It then follows that, for example,

$$\frac{d}{d\tau}\langle a^\dagger(t)a^\dagger(t+\tau)a(t+\tau)a(t)\rangle = -\kappa\langle a^\dagger(t)a^\dagger(t+\tau)a(t+\tau)a(t)\rangle \tag{C.11}$$

and thus

$$\langle a^\dagger(t)a^\dagger(t+\tau)a(t+\tau)a(t)\rangle = e^{-\kappa\tau}\langle a^\dagger a^\dagger aa(t)\rangle. \tag{C.12}$$

Using the equations of motion once again to compute the derivative of the right-hand side, after integration we finally obtain

$$\langle a^\dagger(t)a^\dagger(t+\tau)a(t+\tau)a(t)\rangle = e^{-\kappa(2t+\tau)}\langle a^\dagger a^\dagger aa(0)\rangle. \tag{C.13}$$

C.3. Filtered signals

To see the effect of filtering on the measured signals we will introduce a general framework which describes what happens to multi-time multi-channel correlations when filters are applied. Assume a system with n channels where each channel is filtered individually. One can write the filtered outcome of each channel $\tilde{s}_i$ in terms of the input signal s_i and the filter function

f_i using the relation for linear time-invariant systems

$$\begin{aligned}\tilde{s}_i(t_i) &= f_i(t_i) * s_i(t_i) \\ &= \int_{-\infty}^{\infty} f_i(\tau_i) s_i(t_i - \tau_i) d\tau_i.\end{aligned} \tag{C.14}$$

Note that we introduce a time t_i for each channel individualy to capture the case of multi-time correlations. This also clearifies with respect to which variable the convolution is done. The goal is now to express the filtered correlation function

$$\tilde{G}(t_1, \dots, t_n) = \tilde{s}_1(t_1) \cdot \tilde{s}_2(t_2) \cdots \tilde{s}_n(t_n) \tag{C.15}$$

in terms of the unfiltered correlation function

$$G(t_1, \dots, t_n) = s_1(t_1) \cdot s_2(t_2) \cdots s_n(t_n). \tag{C.16}$$

This can be done straight forward by substituting Eq. (C.14) into Eq. (C.15).

$$\tilde{G}(t_1, \dots, t_n) = \prod_{i=1}^{n} (f_i(t_i) * s_i(t_i)) \tag{C.17}$$

Realizing that all convolutions are related to different time variables one can rearrange this expression as

$$\tilde{G}(t_1, \dots, t_n) = f_1(t_1) * (f_2(t_2) * (\cdots (f_n(t_n) * G(t_1, \dots, t_n)) \cdots)). \tag{C.18}$$

The integral form clarifies this expression

$$\tilde{G}(t_1, \dots, t_n) = \int \cdots \int f_1(t_1 - \tau_1) \cdots f_n(t_n - \tau_n) G(\tau_1, \dots, \tau_n) d\tau_1 \cdots d\tau_n. \tag{C.19}$$

This expression can be seen as a generalized convolution with respect to more then one time dimension. Introducing a global filter function

$$F(t_1, \dots, t_n) = f_1(t_1) \cdot f_2(t_2) \cdots f_n(t_n), \tag{C.20}$$

one can write

$$\tilde{G}(t_1, \dots, t_n) = F(t_1, \dots, t_n) * G(t_1, \dots, t_n). \tag{C.21}$$

In the Fourier domain the same fact can be expressed by using the multi-dimensional Fourier transform instead of the one-dimensional one. We can simply write now

$$\tilde{G}(\omega_1, \dots, \omega_n) = G(\omega_1, \dots, \omega_n) F(\omega_1, \dots, \omega_n). \tag{C.22}$$

First-order correlation function

Using the spectral representation of some first order correlation function $G(t_1, t_2)$ and the global filter function $F(t_1, t_2)$, we can write $\tilde{G}(\tau)$ as

$$\tilde{G}(\tau) = \iiint dt d\omega_1 d\omega_2 \; e^{i(\omega_1+\omega_2)t+i\omega_2\tau} F(\omega_1, \omega_2) G(\omega_1, \omega_2), \tag{C.23}$$

$$= \frac{1}{2\pi} \int d\omega e^{i\omega\tau} F(-\omega, \omega) G(-\omega, \omega). \tag{C.24}$$

If we consider the time representation of this expression, it is clear that the correlation function will be distorted by a convolution with $f_{\text{eff}}(\tau) = \mathcal{F}\{F(-\omega, \omega)/2\pi\}$. In other words,

$$\tilde{\Gamma}^{(1)}(\tau) = g^2\kappa \tilde{G}^{(1)}(\tau) + \tilde{G}_{bc}(\tau) \tag{C.25}$$

$$= g^2\kappa f_{\text{eff}}(\tau) * G^{(1)}(\tau) + f_{\text{eff}}(\tau) * G_{bc}(\tau). \tag{C.26}$$

Note that since we are assuming a linear time independent filter, the relative heights of the peaks remain unchanged – only their shape gets distorted. This distortion is illustrated in Fig. 4.5.

Second-order correlation functions

If we consider second-order correlations with filtered signals, we obtain

$$\tilde{G}(\tau) = \int\limits_{\mathbb{R}^5} dt d\omega^4 e^{i(\omega_1+\omega_2+\omega_3+\omega_4)t} e^{i(\omega_2+\omega_4)\tau} F(\omega_1, \omega_2, \omega_3, \omega_4) G(\omega_1, \omega_2, \omega_3, \omega_4). \tag{C.27}$$

The different types of second-order correlations discussed simply determine the labeling of the variables. Applying the change of variables

$$\omega_1 + \omega_2 + \omega_3 + \omega_4 = k_1, \quad \omega_1 - \omega_2 + \omega_3 - \omega_4 = k_2, \tag{C.28}$$

$$\omega_1 + \omega_2 - \omega_3 - \omega_4 = k_3, \quad \omega_1 - \omega_2 - \omega_3 + \omega_4 = k_4, \tag{C.29}$$

and integrating over time, one obtains

$$\begin{aligned}\tilde{G}(\tau) = \frac{1}{32\pi} \int_{-\infty}^{\infty} dk_2 e^{-ik_2\tau/2} \int_{-\infty}^{\infty}\int_{-\infty}^{\infty} dk_3 dk_4 \\ F\left(\frac{k_2+k_3+k_4}{4}, \frac{-k_2+k_3-k_4}{4}, \frac{k_2-k_3-k_4}{4}, \frac{-k_2-k_3-k_4}{4}\right) \\ G\left(\frac{k_2+k_3+k_4}{4}, \frac{-k_2+k_3-k_4}{4}, \frac{k_2-k_3-k_4}{4}, \frac{-k_2-k_3+k_4}{4}\right),\end{aligned} \tag{C.30}$$

and after another change of variables, one obtains

$$
\begin{aligned}
\tilde{G}(\tau) = \frac{1}{64\pi}\int_{-\infty}^{\infty} dke^{-ik\tau/2}\int_{-\infty}^{\infty}\int_{-\infty}^{\infty} dxdy \\
F\left(\frac{k+x}{4}, \frac{-k+y}{4}, \frac{k-x}{4}, \frac{-k-y}{4}\right) \\
G\left(\frac{k+x}{4}, \frac{-k+y}{4}, \frac{k-x}{4}, \frac{-k-y}{4}\right),
\end{aligned}
\tag{C.31}
$$

The main difficulty in this calculation is that it appears to be necessary to know what $\langle a^\dagger(t_1)a^\dagger(t_2)a(t_3)a(t_4)\rangle$ is, while so far we have only calculated $\langle a^\dagger(t)a^\dagger(t+\tau)a(t+\tau)a(t)\rangle$.

C.4. Commutation relation of cavity output modes

We want to check whether the operators of the two output modes b_{out} and c_{out} commute, so that their quadratures may be measured simultaneously. For this, we use the boundary conditions Eq. (4.23):

$$
\begin{aligned}
[b_{\text{out}}(t), c^\dagger_{\text{out}}(t')] &= [\sqrt{\kappa_b}a(t) - b_{\text{in}}(t), \sqrt{\kappa_c}a^\dagger(t') - c^\dagger_{\text{in}}(t')] \\
&= \sqrt{\kappa_c\kappa_b}[a(t), a^\dagger(t')] - [\sqrt{\kappa_b}a(t), c^\dagger_{\text{in}}(t')] \\
&\quad - [b_{\text{in}}(t), \sqrt{\kappa_c}a^\dagger(t')],
\end{aligned}
\tag{C.32}
$$

where we have used the fact that $[b_{\text{in}}(t), c^\dagger_{\text{in}}(t')] = 0$. To determine the remaining commutators, we use Eq. (7.37) of the second edition of Ref. [35], which here reads

$$
\begin{aligned}
b_{\text{in}}(t) &= \frac{\sqrt{\kappa_c}}{2}a(t) - \frac{1}{\sqrt{2\pi}}\int_{-\infty}^{\infty} d\omega b(\omega, t) \\
c_{\text{in}}(t) &= \frac{\sqrt{\kappa_b}}{2}a(t) - \frac{1}{\sqrt{2\pi}}\int_{-\infty}^{\infty} d\omega c(\omega, t),
\end{aligned}
\tag{C.33}
$$

with $b(\omega, t)$ and $c(\omega, t)$ the field operators for modes of the transmission lines connected to the resonator. Using constraints coming from causality and the boundary condition Eq. (4.23), we have

$$
\begin{aligned}
[a(t), b_{\text{in}}(t')] = 0 \text{ for } t' > t \\
[a(t), b_{\text{out}}(t')] = 0 \text{ for } t' < t,
\end{aligned}
\tag{C.34}
$$

and similar expressions for c_{in}. The two previous expressions yield

$$
\begin{aligned}
[\sqrt{\kappa_b}a(t), c^\dagger_{\text{in}}(t')] &= \sqrt{\kappa_c\kappa_b}u(t-t')[a(t), a^\dagger(t')] \\
[b_{\text{in}}(t), \sqrt{\kappa_c}a^\dagger(t')] &= \sqrt{\kappa_c\kappa_b}u(t'-t)[a(t), a^\dagger(t')]
\end{aligned}
\tag{C.35}
$$

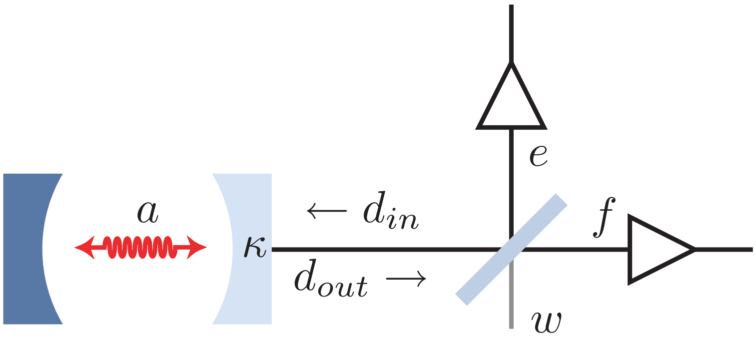

Figure C.1.: One-sided cavity with beamsplitter.

with

$$u(t) = \begin{cases} 1 & t > 0, \\ 1/2 & t = 0 \\ 0 & t < 0. \end{cases} \tag{C.36}$$

Putting everything together, we finally find that the modes commute

$$[b_{\text{out}}(t), c^\dagger_{\text{out}}(t')] = 0. \tag{C.37}$$

As a last note we want to mention what can be learned from these calculation for the expectation values in the form

$$\left\langle a^\dagger b_{\text{in}} \right\rangle, \qquad \left\langle c^\dagger_{\text{in}} a \right\rangle. \tag{C.38}$$

The general assumption is that the input modes are in the vacuum state. Still one has to be careful about the operator ordering, since these operators do not commute at all times (not to be confused with $b_{\text{out}}, c_{\text{out}}$ which were shown to commute). We will generally use the fact that

$$\left\langle a^\dagger b_{\text{in}} \right\rangle = 0 \tag{C.39}$$

whereas

$$\left\langle b_{\text{in}} a^\dagger \right\rangle = \left[b_{\text{in}} a^\dagger \right] \neq 0. \tag{C.40}$$

C.5. One-sided cavity with beamsplitter

In some cases it might be undesired to measure on the two sides of a cavity, therefore we will show how the same kind of measurements can be achieved with a one-sided cavity and a beam splitter.

Assume a system as in Fig. (C.1), where the output of a one-sided cavity (d_{out})is connected to a 50-50 beam splitter. The output modes e and f of the beam splitter are amplified as it is described in Sec. 4.2.2. Then the outputs of the beam splitter are given by

$$\begin{aligned} e &= (d_{\text{out}} + w)/\sqrt{2} \\ f &= (d_{\text{out}} - w)/\sqrt{2}, \end{aligned} \tag{C.41}$$

where w is the mode of the beam splitters vacuum port. The output of the cavity is given as in Eq. (4.23), by

$$d_{\text{out}} = \sqrt{\kappa} a - d_{\text{in}}. \tag{C.42}$$

Therefore

$$\begin{aligned} e &= \sqrt{\frac{\kappa}{2}} a - \frac{d_{\text{in}} - w}{\sqrt{2}} \\ f &= \sqrt{\frac{\kappa}{2}} a - \frac{d_{\text{in}} + w}{\sqrt{2}}. \end{aligned} \tag{C.43}$$

Comparing this to Eq. (4.23), we can see an equivalence of the output modes e, f in this setup to $b_{\text{out}}, c_{\text{out}}$ in our discussion above, by these replacements:

$$\kappa_c, \kappa_b \to \frac{\kappa}{2}, \qquad c_{\text{in}} \to \frac{d_{\text{in}} - w}{\sqrt{2}}, \qquad b_{\text{in}} \to \frac{d_{\text{in}} + w}{\sqrt{2}}. \tag{C.44}$$

We conclude that for the investigation of the cavity field the two sided symmetric setup and the asymmetric setup with a beam splitter are equivalent.

C.6. Complex envelope measurement in a quasi-classical picture

A different way to obtain the results of Sec. 4.2.2 is from a quasi-classical perspective. This is justified, since the signals after the amplifier should behave mainly classical. Therefore lets interpret our mode b as a classical field, where we can measure both quadratures $(x + ip)$ at the same time, by using classical signal processing methods. The result of this measurement can be described in terms of a classical probability distribution $Q(\alpha) = Q(x + ip)$. We can then write the expectation values for this measurment signal in terms of the distribution $Q(\alpha)$ as

$$\langle S \rangle = \langle x + ip \rangle = \int \alpha Q(\alpha) d^2\alpha \tag{C.45}$$

$$\left\langle (S^*)^m (S)^n \right\rangle = \int (\alpha^*)^m (\alpha)^n Q(\alpha) d^2\alpha \tag{C.46}$$

If one assumes now that this probability distribution is effectively given by the Q-function as it is commonly defined as

$$Q(\alpha) = \frac{\langle \alpha | \rho | \alpha \rangle}{\pi} \tag{C.47}$$

one obtains as in Eq.(4.50) of Ref. [35]

$$\begin{aligned}\left\langle (S^*)^m \, (S)^n \right\rangle &= \int (\alpha^*)^m \, (\alpha)^n \, Q(\alpha) d^2\alpha && \text{(C.48)}\\ &= \left\langle (b^n) \left(b^\dagger\right)^m \right\rangle && \text{(C.49)}\end{aligned}$$

where b and $b^\dagger$ are the field operators, which are *anti-normaly* ordered. In fact the assumption of a classical signal is not necessary in this derivation and therefore it is generally valid under assumption Eq. (C.47).

Bibliography

[1] Blais, A., Huang, R.-S., Wallraff, A., Girvin, S. M., and Schoelkopf, R. J. *Physical Review A* **69**(6), 062320 June (2004).

[2] Wallraff, A., Schuster, D. I., Blais, A., Frunzio, L., Huang, R. S., Majer, J., Kumar, S., Girvin, S. M., and Schoelkopf, R. J. *Nature* **431**, 162–167 (2004).

[3] Gabelli, J., Reydellet, L.-H., Feve, G., Berroir, J.-M., Placais, B., Roche, P., and Glattli, D. C. *Physical Review Letters* **93**(5), 056801 (2004).

[4] Menzel, E. P., Deppe, F., Mariantoni, M., Caballero, M. A. A., Baust, A., Niemczyk, T., Hoffmann, E., Marx, A., Solano, E., and Gross, R. (2010).

[5] Astafiev, O., Zagoskin, A. M., Abdumalikov, A. A., J., Pashkin, Y. A., Yamamoto, T., Inomata, K., Nakamura, Y., and Tsai, J. S. *Science* **327**(5967), 840–843 (2010).

[6] Houck, A., Schuster, D., Gambetta, J., Schreier, J., Johnson, B., Chow, J., Frunzio, L., Majer, J., Devoret, M., Girvin, S., and Schoelkopf, R. *Nature* **449**, 328 (2007).

[7] Hofheinz, M., Wang, H., Ansmann, M., Bialczak, R. C., Lucero, E., Neeley, M., O'Connell, A. D., Sank, D., Wenner, J., Martinis, J. M., and Cleland, A. N. *Nature* **459**(7246), 546–549 May (2009).

[8] Deleglise, S., Dotsenko, I., Sayrin, C., Bernu, J., Brune, M., Raimond, J.-M., and Haroche, S. *Nature* **455**(7212), 510–514 September (2008).

[9] Einstein, A. *Annalen der Physik* **17**, 132–148 (1905).

[10] Planck, M. *Annalen der Physik* **4**, 553 (1901).

[11] Muller, H., Peters, A., and Chu, S. *Nature* **463**(7283), 926–929 February (2010).

[12] Feynman, R. *International Journal of Theoretical Physics* **21**(6), 467–488 June (1982).

[13] Shor, P. W. *SIAM Journal on Scientific and Statistical Computing* **26**, 1484 (1997).

[14] Houck, A. A., Schreier, J. A., Johnson, B. R., Chow, J. M., Koch, J., Gambetta, J. M., Schuster, D. I., Frunzio, L., Devoret, M. H., Girvin, S. M., and Schoelkopf, R. J. *Phys. Rev. Lett.* **101**(8), 080502–4 August (2008).

[15] DiCarlo, L., Chow, J. M., Gambetta, J. M., Bishop, L. S., Johnson, B. R., Schuster, D. I., Majer, J., Blais, A., Frunzio, L., Girvin, S. M., and Schoelkopf, R. J. *Nature* **460**(7252), 240–244 July (2009).

[16] Grosse, N. B., Symul, T., Stobinska, M., Ralph, T. C., and Lam, P. K. *Physical Review Letters* **98**(15), 153603–4 (2007).

[17] Blais, A., Gambetta, J., Wallraff, A., Schuster, D. I., Girvin, S. M., Devoret, M. H., and Schoelkopf, R. J. *Physical Review A* **75**(3), 032329 March (2007).

[18] Wallraff, A., Schuster, D. I., Blais, A., Frunzio, L., Majer, J., Girvin, S. M., and Schoelkopf, R. J. *Physical Review Letters* **95**, 060501 (2005).

[19] Fragner, A., Göppl, M., Fink, J. M., Baur, M., Bianchetti, R., Leek, P. J., Blais, A., and Wallraff, A. *Science* **322**(5906), 1357–1360 (2008).

[20] Bishop, L. S., Chow, J. M., Koch, J., Houck, A. A., Devoret, M. H., Thuneberg, E., Girvin, S. M., and Schoelkopf, R. J. *Nature Physics* **5**(2), 105 February (2009).

[21] Birnbaum, K. M., Boca, A., Miller, R., Boozer, A. D., Northup, T. E., and Kimble, H. J. *Nature* **436**(7047), 87–90 July (2005).

[22] Frunzio, L., Wallraff, A., Schuster, D., Majer, J., and Schoelkopf, R. *IEEE Transactions On Applied Superconductivity* **15**(2), 860–863 June (2005).

[23] Barends, R., Baselmans, J., Hovenier, J., Gao, J., Yates, S., Klapwijk, T., and Hoevers, H. *IEEE Transactions on Applied Superconductivity* **17(2)**, 263 (2007).

[24] Makhlin, Y., Schön, G., and Shnirman, A. *Rev. Mod. Phys.* **73**(2), 357–400 May (2001).

[25] Koch, J., Yu, T. M., Gambetta, J., Houck, A. A., Schuster, D. I., Majer, J., Blais, A., Devoret, M. H., Girvin, S. M., and Schoelkopf, R. J. *Physical Review A* **76**(4), 042319 (2007).

[26] Bianchetti, R., Filipp, S., Baur, M., Fink, J. M., Göppl, M., Leek, P. J., Steffen, L., Blais, A., and Wallraff, A. *Phys. Rev. A* **80**(4), 043840 (2009).

[27] Lang, C. Diploma thesis, LMU Munich, (2009).

[28] Bianchetti, R. Three level tomography in circuit QED (unpublished), (2010).

[29] Göppl, M., Fragner, A., Baur, M., Bianchetti, R., Filipp, S., Fink, J. M., Leek, P. J., Puebla, G., Steffen, L., and Wallraff, A. *Journal of Applied Physics* **104**, 113904 (2008).

[30] Göppl, M. *Engineering Quantum Electronic Chips - Realization and Characterization of Circuit Quantum Electrodynamics Systems*. PhD thesis, ETH Zurich, (2009).

[31] Steffen, L. Master's thesis, Laboratory of solid state physics, ETH Zurich, (2008).

[32] Pobell, F. *Matter and Methods at Low Temperatures*. Springer, 3rd edition,, (2006).

[33] E.I. Mikulin, A. T. and Shkrebyonock, M. *Adv. Cryo. Eng.* **29**, 629 (1984).

[34] Brown, R. H. and Twiss, R. Q. *Royal Society of London Proceedings Series A* **242**, 300–324 November (1957).

[35] Walls, D. and Milburn, G. *Quantum optics*. Spinger-Verlag, Berlin, (1994).

[36] Mandel, L. and Wolf, E. *Optical Coherence and Quantum Optics*. Cambridge University Press, September (1995).

[37] Gardiner, C. W. and Collett, M. J. *Physical Review A* **31**(6), 3761– June (1985).

[38] Caves, C. M. *Physical Review D* **26**, 1817–1839 October (1982).

[39] Carmichael, H. J., Castro-Beltran, H. M., Foster, G. T., and Orozco, L. A. *Physical Review Letters* **85**(9), 1855–1858 Aug (2000).

[40] E.R. Marquina-Cruz, H.-B. *Laser Physics, Nonlinear and quantum optics* **18**, 157–164 (2008).

[41] Gerber, S., Rotter, D., Slodička, L., Eschner, J., Carmichael, H. J., and Blatt, R. *Physical Review Letters* **102**(18), 183601 May (2009).

[42] Imamoglu, Y. Y. A. *Mesoscopic Quantum Optics*. John Wiley & Sons, New York, (1999).

[43] Carmichael, H. J. *Statistical Methods in Quantum Optics 1: Master Equations and Fokker-Planck Equations*. Springer-Verlag, (1999).

[44] Schuster, D. I., Wallraff, A., Blais, A., Frunzio, L., Huang, R.-S., Majer, J., Girvin, S. M., and Schoelkopf, R. J. *Physical Review Letters* **94**(12), 123602 April (2005).

[45] Gambetta, J., Blais, A., Schuster, D. I., Wallraff, A., Frunzio, L., Majer, J., Devoret, M. H., Girvin, S. M., and Schoelkopf, R. J. *Physical Review A* **74**(4), 042318 October (2006).

[46] Brune, M., Schmidt-Kaler, F., Maali, A., Dreyer, J., Hagley, E., Raimond, J. M., and Haroche, S. *Physical Review Letters* **76**(11), 1800–1803 Mar (1996).

[47] Fink, J. M., Steffen, L., Studer, P., Bishop, L. S., Baur, M., Bianchetti, R., Bozyigit, D., Lang, C., Filipp, S., Leek, P. J., and Wallraff, A. *ArXiv e-prints* March (2010).

[48] Michler, P., Kiraz, A., Becher, C., Schoenfeld, W. V., Petroff, P. M., Zhang, L., Hu, E., and Imamoğlu, A. *Science* **290**, 2282–2285 December (2000).

[49] Santori, C., Fattal, D., Vučković, J., Solomon, G. S., and Yamamoto, Y. *Nature* **419**, 594–597 October (2002).

[50] Shannon, C. E. *Proceedings of the IRE* **37**(1), 10–21 (1949).

[51] Bozyigit, D. Technical report, Laboratory of solid state physics, ETH Zurich, (2008).

[52] Arnold, P. Technical report, Laboratory of solid state physics, ETH Zurich, (2008).

[53] Yates, R. Technical report, http://www.digitalsignallabs.com/fp.pdf, (2009).

[54] Lyons, R. G. *Understanding Digital Signal Processing (2nd Edition)*. Prentice Hall PTR, Upper Saddle River, NJ, USA, (2004).

Acknowledgements

This thesis is the result of the collaboration of a number of people. First of all I want to thank Prof. Wallraff for giving me the opportunity to work in the exciting field of circuit QED. I am thankful for the continuous support and the encouragement he provided, but also for the constructive criticism and the freedom I had during my work. He provided good guidance as a mentor and was able to spark my interest in scientific work.

Further, I want to thank Christian Lang and Lars Steffen who contributed greatly to the experimental and technical achievements of this thesis. In the beginning but also throughout the work their help was invaluable. In particular the implementation of the FPGA design and the time-resolved qubit control would have been impossible without their expertise.

To perform the experiments, the upkeep and operation of the experimental setup required a substantial piece of work and cannot be achieved alone. I want to thank especially Johannes Fink, Romeo Bianchetti and Matthias Baur for their support with the cryostat, the software and the lab equipment, as well as the fabrication of the sample.

For the support in the theoretical understanding, I want to thank Alexandre Blais and Marcus P. Silva for the fruitful discussions and their work on the mathematical formulations which resulted (not only) in the theoretical part of this thesis. Also, I want to thank Prof. Bölcskei for his kindness to help in administrative matters.

Finally I want to thank all the other people who greatly supported me on different levels, most importantly my *roommate* and my family, which made it possible for me to pursue my master thesis.